

Catalytic Hydrodeoxygenation of Bio-Oil Model Compounds (Ethanol, 2-Methyltetrahydrofuran) over Supported Transition Metal Phosphides

Phuong Phuc Nam Bui

Dissertation submitted to the faculty of Virginia Polytechnic Institute and State University in
partial fulfillment of the requirements for the degree of

Doctor of Philosophy
In
Chemical Engineering

David F. Cox, Chair

Shigeo T. Oyama

Y. A. Liu

John Y. Walz

December 20, 2012

Blacksburg, VA

Keywords: transition metal phosphide, nickel phosphide, tungsten phosphide, hydrodeoxygenation (HDO), deoxygenation, ethanol, 2-methyltetrahydrofuran, FTIR spectroscopy.

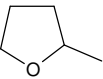
Copyright © 2012, Phuong Phuc Nam Bui

Catalytic Hydrodeoxygenation of Bio-Oil Model Compounds (Ethanol, 2-Methyltetrahydrofuran) over Supported Transition Metal Phosphides

Phuong Phuc Nam Bui

Abstract

The objective of this project is to investigate hydrodeoxygenation (HDO), a crucial step in the treatment of bio-oil, on transition metal phosphide catalysts. The study focuses on reactions of simple oxygenated compounds present in bio-oil – ethanol and 2-

methyltetrahydrofuran (2-MTHF) . The findings from this project provide fundamental knowledge towards the hydrodeoxygenation of more complex bio-oil compounds. Ultimately, the knowledge contributes to the design of optimum catalysts for upgrading bio-oil.

A series of transition metal phosphides was prepared and tested; however, the focus was on Ni₂P/SiO₂. Characterization techniques such as X-ray diffraction (XRD), temperature-programmed reduction and desorption (TPR and TPD), X-ray photoelectron spectroscopy (XPS), and chemisorption were used. In situ Fourier transform infrared (FTIR) spectroscopy was employed to monitor the surface of Ni₂P during various experiments such as: CO and pyridine adsorption and transient state of ethanol and 2-MTHF reactions. The use of these techniques allowed for a better understanding of the role of the catalyst during deoxygenation.

Acknowledgement

The last five years have been an important chapter of my life with some painful loses, but also many joyful rewards. I am grateful to have taken this journey and met wonderful people along the way.

I am sincerely grateful to my advisor and mentor Dr. S. Ted Oyama for his guidance and continuous support throughout the journey. Besides valuable professional critiques and advices, he taught me the beauty of science (chemistry) and instilled in me a passion for research and perfection. I also appreciate the time and support provided for my project by my committee members, Dr. Cox, Dr. Lu, Dr. Liu, and Dr. Walz.

I have gained invaluable experience from the international collaborations during my program and for this I would like to thank Dr. Juan A. Cecilia, Dr. Antonia Infantes-Molina, Dr. Enrique Rodríguez-Castellón, Dr. Antonio J. López, Dr. Atsuhiko Takagaki, Dr. Ara Cho, Ayako Iino, Dr. Tao Dou, and Dr. Zhao Shen.

I have special thanks for the invaluable friendships I have been lucky to have with the group members and other colleagues: Dr. Pelin Hacarlioglu, Dr. Sheima Khatib, Dr. Yujung Dong, Dr. Dan Li, Dr. Haiyan Zhao, Dr. Chen Chen, and Stuart Higgins. I appreciate the initial training from Dr. Travis Gott and Dr. Jason Gaudet. I would like to thank the Chemical Engineering Department staff, Riley Chan, Diane Cannaday, Tina Russell, Michael Vaught, Kevin Holshouser, Nora Bentley, and Jane Price for their help with the equipment maintenance, purchase orders, and various paperwork processes.

Words cannot express my gratitude to my large family – my parents, grandparents, uncles, aunts, and cousins. Though being far away, they have never stopped caring and

encouraging me every step of the way. Special thanks to my Mom and Dad who have been sacrificing their whole life for a better future for us and to my brother who has been my motivation.

My dearest love and appreciation goes to my husband – Logan Sorenson, he brings sunshine to my life, even when the sky is grey. I would also like to extend my thanks to my kind and sweet in-laws who are my second family.

*To my parents, Huong Hua and Cuong Bui,
and my life partner, Logan Sorenson,
for their constant love and support*

ATTRIBUTION

My dissertation includes collaborations from several colleagues around the world. A brief description of their contribution is included here.

Chapter 2: Rake Mechanism for the Deoxygenation of Ethanol over a Supported Ni₂P/SiO₂ Catalyst.

Chapter 2 was published in the Journal of Catalysis.

Dan Li earned his Ph. D from the Key Laboratory of Heavy Oil Processing in China University of Petroleum. Dr. Li was a co-author on this paper, wrote, and contributed to the research on catalytic ethanol decomposition.

Haiyan Zhao earned her Ph. D from the Environmental Catalysis and Materials Laboratory, Virginia Tech. Dr. Zhao was a co-author on this paper, helped with the Weisz-Prater calculation, and contributed editorial comments.

Shigeo T. Oyama, Ph. D, is a professor in the field of catalysis at both University of Tokyo and Virginia Tech. Dr. Oyama was a co-author on this paper, principal investigator for the grants supporting the research, and contributed editorial comments.

Tao Dou, Ph. D, and Zhen Zhao, Ph. D, are professors at the Key Laboratory of Heavy Oil Processing, China University of Petroleum. Dr. Dou and Dr. Zhao were co-authors on this paper and contributed editorial comments.

Chapter 3: Synthesis of Transition Metal Phosphides via Phosphate and Phosphite Method and their Activity in the Hydrodeoxygenation of 2-Methyltetrahydrofuran.

Chapter 3 was published in the Journal of Catalysis.

Juan A. Cecilia, Ph. D, is from the Departamento de Química Inorgánica, Unidad asociada al ICP-CSIC, Facultad de Ciencias, Universidad de Málaga (Spain). Dr. Cecilia was a co-author on this paper, wrote, and helped with the catalyst synthesis via phosphite method and the X-ray photoelectron spectroscopic experiments.

Shigeo T. Oyama, Ph. D, is a professor in the field of catalysis at both the University of Tokyo (Japan) and Virginia Tech. Dr. Oyama was a co-author on this paper, principal investigator for one of the grants supporting the research, and contributed editorial comments.

Atsushi Takagaki, Ph. D, is an assistant professor at the University of Tokyo. Dr. Takagaki was a co-author on this paper and contributed to the X-ray photoelectron spectroscopic experiments. Antonia Infantes-Molina, Ph. D, is a researcher at the Instituto de Catálisis, CSIC (Spain). Dr. Infantes-Molina was a co-author on this paper and assisted with the X-ray photoelectron spectroscopic experiments and editorial comments.

Haiyan Zhao earned her Ph. D from the Environmental Catalysis and Materials Laboratory, Virginia Tech. Dr. Zhao was a co-author on this paper and contributed editorial comments.

Dan Li earned his Ph. D from the Key Laboratory of Heavy Oil Processing in China University of Petroleum. Dr. Li was a co-author on this paper and contributed editorial comments.

Enrique Rodríguez-Castellón, Ph. D, and Antonio J. López, Ph. D, are professors at the Departamento de Química Inorgánica, Unidad asociada al ICP-CSIC, Facultad de Ciencias, Universidad de Málaga (Spain). Dr. Rodríguez-Castellón and Dr. López helped with the X-ray photoelectron spectroscopy research and contributed editorial comments.

Chapter 4: Kinetic and Spectroscopic Study of Deoxygenation of 2-Methyltetrahydrofuran over Supported Nickel Phosphide Catalyst.

Ayako Iino is a graduate student in the Department of Chemical System Engineering of the University of Tokyo. Iino helped with the temperature-programmed desorption of 2-MTHF from nickel phosphide.

Contents

Chapter 1 Introduction	1
1.1. Importance of Hydrodeoxygenation.....	1
1.2. Catalysts in Hydrodeoxygenation	2
1.2.1. Transition metal phosphides.....	3
1.2.2. Preparations of transition metal phosphides.....	4
1.3. Hydrodeoxygenation of Cyclic Ether Compounds	5
1.3.1. Aromatic cyclic ethers.....	6
1.3.2. Saturated cyclic ethers.....	12
1.4. Conclusions	16
1.5. Goals.....	16
1.6. Dissertation Overview.....	17
Reference	19
Chapter 2 Rake mechanism for the deoxygenation of ethanol over a supported Ni ₂ P/SiO ₂ catalyst	23
2.1. Introduction	23
2.2. Materials and Experiments.....	25
2.2.1. Materials	26
2.2.2. Nickel phosphide (Ni ₂ P/SiO ₂) synthesis.....	26
2.2.3. Characterization.....	27
2.2.4. Reactivity studies.....	30
2.3. Results and Discussion.....	31
2.3.1. Synthesis and basic characterization	31
2.3.2. Temperature-programmed desorption (TPD) of NH ₃ , pyridine, and CO ₂	34
2.3.3. Infrared spectroscopy of pyridine.....	37
2.3.4. Ethanol temperature-programmed desorption.....	40
2.3.5. Reactivity.....	44
2.4. Conclusions	57
Reference	59

Chapter 3 Synthesis of Transition Metal Phosphides via Phosphate and Phosphite Method and their Activity in the Hydrodeoxygenation of 2-Methyltetrahydrofuran	62
3.1. Introduction:	62
3.2. Materials and Experiments	64
3.2.1. Materials and catalysts	64
3.2.2. Reactivity studies	68
3.3. Results and Discussion	70
3.3.1. Temperature-programmed reduction	70
3.3.2. BET surface area	75
3.3.3. CO chemisorption	76
3.3.4. X-ray diffraction	77
3.3.5. X-ray photoelectron spectroscopy	80
3.3.6. Reactivity in hydrodeoxygenation (HDO) of 2-methyltetrahydrofuran (2-MTHF)....	83
3.4. Conclusions	102
3.5. Supplementary Information	104
Reference	106
 Chapter 4 Kinetic and Spectroscopic Study of Deoxygenation of 2-Methyltetrahydrofuran over Supported Nickel Phosphide Catalyst	 108
4.1. Introduction	108
4.2. Materials and Experiments	108
4.2.1. Materials and synthesis	108
4.2.2. General characterization	109
4.2.3. Low temperature reactivity test	109
4.2.4. Kinetic test	111
4.2.5. Temperature-programmed desorption	111
4.2.6. Fourier transform infrared (FTIR) spectroscopic experiments	112
4.3. Results and Discussion	113
4.3.1. Characterization	113
4.3.2. Low temperature reactivity test	115
4.3.3. Kinetic study	116
4.3.4. Temperature-programmed desorption	121

4.3.5. Fourier transform spectroscopy	122
4.4. Conclusions	133
4.5. Supplementary Information.....	133
4.5.1. Crystallite size calculations	133
4.5.2. Weisz – Prater criterion for internal diffusion.....	134
Reference	135
Chapter 5 Conclusions	136
5.1. Conclusions	136
5.2. Recommendations for future work.....	137

Lists of Tables

Table 1.1. Summary of recent studies on catalytic HDO of dibenzofuran and benzofuran	6
Table 1.2. Summary of recent studies on catalytic HDO of furan 	11
Table 1.3. Summary of studies on catalytic HDO of tetrahydrofuran 	13
Table 2.1. The true width at half-maximum of the peak and crystallite size of Ni ₂ P/SiO ₂ catalyst	33
Table 2.2. Characterization results for HZSM-5 and Ni ₂ P/SiO ₂ catalysts	34
Table 2.3. Acid and base properties for HZSM-5 and Ni ₂ P/SiO ₂ catalysts	39
Table 2.4. Distribution of ethylene and acetaldehyde in different temperature ranges on EtOH-TPD	41
Table 2.5. Parameters in the Gorte Criterion	44
Table 2.6. Reactivity in ethanol deoxygenation (Contact time = 162 s)	45
Table 2.7. Rate constants used in the simulation	52
Table 2.8. Summary of FTIR assignments	56
Table 3.1. Materials and amounts used in the preparation of phosphides supported on silica	66
Table 3.2. Characterization results for the supported phosphide catalysts. (I) – catalysts made by the phosphite method, (A) – catalysts made by the phosphate method	76
Table 3.3. Spectral parameters for Ni ₂ P/SiO ₂ and WP/SiO ₂ catalysts	80
Table 3.4. Conversions and apparent activation energies of 2-MTHF HDO on transition metal phosphides	84
Table 3.5. Product selectivity for HDO of 2-MTHF on transition metal phosphides at 275 °C *Conversions of FeP/SiO ₂ were at 300°C	89
Table 3.6. Parameters in the Weisz-Prater Criterion	104
Table 3.7. The observed reaction rates and corresponding Weisz-Prater criterion for Ni ₂ P/SiO ₂	104
Table 3.8. The observed reaction rates and corresponding Weisz-Prater criterion for WP/SiO ₂ (I)	105
Table 3.9. The observed reaction rates and corresponding Weisz-Prater criterion for WP/SiO ₂ (A)	105
Table 4.1: Masses monitored during temperature programmed desorption of 2-MTHF and their relative intensity	112
Table 4.2: Characterization results of Ni ₂ P/SiO ₂ ; * BET surface area value of SiO ₂	115
Table 4.3 Effects of H ₂ and 2-MTHF partial pressures on the conversion of 2-MTHF over Ni ₂ P/SiO ₂	117
Table 4.4: Assignment of FTIR peaks	132
Table 4.5. Parameters in the Weisz-Prater Criterion	134
Table 4.6: C _{WP} values for reactivity test at low temperature	135

List of Figures

Fig. 1.1. Triangular prism (mono-phosphide - MP) and tetrakaidecahedral structure (metal-rich phosphide – M ₂ P) [53]	4
Fig. 2.1. Synthesis and XRD Analysis of Ni ₂ P/SiO ₂	32
Fig. 2.2. Mass 17 signal from NH ₃ -TPD	35
Fig. 2.3. Mass 79 signal from pyridine-TPD	36
Fig. 2.4.. Mass 44 signal from CO ₂ -TPD.....	37
Fig. 2.5. Infrared spectra of adsorbed pyridine over samples at 423 K	38
Fig. 2.6. Infrared spectra of adsorbed pyridine over samples at 423 K	41
Fig. 2.7. Conversion and Selectivity from EtOH-TPD.....	42
Fig. 2.8. Variation of ethanol conversion and product yield as a function of reaction temperature at a contact time of 162 s. a) HZSM-5 b) Ni ₂ P/SiO ₂	46
Fig. 2.9. Variation of ethanol conversion and product yield as a function of contact time on HZSM-5. a) Reaction temperature of 473 K b) Reaction temperature of 498 K.....	47
Fig. 2.10. Variation of ethanol conversion and product yield as a function of contact time on Ni ₂ P/SiO ₂ . The curves are fits from a simulation model discussed in the text.	49
Fig. 2.11. EtOH FTIR over Ni ₂ P/SiO ₂ with 0.15% EtOH in He flow	53
Fig. 2.12. EtOH FTIR over Ni ₂ P/SiO ₂ in He at 497 K	55
Fig. 3.1. Temperature-programmed reduction of transition metal phosphide catalysts supported on silica; heating rate of 2°C/min, H ₂ flow rate of 100ccm/g of catalyst. a) Mass 18 signal, phosphite precursors, b) Mass 18 signal, phosphate precursors, c) Mass 34 (PH ₃) signal, phosphite precursors, d) Mass 34 (PH ₃) signal, phosphate precursors.	71
Fig. 3.2. X-ray diffraction patterns of supported phosphide catalysts	78
Fig. 3.3. Ni 2 <i>p</i> and P 2 <i>p</i> core-level spectra for silica supported nickel phosphide catalysts	81
Fig. 3.4. W 4 <i>f</i> and P 2 <i>p</i> core-level spectra for silica supported tungsten phosphide catalysts.....	82
Fig. 3.5. Turnover frequency of 2-MTHF on transition metal phosphides.....	85
Fig. 3.6. Total conversion and selectivity towards HDO products of 2-MTHF reaction on transition metal phosphides.....	86
Fig. 3.7. Product selectivity of 2-MTHF reaction on Ni ₂ P/SiO ₂ and CoP/SiO ₂ at a total conversion of around 5%	89
Fig. 3.8. Product selectivity of 2-MTHF reaction on WP/SiO ₂ and MoP/SiO ₂ at total conversion of 5%	91
Fig. 3.9. Product selectivity of 2-MTHF reaction on FeP/SiO ₂ and Pd/Al ₂ O ₃ at total conversion of 5%	93
Fig. 3.10. Contact time study on Ni ₂ P/SiO ₂	95
Fig. 3.11. Contact time study on WP/SiO ₂ prepared by the phosphite and phosphate methods ...	98

Fig. 4.1 X-ray diffraction pattern of Ni ₂ P/SiO ₂	114
Fig. 4.2. Arrhenius plot of 2-MTHF conversion over Ni ₂ P/SiO ₂	116
Fig. 4.3. Selectivity of products in partial pressure experiment	119
Fig. 4.4. Estimate of reaction order of H ₂ and 2-MTHF	120
Fig. 4.5: Temperature programmed desorption of 2-MTHF on Ni ₂ P/SiO ₂ in H ₂ and He at atmospheric pressure, heating rate of 3 °C min ⁻¹ , injection temperature was at 30 °C.....	121
Fig. 4.6 Temperature programmed desorption of 2-MTHF on Ni ₂ P/SiO ₂ in H ₂ at atmospheric pressure, heating rate of 3 °C min ⁻¹ , injection temperature was at 150 °C	122
Fig. 4.7. Temperature programmed desorption of 2-MTHF from the support SiO ₂ in H ₂	124
Fig. 4.8 Proposed structural models of (a) P ₂ O ₅ /SiO ₂ and (b) Ni ₂ P/SiO ₂ [8]	125
Fig. 4.9. Temperature programmed desorption of 2-MTHF from Ni ₂ P/SiO ₂ in H ₂	127
Fig. 4.10 Temperature programmed desorption of 2-MTHF from Ni ₂ P/SiO ₂ in He	128
Fig. 4.11. FTIR spectra of 2-MTHF adsorbed on Ni ₂ P/SiO ₂ in 0.32% 2-MTHF/H ₂ flow as a function of temperature.....	130
Fig. 4.12. FTIR spectra of 2-MTHF adsorbed on Ni ₂ P/SiO ₂ in 2-MTHF/He flow as a function of temperature	131
Fig. 4.13. Transient FTIR spectra following the introduction of 2-MTHF onto Ni ₂ P/SiO ₂ in H ₂	132

List of Schemes

Scheme 1.1. Simplified reaction network for dibenzofuran	9
Scheme 1.2. Simplified reaction network for benzofuran	9
Scheme 1.3. Reaction network of furan on various catalysts	12
Scheme 1.4. Reaction network of tetrahydrofuran on CoMo/Al ₂ O ₃	14
Scheme 1.5. Reaction network of tetrahydrofuran on supported Pt catalysts	15
Scheme 1.6. Reaction network of 2-methyltetrahydrofuran on Pt catalysts.....	16
Scheme 2.1. “Rake” mechanism for ethanol reaction.....	50
Scheme 3.1. HDO reaction network of 2-MTHF on Ni ₂ P/SiO ₂	97
Scheme 3.2. HDO reaction network of 2-MTHF on WP/SiO ₂ (phosphate method).....	100
Scheme 3.3. HDO reaction network of 2-MTHF on WP/SiO ₂ (phosphite method).....	102

List of Abbreviation

BF	Benzofuran
BET	Brunauer, Emmett and Teller surface area
CUS	Coordinatively Unsaturated Sites
DBF	Dibenzofuran
FTIR	Fourier Transform Infrared spectroscopy
HDN	Hydrodenitrogenation
HDO	Hydrodeoxygenation
HDS	Hydrodesulfurization
HYD	Hydrogenation
HMS	Hybrid Mesoporous Silica
2-MTHF	2-Methyltetrahydrofuran
THF	Tetrahydrofuran
TPD	Temperature Controlled Desorption
TPR	Temperature Controlled Reduction
XRD	X-ray Diffraction
XPS	X-ray Photoelectron Spectroscopy

Chapter 1

Introduction

1.1. Importance of Hydrodeoxygenation

The search for renewable energy sources has been receiving much attention for many reasons such as depletion of fossil fuels, new stringent environmental regulations, and rapid growth of global energy consumption [1]. Biomass has several advantages over conventional fossil fuels as an energy source. For example, biomass has a net zero CO₂ production, negligible SO_x and NO_x emissions, and abundant availability [2-8]. Raw biomass materials come from various sources, including wastes and by-products from agriculture and forestry [9-11]. Therefore, utilization of biomass as an energy source contributes greatly to the recycling industry and the conservation of the environment. For these reasons, biomass presents one of the most promising energy sources.

Biomass can be converted to liquid products directly through liquefaction processes at high pressures [10, 12-14]. In fast and flash pyrolysis, biomass is heated rapidly ($\sim 300 \text{ }^\circ\text{C min}^{-1}$ to up to $700 \text{ }^\circ\text{C}$) at a relatively low pressure (up to 0.2 MPa) in the absence of oxygen and produces the highest yield of liquid products (50-70 %) [10, 15, 16]. However, raw biomass derived oil is not suitable for direct use as fuel. Typically, the raw oil contains 35-50 wt% of oxygenated compounds in which water takes up to 30 wt% [10, 17-20]. The high oxygen content results in many disadvantages such as immiscibility with hydrocarbon fuels, low heating value, and low chemical and thermal stability [4, 21-23]. Therefore, removing oxygenated compounds is essential in the treatment of bio-oil.

There are three typical ways to reduce oxygen content: hydrodeoxygenation (HDO), decarbonylation, and catalytic cracking [24]. The HDO process entails cleavage of C-O bonds in the presence of hydrogen to form hydrocarbons and environmentally benign water. This resembles the hydrodesulfurization (HDS) and hydrodenitrogenation (HDN) processes in petroleum feedstock hydro-treatment. These processes have been studied in depth, creating an excellent background for research in HDO [25]. Furthermore, the HDO process can be incorporated to the existing petroleum refining infrastructure and technology, an important fact that reinforces the potential of HDO as one of the most promising methods to upgrade bio-oil [26-30].

1.2. Catalysts in Hydrodeoxygenation

Hundreds of oxygen-rich substances in bio-oil have been identified including guaiacol, aldehydes, ketones, furans, organic acids, and phenolic compounds [3, 20, 31, 32]. Furimsky provided a thorough review of catalytic hydrodeoxygenation [4]. Traditional hydrotreating catalysts (such as CoMo/Al₂O₃ or NiMo/Al₂O₃) have been investigated for HDO reactivity on bio-oil [31, 33-36] as well as bio-oil model compounds [37-42]. Supported precious metal catalysts were also examined [43-47]. Presulfidation requirement of the traditional CoMo and NiMo catalysts and high costs and scarcity of the noble metal catalysts are among the drawbacks of these materials.

The choice of catalyst supports plays an important role in HDO activity. One of the most popular catalyst supports is Al₂O₃; however, Al₂O₃ has been shown to be unsuitable for HDO. In the presence of large amounts of water Al₂O₃ converts to boehmite [16, 48, 49]. The formation of boehmite results in oxidation of nickel as well as blockage of Mo and Ni sites on the catalyst.

Moreover, Popov et al. suggested that the acidity of Al_2O_3 led to the high affinity for carbon formation (coking) on this type of support [50]. Among alternative support materials, SiO_2 has been used due to its neutrality and relatively low affinity for coking. Other supports were also investigated such as carbon, ZrO_2 , and CeO_2 [43, 51, 52]. However, SiO_2 still has a better economic edge due to its lower cost and the ease of preparation and utilization.

1.2.1. Transition metal phosphides

Emerging alternatives to sulfur containing catalysts and noble metal catalysts are transition metal carbides, nitrides and phosphides. These catalysts exhibit combined physical properties of both metals and ceramic, and thus are good conductors of heat and electricity, are hard and strong and have high thermal and chemical stability [53, 54]. Though having similar physical properties, the phosphides differ from the carbides and nitrides substantially in their crystal structure. The carbon in carbides and the nitrogen in nitrides have an atomic radius of 0.071 nm and 0.065 nm respectively, substantially smaller than that of the phosphorus (0.109 nm) in phosphides. Therefore, in the crystal structure of carbides and nitrides, the carbon and nitrogen atoms reside in the interstitial spaces inside the octahedral spaces formed by the closed-packed metal atoms, whereas the larger-sized phosphorus does not fit in these spaces and is instead located in the center of triangular prisms of metal atoms (Fig. 1.1). The phosphides are also different from the sulfides (present in the conventional molybdenum catalysts) as they do not form flat layered structures; instead, they have more isotropic external morphologies that give rise to globular shapes. As described later in the deoxygenation on traditional molybdenum catalysts, many studies reported that the active sites are located at the edges of the layered MoS_2 slabs (Section 1.4.1). Due to the globular shapes, the phosphides potentially permit greater

access to active corner and edge sites than the sulfides [55]. Transition metal carbides and nitrides suffer deactivation in the presence of high sulfur level in petroleum feedstocks [56-58]. Meanwhile, transition metal phosphides possess enhanced stability, high sulfur resistance, and high reactivity for hydrotreating reactions [53]. For these advantages, transition metal phosphides are considered potential substitutes for conventional CoMo and NiMo catalysts [53, 55, 59]. Recent work has shown that MoP [60-62], WP [62-64], CoP [65-67], and Ni₂P [53, 68-72] are highly active for HDS and HDN. This knowledge serves as a background for further investigation of their HDO activity.

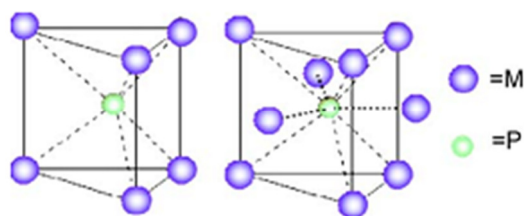


Fig. 1.1. Triangular prism (mono-phosphide - MP) and tetrakaidecahedral structure (metal-rich phosphide – M₂P) [53]

1.2.2. Preparations of transition metal phosphides

Many methods were reported for the synthesis of transition metal phosphides such as solid state reaction of metal and phosphorous, electrolysis of fused salts, and most popular recently reduction of phosphate precursors [55, 73-76]. However, there is still much need for an improved preparation method. Milder synthesis conditions as well as better carrier materials are the main targets in order to reduce energy consumption during catalyst production and maintain a high surface area for the catalysts. Metal phosphides are mostly supported on high surface area materials to maximize their catalytic effects. Less acidic supports are preferred because they favor both the formation of metal phosphides and the reduction of coke deposition [77, 78].

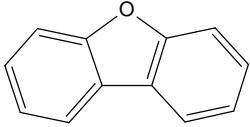
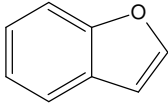
Precursors other than phosphates were also investigated [70, 79, 80]. Among the newer precursors, metal phosphites stand out as an important development. Compared to phosphate, phosphite contains phosphorus in a lower oxidation state and thus should be reducible at a lower temperature [65, 70, 77, 81]. For instance, active Ni₂P phase from phosphite precursor was formed at a reduction temperature of 300 °C, whereas when using phosphate as precursor, the active phase was formed at the reduction temperature of 500 °C [59, 82]. Conditions to prepare phosphite precursors are also much less intense than those of phosphates. Specifically, phosphite precursor preparation only requires drying at low temperatures (< 120 °C) and bypasses the calcination at high temperatures (> 450 °C) that is mandated in phosphate preparation.

1.3. Hydrodeoxygenation of Cyclic Ether Compounds

A plethora of work has been conducted on the HDO of a wide range of oxygenated compounds in which lignin derivatives (phenols and substituted phenols) received the most attention [83-88]. The apparent reactivity of different compounds followed the order of: alcohol > ketone > alkylether > carboxylic acid ~ m-/p- phenol ~ naphthol > phenol > diarylether ~ o-phenol ~ alkylfuran > benzofuran > dibenzofuran [4]. Aromatic model compounds (phenols and benzofurans) constitute the hardest classes of compounds to deoxygenate and therefore are often chosen in HDO studies of model compounds. To overcome the high energy barrier of the aromatic group, the hydrodeoxygenation process typically involves with hydrogenation (HYD) of the unsaturated ring, followed by deoxygenation. Transition metal phosphides with good hydrogen-transfer properties are well-capable to catalyze the initial hydrogenation and therefore are excellent potential catalysts for hydrodeoxygenation.

1.3.1. Aromatic cyclic ethers

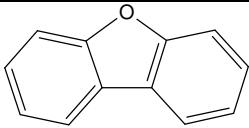
Cyclic ethers pose interesting topics for HDO investigations. Aromatic cyclic ethers, such

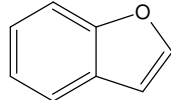
as dibenzofuran (DBF) , benzofuran (BF) , and furan ,

present in conventional petroleum feedstock (~0.1 wt%), heavy oil distillates (~2 wt%), oil shale (~1 wt%), and coal derived liquids (~7 wt%) [4, 89, 90] and therefore receive considerable coverage [4]. Though constituting a small amount, these compounds are important for their resistance to HDO and their effects on the hydrodesulfurization (HDS) and the hydrodenitrogenation (HDN) during hydrotreating processes [91]. A review by Furimsky comprehensively covers various aspects of catalytic HDO of these compounds including mechanism, kinetics, and interaction modes of the reactants with the catalyst surfaces [4]. More recent studies are summarized in Table 1.1 and Table 1.2.

1.3.1.a) Hydrodeoxygenation of dibenzofuran (DBF) and benzofuran (BF)

Table 1.1. Summary of recent studies on catalytic HDO of dibenzofuran and benzofuran

Catalysts	Remarks	Reference
Various	A review of studies prior to 2000 covered catalytic hydrodeoxygenation of mostly conventional catalysts – NiMo or CoMo on alumina. Carbides and nitrides showed to be less active than conventional catalysts.	Furimsky [4], Ramanathan [92]
 Studies on Dibenzofuran (2000-2012)		
Pt/ mesoporous ZSM5 Pt/ ZSM5	Reaction network: hydrogenation of one aromatic ring occurred first.	Wang [93]

Pt/Al ₂ O ₃	Mesoporous ZSM-5 support enhanced the catalyst activity compared to the alumina support.	
 <p>Studies on Benzofuran (2000-2012)</p>		
Sulfided NiMoP/Al ₂ O ₃	Reaction network: partial hydrogenation of the furan ring occurred first. Self-inhibition of BF and intermediate oxygenated species was observed. Presence of H ₂ S promoted HDO and hydrogenation activity.	Romero [83]
Mo/Al ₂ O ₃ NiMo/Al ₂ O ₃ (sulfided and reduced)	Reaction network: partial hydrogenation of the furan ring occurred first. The Ni promoter promoted hydrogenation and HDO. The reduced catalyst was superior to the sulfided catalyst. The reduced catalyst contained coordinatively unsaturated sites and favored full hydrogenation of 2,3-dihydrobenzofuran prior to oxygen removal. The sulfided catalyst contained Brønsted acid sites and favored hydrogenolysis of 2,3-dihydrobenzofuran to ethylphenol prior to oxygen removal. The presence of H ₂ S decreased HDO activity.	Bunch [38, 39, 94]
Pt/activated carbon in super critical water	Reaction network: partial hydrogenation of the furan ring occurred first. Self-inhibition of BF and intermediate oxygenated species was observed.	Dickinson [95]
Pt/ SiO ₂ -Al ₂ O ₃ Pd/ SiO ₂ -Al ₂ O ₃ Pt _x Pd _y / SiO ₂ -Al ₂ O ₃	HDO reactivity: PtPd (1:4) alloy > Pd > Pt. Reaction network: full hydrogenation of the aromatic ring occurred prior to oxygen removal. Self-inhibition of BF and intermediate oxygenated species was observed.	Liu [96]
Ni ₂ P/SiO ₂	Catalyst loading amount was optimum at 18.1wt% with HDO conversion of 80%. Low loading amount led to incomplete formation of Ni ₂ P phase while high loading amount led to formation of Ni-Ni bond which is susceptible to coking.	Oyama [68]

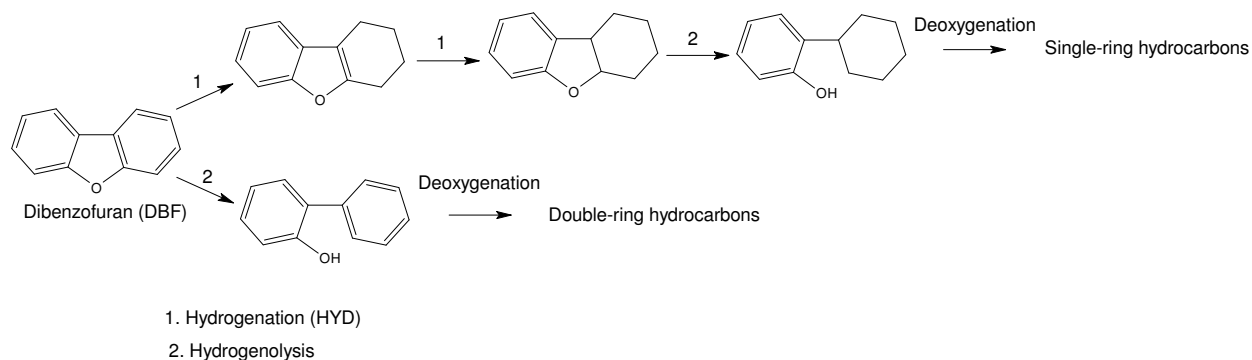
On conventional NiMo or CoMo catalysts, HDO of DBF and BF exhibits hydrogenation, hydrogenolysis and direct deoxygenation. The main products were substituted phenols, aromatic and cyclic hydrocarbons (Scheme 1.1, Scheme 1.2). Self-inhibition by intermediate products and sulfur containing compounds as well as poisoning by nitrogen containing compounds was

observed [97-99]. The mutual inhibition of HDO and HDS indicates competitive adsorptions at the same active sites. This was supported by the oxygen-chemisorption results that showed linear correlation with HDS activity [100] and the same adverse effect of coking on HDS and HDO [101]. The HDO of DBF and BF showed products from both hydrogenation and hydrogenolysis routes (Scheme 1.1, Scheme 1.2). The existence of different active sites for hydrogenation and hydrogenolysis has been frequently proposed in the literature [102] though both types of active sites involve coordinatively unsaturated Mo surface atoms (CUS) formed by sulfur vacancies associated with Mo atoms at the edges of MoS₂ slabs [83, 94]. The distinction between hydrogenation and hydrogenolysis sites was found related to the degree of uncoordination [103, 104], the Brønsted-Lewis acidic character [102, 105], or the environment of the vacancy [106-108]. A small amount of H₂S in the feed was reported to be beneficial to the overall HDO as it maintained the MoS₂ slabs while some portion of surface sulfur was replaced with oxygen atoms from the reactant [109, 110].

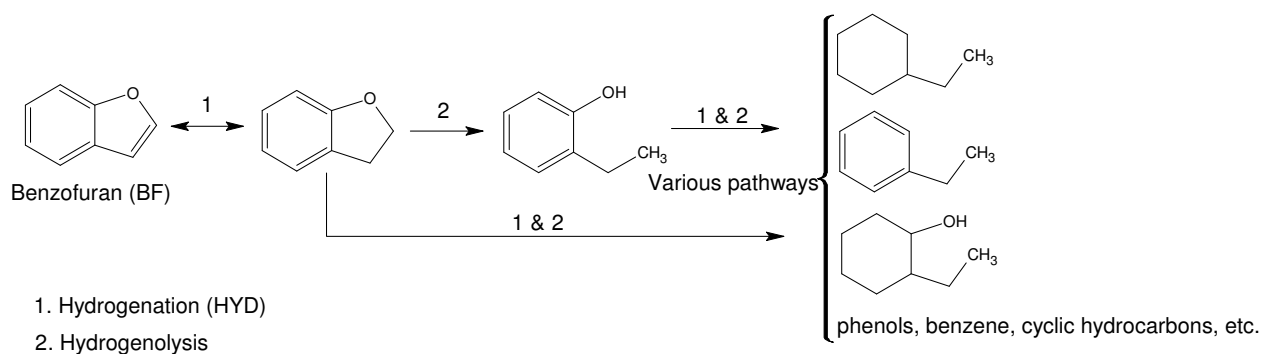
Laurent and Delmon proposed that C-O hydrogenolysis of DBF could be based on an ensemble of coordinatively unsaturated Mo atoms and the hydrogenation (HYD) sites located on one triply unsaturated Mo atom [40]. The HYD sites may have been responsible for forming a π -interaction with one of the aromatic rings and weaken the C-O bond, leading to hydrogenolysis. The HYD sites also gave rise to partially or fully hydrogenated products. Direct deoxygenation from DBF may originate from σ -bonded adsorption of the oxygen to the hydrogenolysis site. Direct deoxygenation of DBF is not as straightforward as direct desulfurization of DBT because oxygen is less polarizable than sulfur [111].

Similar deductions could be drawn for BF in which the π -bond with the HYD sites results in a partial hydrogenation of BF to 2,3-dihydroBF, then interactions with hydrogenolysis sites

cleave C-O bond to produce ethylphenol. Unlike DBF, the direct deoxygenation of BF was not observed experimentally on the conventional NiMo or CoMo catalysts.



Scheme 1.1. Simplified reaction network for dibenzofuran



Scheme 1.2. Simplified reaction network for benzofuran

There are few studies on HDO of DBF for catalysts other than conventional nickel or cobalt molybdenum catalysts. Most recently, noble metal (Pt) on various supports were tested [93]. Mesoporous hierarchical ZSM5 zeolites have combined advantages of uniform meso-pore size and strong acidity and were expected to improve catalytic activities. The catalyst indeed was better than the supported alumina and microporous ZSM5. Considering that the supports (mesoporous ZSM5, ZSM5 and alumina) have plenty of acidic sites and that acidic sites are

generally considered hydrogenolysis or dehydration sites, it is interesting that direct deoxygenation did not occur on any of these catalysts. Instead, the catalysts showed strong hydrogenation capacity and some dehydration activity. This indicated hydrogen spill-over effect from the metal sites to the acidic sites, a well-known phenomenon for noble metals [102, 112].

A similar study for HDO of BF was conducted on Pt, Pd and alloyed PtPd supported on silica-alumina [96]. Complete ring hydrogenation prior to deoxygenation was observed, consistent with the hydrogenation capacity of metallic catalysts. The HDO activity followed the order of PtPd (1:4) > Pd > Pt. On Pt/activated carbon, the major pathway involved initial partial hydrogenation of the furan ring prior to hydrogenolysis [95]. The experiment was conducted in supercritical water and increasing water loading led to a decrease in fully hydrogenated compounds as well as total deoxygenation. This suggests that water may have inhibited hydrogenation by strong bonding to HYD sites. Self-inhibition from the reactant and the oxygenated intermediates was also observed, consistent with previous studies on other catalysts [94, 99].

1.3.1.b) Hydrodeoxygenation of furan

The simplest aromatic oxygenated compound – furan – was studied mostly on traditional catalysts consisting of promoted and unpromoted molybdenum on various supports and a few other catalysts (Table 1.2). All experiments on furan were conducted at atmospheric pressure to prevent complete hydrogenation to tetrahydrofuran (THF). The goal was to observe the interactions between the furan ring and the catalyst.

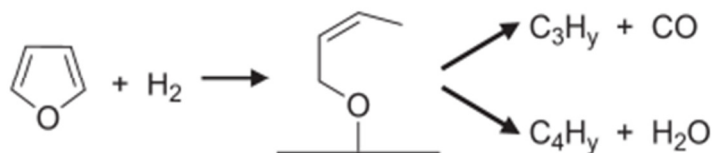


Table 1.2. Summary of recent studies on catalytic HDO of furan

Catalysts	Remarks	Reference
Various	Review (studies prior to 2000): Catalytic hydrodeoxygenation of mostly conventional NiMo or CoMo on alumina catalysts	Furimsky [4]
Studies on Furan (2000-2012)		
Mo, NiMo, CoMo on various supports (Al-HMS, MCM41) HMS = hybrid mesoporous silica	HDO reactivity: CoMo/Al-HMS > NiMo/Al-HMS > Mo/Al-HMS NiMo/MCM41 > CoMo/MCM41 > Mo/MCM41	Chiranjeevi [113-115]
MoS ₂ Density functional theory (DFT) study	The stability of MoS ₂ catalyst depends on H ₂ S/H ₂ O ratio during the reaction. The metallic edge is stable regardless of the ratio; the sulfur edge needs a presence of H ₂ S to prevent partial oxygenation. Furan adsorbs on coordinatively unsaturated sites (vacancy of an S atom from the metallic edge). Reaction energies are 0.5 eV for the η^1 adsorption mode of furan and 1.39 eV for the η^5 adsorption mode.	Badawi [109]
Ru ₂ P, RuP, Ru, and Ni ₂ P supported on SiO ₂ , CoMo/Al ₂ O ₃	HDO activity: Ru ₂ P/SiO ₂ >> RuP/SiO ₂ > Ru/SiO ₂ > Ni ₂ P/SiO ₂ >> CoMo/Al ₂ O ₃ Ru/SiO ₂ strongly favored C3 hydrocarbons while others favored C4 hydrocarbons. Phosphorous may have increased Lewis acid acidity, resulting in stabilization of a ring-opened species having an $\eta^1(O)$ geometry. Meanwhile, Ru/SiO ₂ contained mostly $\eta^2(C,O)$ species that favored decarbonylation.	Bowker [116]

Furan hydrodeoxygenation occurs via direct deoxygenation, hydrogenation, hydrogenolysis, and cracking with C3 and C4 hydrocarbons as major products (Scheme 1.3). In all of the studies (Table 1.2), no dihydrofuran or tetrahydrofuran in the product stream was observed indicating that initial partial hydrogenation of the ring was fast and was followed immediately by a ring opening (Scheme 1.3). Promoted catalysts performed better than unpromoted catalysts and this was shown on both molybdenum and tungsten catalysts on various

supports [113-115, 117, 118]. The promoter did not increase the number of active sites, rather it promoted the intrinsic activity of the sites.



Scheme 1.3. Reaction network of furan on various catalysts [116]

The simplicity of furan allowed detailed density functional theory calculations [116]. On MoS₂, the calculations showed furan only adsorbs onto defective metal sites that have at least one anion sulfur vacancy. The calculations also showed that a small presence of H₂S is needed in order to keep the MoS₂ from being oxygenated, this is consistent with a previous study [110].

1.3.2. Saturated cyclic ethers

Under a high H₂ pressure of typical hydrotreating conditions, unsaturated cyclic ethers are partially or fully hydrogenated. Thus, saturated cyclic ethers are an important intermediate before the final oxygen removal. Hydrodeoxygenation of tetrahydrofuran has been investigated on CoMo/Al₂O₃, supported Pt, and supported Mo catalysts (Table 1.3)

1.3.2.a) Hydrodeoxygenation of tetrahydrofuran (THF)

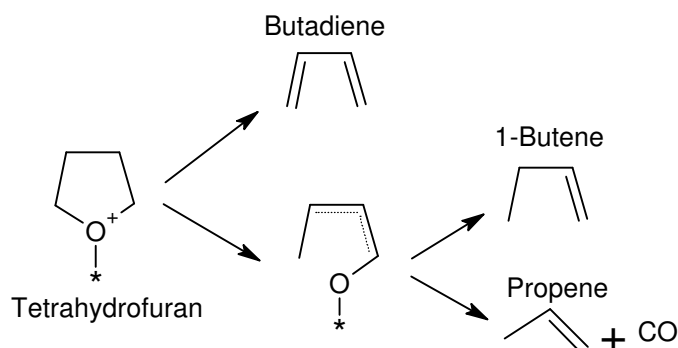


Table 1.3. Summary of studies on catalytic HDO of tetrahydrofuran

Catalysts	Remarks	Reference
CoMo/Al ₂ O ₃	HDO products are similar to furan HDO (butenes, propene, etc.) Sulfided catalyst provided more efficient transfer of surface hydrogen to the adsorbed THF thus increased HDO activity and suppressed decarbonylation compared to non-sulfided catalyst. Little HDO reactivity on the Al ₂ O ₃ support produced same products with the reduced catalyst.	Furimsky [119]
Pt on TiO ₂ , SiO ₂ , and Al ₂ O ₃	HDO activity: Pt/TiO ₂ > Pt/SiO ₂ and Pt/Al ₂ O ₃ >> Pt Cracking formed CO which poisoned the catalyst. At high temperature (over 200 °C) the adsorbed CO was reformed into methane. C-O scission occurred on the Pt/support phase boundary.	Kreuzer [120], Bartok [121]
Mo on TiO ₂ , ZrO ₂ , and TiO ₂ -ZrO ₂	HDO activity: Mo/TiO ₂ -ZrO ₂ > Mo/TiO ₂ > Mo/ZrO ₂ Mixed oxide supports may have facilitated formation of coordinatively unsaturated sites, increasing HDO activity.	Maity [122]

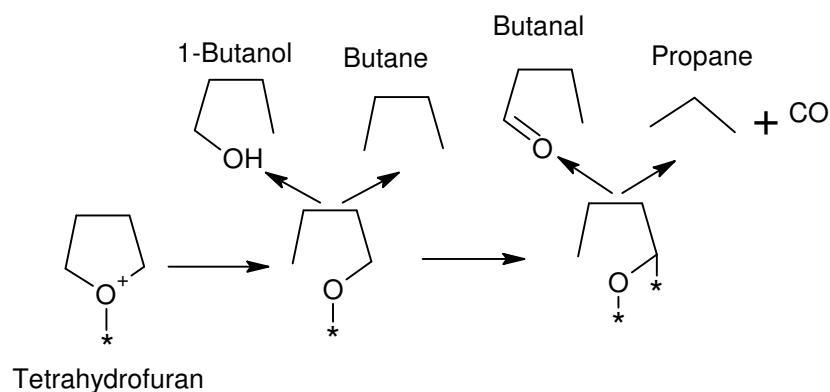
Over CoMo/Al₂O₃ catalyst, HDO of THF produced dehydrogenated products including butenes (sulfided catalysts) and propylene and butadiene (reduced catalyst) (Scheme 1.4). More hydrogenated products on the sulfided catalyst suggested a better surface hydrogen transfer than on the reduced catalyst. About 39% of THF converted to tar and coke on the reduced catalyst (compared to 8% for the sulfided catalyst). The lack of effective hydrogen surface species may have caused polymerization of butadienes. No alcohol or aldehyde products were observed, indicating the ring opened intermediate stayed attached to the catalyst surface via the O atom throughout the deoxygenation. In the absence of hydrogen, there was a small extent of HDO

activity over the reduced catalysts as well as over the Al_2O_3 support suggesting intramolecular migration of THF's hydrogen atoms.



Scheme 1.4. Reaction network of tetrahydrofuran on CoMo/Al₂O₃

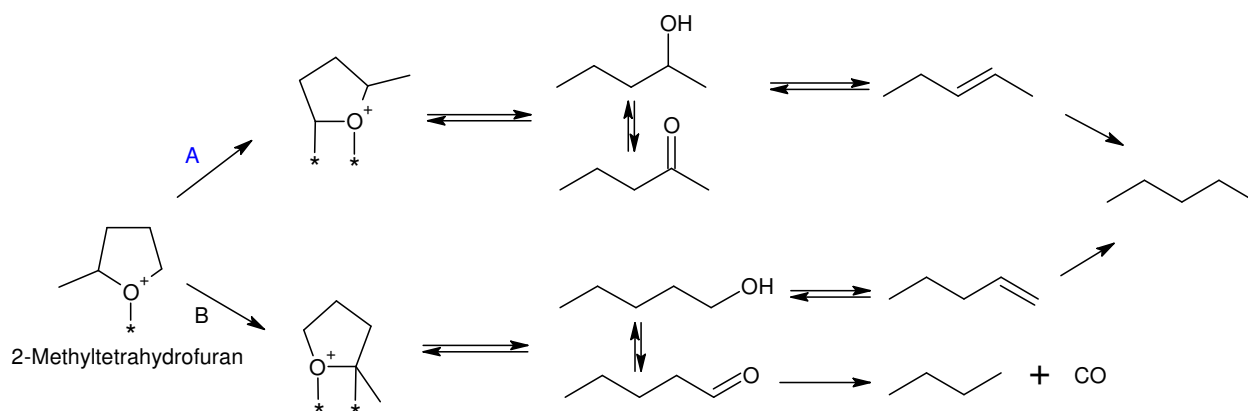
Over noble metal catalysts, HDO of THF produced fully hydrogenated products such as butane, propane, and 1-butanol (Scheme 1.5). The hydrogenation preference on metal catalysts is consistent with the studies on BF and DBF (Table 1.1). Both Kreuzer et al. [120] and Bartok et al. [121] investigated the HDO of THF on the Pt catalyst and obtained similar products, yet they proposed different reaction pathways. Kreuzer et al. proposed that 1-butanol was the first ring opened product which could go through a hydrogenolysis to give butane or transform into butanal – a secondary product that reacted to form propane and CO. Bartok et al. proposed a sequence of surface reactions in which the formation of both 1-butanol and butane was from an $\eta^1(\text{O})$ surface butoxy species and the formation of butanal and propane was from an $\eta^2(\text{CO})$ surface species. The supports showed a strong effect on the selectivity. The phase boundary of the metal and the support provided active sites for C-O bond scission. The TiO₂ supported Pt yielded mostly butane while SiO₂ and Al₂O₃ supported ones produced more decarbonylation products and CO. In all cases, CO caused self-poisoning of the Pt surface.



Scheme 1.5. Reaction network of tetrahydrofuran on supported Pt catalysts

1.3.2.b) Hydrodeoxygenation of 2-methyltetrahydrofuran (2-MTHF)

Research on HDO of 2-MTHF is limited. Platinum, palladium and nickel catalysts were tested [123-126] but the most detailed results were for Pt catalysts. A proposed reaction network for 2-MTHF involved the reactant adsorbed onto two active sites and proceeded in two pathways (Scheme 1.6). The main pathway (A) occurred as the bond between oxygen and the primary carbon atom was cleaved, producing 2-pentanone and 2-pentanol as primary product, then pentene and pentane as secondary and final products. The pathway (B) involved scission between the oxygen and the secondary carbon which led to 1-pentanol and pentanal as primary products (observed only at 150 °C) and to pentane or decarbonylated to butane as final products. The selectivity towards pathway (B) was 30% on the supported Pt and 7% on the unsupported Pt. The silica support had no reactivity therefore the pathway (B) activity was due to the phase boundary.



Scheme 1.6. Reaction network of 2-methyltetrahydrofuran on Pt catalysts

1.4. Conclusions

Commercialization of second generation biomass derived oil depends on an efficient and economical oxygen removal system. The review on HDO of cyclic ethers emphasized the importance of surface hydrogen species in the HDO reactivity. The traditional hydrotreating catalysts (supported CoMo, NiMo, or Mo) require the presence of H_2S – a well-known pollutant – to maintain the stability of the active phase; yet, overdosing H_2S causes adverse effect on the HDO reactivity. Metal catalysts tend to be poisoned by CO produced from cracking reactions. Transition metal phosphides were shown to have good hydrogen transfer capacity and good resistance to sulfur and nitrogen contained compounds; therefore these catalysts have great potential in hydrodeoxygenation applications.

1.5. Goals

The research presented in this dissertation aims to characterize supported transition metal phosphides with a special focus on Ni₂P/SiO₂, evaluate their activity in HDO reactions, and investigate the mechanisms of HDO. In order to reach the goal, the following tasks have been carried out:

- Synthesis of transition metal phosphides on high surface area support via two methods – phosphate method and phosphite method.
- Characterization of the catalysts with CO chemisorption, BET surface area measurements, temperature-programmed desorption, and X-ray diffraction measurements.
- NH₃ temperature-programmed desorption on Ni₂P/SiO₂ to quantify the catalyst acidity.
- Fourier transformed infrared measurements to investigate the acidic properties of Ni₂P catalysts with pyridine as a probe molecule.
- Steady state reactivity and transient study of ethanol reactions on Ni₂P/SiO₂.
- Fourier transform infrared measurements of ethanol reactions on the Ni₂P/SiO₂ surface.
- Steady state reactivity and transient study of 2-methyltetrahydrofuran reactions on Ni₂P/SiO₂.
- Fourier transform infrared measurements of 2-MTHF reactions on the Ni₂P/SiO₂ surface.

1.6. Dissertation Overview

Chapter 1 describes the motivation of the project and provides background information including reviews on catalysts in hydrodeoxygenation processes and studies on catalytic reactions of cyclic ethers.

Chapter 2 presents a study of ethanol decomposition on $\text{Ni}_2\text{P}/\text{SiO}_2$ and HZSM5. A reaction network was proposed on $\text{Ni}_2\text{P}/\text{SiO}_2$.

Chapter 3 presents a study of 2-methyltetrahydrofuran reactions on a series of transition metal phosphides. The phosphides were synthesized via two methods: the phosphate precursor method and the phosphite precursor method. Reaction networks were proposed for the iron group phosphides (Ni_2P and CoP) and group 8 metal phosphides (WP and MoP).

Chapter 4 presents a Fourier transform infrared spectroscopic study of 2-methyltetrahydrofuran on $\text{Ni}_2\text{P}/\text{SiO}_2$.

Chapter 5 presents the conclusions of this research and suggestions for future work.

References

1. Demirbas, A., *Appl. Energ.*, 86 (2009) S108.
2. A. A. Lappas, S. Bezergianni, I. A. Vasalos, *Catal. Today*, 145 (2009) 55.
3. D. Mohan, C. U. Pittman Jr., P. H. Steele, *Energ. Fuel*, 20 (2006) 848.
4. Furimsky, E., *Appl. Catal. A: Gen.*, 199 (2000) 147.
5. J. I. C. Shumaker, S. A. Crofcheck, E. S. Tackett, M. Jiménez, *Catal. Lett.*, 115 (2007) 56.
6. Klass, D. L., *Biomass for renewable energy*. Fuels and chemicals. 1998, San Diego: Academic Press.
7. L. R. Lynd, J. H. Cushman, R. J. Nichols, C. E. Wyman, *Science*, 251 (1991) 1318.
8. S. Czernik, A. V. Bridgwater, *Energ. Fuel*, 18 (2004) 590.
9. M. F. Demirbas, M. Balat, *J. Sci. Ind. Res.*, 66 (2007) 797.
10. H. B. Goyal, D. Seal, R. C. Saxena, *Renewable and Sustainable Energy Reviews*, 12 (2008) 504.
11. McKendry, P., *Bioresour. Technol.*, 83 (2002) 37.
12. Demirbas, A., *Energ. Convers. Manage.*, 42 (2001) 1357.
13. Demirbas, A., *Energ. Convers. Manage.*, 41 (2000) 633.
14. L. Zhang, C. Xu, P. Champagne, *Energ. Convers. Manage.*, 51 (2010) 969.
15. A. V. Bridgwater, G. V. C. Peacocke, *Renewable Sustainable Energy Rev.*, 4 (2000) 1.
16. Elliott, D. C., *Energ. Fuel*, 21 (2007) 1792.
17. C. A. Mullen, A. A. Boateng, *Energ. Fuel*, 22 (2008) 2104.
18. M. Bertero, G. de la Puente, U. Sedran, *Fuel*, 95 (2012) 263.
19. Bridgwater, T., *Biomass Bioenergy*, 31 (2007) 7.
20. J. H. Marsman, J. Wildschut, P. Evers, S. de Koning, H. J. Heeres, *J. Chromatogr. A.*, 1188 (2008) 17.
21. A. Oasmaa, S. Czernik, *Appl. Catal. A: Gen.*, 13 (1999) 914.
22. Yaman, S., *Energ. Convers. Manage.*, 45 (2004) 651.
23. Demirbas, M. F., *Appl. Energ.*, 86 (2009) S151.
24. S. R. A. Kersten, W. P. M. van Swaaij, L. Lefferts, K. Seshan: G. Centi, R. A. van Santen (Eds.), *Catalysis for renewable - from feedstocks to energy production*. 2007, Weinheim: Wiley-VCH. Chapter 6.
25. R. Prins, M. Egorova, A. Rothlisberger, Y. Zhao, N. Sivasankar, P. Kukul, *Catal. Today*, 111 (2006) 84.
26. J. Sadhukhan, K. S. Ng, *Ind. Eng. Chem. Res.*, 50 (2011) 6794.
27. F. M. Mercader, M. J. Groeneveld, S. R. A. Kersten, N. W. J. Way, *Appl. Catal. B: Environ.*, 96 (2010) 57.
28. J. A. Melero, A. Garcia, J. Iglesias, *Advances in clean hydrocarbon fuel processing: Science and technology*. 2011, Cambridge: Woodhead Publishing. 199.
29. S. Fernando, S. Adhikari, C. Chandrapal, N. Murali *Energ. Fuel*, 20 (2006) 1727.
30. F. de M. Mercader, M. J. Groeneveld, S. R. A. Kersten, C. Geantet, G. Toussaint, N. W. J. Way, C. J. Schaverien, K. J. A. Hogendoorn, *Energy Environ. Sci.*, 4 (2011) 985.
31. P. M. Mortensen, J. D. Grunwaldt, P. A. Jensen, K. G. Knudsen, A. D. Jensen, *Appl. Catal. A: Gen.*, 407 (2011) 1.
32. G. W. Huber, S. Iborra, A. Corma, *Chem. Rev.*, 106 (2006) 4044.
33. S. D. S. Murti, K. H. Choi, K. Sakanishi, O. Okuma, Y. Korai, I. Mochida, *Fuel*, 84 (2005) 135.

34. J. Wildschut, F. H. Mahfud, R. H. Venderbosch, H. J. Heeres, *Ind. Eng. Chem. Res.*, 48 (2009) 10324.
35. J. Zakzeski, P. C. A. Bruijninx, A. L. Jongerius, B. M. Weckhuysen, *Chem. Rev.*, 110 (2010) 3552.
36. V. N. Bui, G. Toussaint, D. Laurenti, C. Mirodatos, C. Geantet, *Catal. Today*, 143 (2009) 172.
37. A. Popov, E. Kondratieva, J. Gilson, L. Mariey, A. Travert, F. Mauge, *Catal. Today*, 172 (2011) 132.
38. A. Y. Bunch, U. S. Ozkan, *J. Catal.*, 206 (2002) 177.
39. A. Y. Bunch, X. Wang, U. S. Ozkan, *J. Mol. Catal. A*, 270 (2007) 264.
40. E. Laurent, B. Delmon, *Appl. Catal. A: Gen.*, 109 (1994) 77.
41. E. M. Ryymin, M. L. Honkela, T. R. Viljava, A. O. Krause, *Appl. Catal. A: Gen.*, 389 (2010) 114.
42. V. N. Bui, D. Laurenti, P. Afanasiev, C. Geantet, *Appl. Catal. B: Environ.*, 101 (2011) 239.
43. A. Gutierrez, R. K. Kaila, M. L. Honkela, R. Slioor, A. O. I. Krause, *Catal. Today*, 147 (2009) 239.
44. D. Prochazkova, P. Zamostny, M. Bejblova, L. Cerveny, J. Cejka, *Appl. Catal. A: Gen.*, 332 (2007) 56.
45. R. C. Runnebaum, R. J. Lobo-Lapidus, T. Nimmanwudipong, D. E. Block, B. C. Gates, *Energ. Fuel*, 25 (2011) 4776.
46. T. Nimmanwudipong, R. C. Runnebaum, D. E. Block, B. C. Gates, *Energ. Fuel*, 25 (2011) 3417.
47. T. T. Pham, L. L. Lobban, D. E. Resasco, R. G. Mallinson, *J. Catal.*, 206 (2009) 9.
48. E. Laurent, A. Centeno, B. Delmon, in *6th Inter. Symp. Catalyst Deactivation*, 1994.
49. R. H. Venderbosch, A. R. Ardiyanti, J. Wildschut, A. Oasmaa, H. J. Heeres, *J. Chem. Technol. Biotechnol.*, 85 (2010) 674.
50. A. Popov, E. Kondratieva, J. M. Goupil, L. Mariey, P. Bazin, J. -P. Gilson, A. Travert, F. Mauge, *J. Phys. Chem. C*, 114 (2010) 15661.
51. V. A. Yakovlev, S. A. Khromova, O. V. Sherstyuk, V. O. Dundich, D. Y. Ermakov, V. M. Novopashina, M. Y. Lebedev, O. Bulavchenko, V. N. Parmon, *Catal. Today*, 144 (2009) 362.
52. V. N. Bui, D. Laurenti, P. Delichère, C. Geantet, *Appl. Catal. B: Environ.*, 111 (2011) 246.
53. S. T. Oyama, T. Gott, H. Zhao, Y. -K. Lee, *Catal. Today*, 143 (2009) 94.
54. Oyama, S. T., *Transition metal carbides, nitrides, and phosphides*. Handbook of catalysis, ed. H. K. G. Ertl, J. Weitkamp. 2008, Weinheim: Springer-Verlag.
55. Oyama, S. T., *J. Catal.*, 216 (2003) 343.
56. B. Dhandapani, T. St. Clair, S. T. Oyama, *Appl. Catal. A: Gen.*, 168 (1998) 219.
57. B. Diaz, S. J. Sawhill, D. H. Bale, R. Main, D. C. Phillips, S. Korlann, R. Self, M. E. Bussell, *Catal. Today*, 86 (2003) 191.
58. Furimsky, E., *Appl. Catal. A: Gen.*, 240 (2003) 1.
59. S. T. Oyama, X. Wang, Y. -K. Lee, K. Bando, F. G. Requejo, *J. Catal.*, 210 (2002) 207.
60. P. Clark, X. Wang, S. T. Oyama, *J. Catal.*, 207 (2002) 256.
61. W. Li, B. Dhandapani, S. T. Oyama, *Chem. Lett.*, (1998) 207.
62. P. Clark, X. Wang, P. Deck, S. T. Oyama, *J. Catal.*, 210 (2002) 116.

63. P. Clark, W. Li, S. T. Oyama, *J. Catal.*, 200 (2001) 140.
64. S. T. Oyama, P. Clark, X. Wang, T. Shido, Y. Iwasawa, S. Hayashi, J. M. Ramallo-Lopez, F. G. Requejo, *J. Phys. Chem. B*, 106 (2002) 1913.
65. J. A. Cecilia, A. Infantes-Molina, E. Rodríguez-Castellón, A. Jiménez-López, *Appl. Catal. B: Environ.*, 92 (2009) 100.
66. X. Wang, P. Clark, S. T. Oyama, *J. Catal.*, 208 (2002) 321.
67. V. Zuzaniuk, R. Prins, *J. Catal.*, 219 (2003) 85.
68. S. T. Oyama, X. Wang, Y. -K. Lee, W. -J. Chun, *J. Catal.*, 221 (2004) 263.
69. S. T. Oyama, Y. -K. Lee, *J. Catal.*, 258 (2008) 393.
70. J. A. Cecilia, A. Infantes-Molina, E. Rodríguez-Castellón, A. Jiménez-López, *J. Phys. Chem. C*, 113 (2009) 17032.
71. C. Stinner, R. Prins, Th. Weber, *J. Catal.*, 202 (2001) 187.
72. Y. Shu, S. T. Oyama, *Carbon*, 43 (2005) 1517.
73. Chene, M., *Anal. Chim.*, 15 (1941) 187.
74. West, A. R., *Solid state chemistry and its applications*. 1992, Chichester: Wiley.
75. S. Burns, J. S. J. Hargreaves, S. M. Hunter, *Catal. Comm.*, 8 (2007) 931.
76. A. Montesinos-Castellanos, T. A. Zepeda, B. Pawelec, J. L. G. Fierro, J. A. de los Reyes, *Chem. Mater.*, 19 (2007) 5627.
77. J. A. Cecilia, A. Infantes-Molina, E. Rodríguez-Castellón, A. Jiménez-López, *J. Catal.*, 263 (2009) 4.
78. T. I. Korányi, Z. Vít, D. G. Poduval, R. Ryoo, H. -S. Kim, E. J. M. Hensen, *J. Catal.*, 253 (2008) 119.
79. H. Loboue, C. Guillot-Deudon, A. Florin Popa, A. Lafond, B. Rebours, C. Pichon, T. Cseri, G. Berhault, C. Geantet, *Catal. Today*, 130 (2008) 63.
80. Z. W. Yao, L. Wang, H. Dong, *J. Alloy Compd.*, 473 (2009) L10.
81. Q. Guan, W. Li, M. Zhang, K. Tao, *J. Catal.*, 263 (2009) 1.
82. G. Shi, J. Shen, *J. Mater. Chem.*, 19 (2009) 2295.
83. Y. Romero, F. Richard, Y. Reneme, S. Brunet, *Appl. Catal. A: Gen.*, 353 (2009) 45.
84. M. Badawi, J. F. Paul, S. Cristol, E. Payen, Y. Romero, F. Richard, S. Brunet, D. Lambert, X. Portier, A. Popov, E. Kondratieva, J. M. Goupil, J. El Fallah, J. P. Gilson, L. Mariey, A. Travert, F. Mauge, *J. Catal.*, 282 (2011) 155.
85. H. Y. Zhao, D. Li, P. Bui, S. T. Oyama, *Appl. Catal. A: Gen.*, 391 (2011) 305.
86. C. Zhao, Y. Kou, A. A. Lemonidou, X. Li, J. A. Lercher, *Angew. Chem. Int. Ed.*, 48 (2009) 3987.
87. F. E. Massoth, P. Politzer, M. C. Concha, J. S. Murray, J. Jakowski, J. Simons, *J. Phys. Chem. B*, 110 (2006) 14283.
88. N. Yang, Y. Yuan, R. Dykeman, Y. Kou, P. Dyson, *Angew. Chem. Int. Ed.*, 49 (2010) 5549.
89. Furimsky, E., *Catal. Rev. Sci. Eng.*, 25 (1983) 421.
90. Leckel, D., *Energ. Fuel*, 22 (2008) 231.
91. C. Lee, D. F. Ollis, *J. Catal.*, 87 (1984) 332.
92. S. Ramanathan, S. T. Oyama, *J. Phys. Chem.*, 99 (1995) 16365.
93. Y. Wang, Y. Fang, T. He, H. Hu, J. Wu, *Catal. Comm.*, 12 (2011) 1201.
94. A. Y. Bunch, X. Wang, U. S. Ozkan, *Appl. Catal. A: Gen.*, 346 (2008) 96.
95. J. G. Dickinson, J. T. Poberezny, P. E. Savage, *Appl. Catal. B: Environ.*, 123-124 (2012) 357.
96. C. Liu, Z. Shao, Z. Xiao, C. T. Williams, C. Liang, *Energ. Fuel*, 26 (2012) 4205.

97. C. Kordulis,A. Gouromihou,A. Lycourghiotis,C. Papadopoulo,H. K. Mataralis, *Appl. Catal.*, 67 (1990) 39.
98. V. LaVopa, C. N. Satterfield, *J. Catal.*, 110 (1998) 375.
99. E. O. Odebunmi ,D. F. Ollis, *J. Catal.*, 80 (1983) 65.
100. S. J. Tauster, T. A. Pecorara, R. R. Chianelli, *J. Catal.*, 63 (1980) 515.
101. Y. Yamamoto,F. Kumata,F. E. Massoth, *Fuel Proc. Technol.*, 19 (1998) 253.
102. H. Du,C. Fairbridge,H. Yang,Z. Ring, *Appl. Catal. A: Gen.*, 294 (2005) 1.
103. Delmon, B., *Bull. Soc. Chim. Belg.*, 88 (1979) 979.
104. Y. Okamoto,A. Maezawa,T. Imanaka, *J. Catal.*, 120 (1989) 29.
105. C. Moreau,C. Aubert,R. Durand,N. Zmimita,P. Geneste, *Catal. Today*, 4 (1988) 117.
106. B. Delmon ,J. L. Dallons, *Bull. Soc. Chim. Belg.*, 97 (1988) 473.
107. J. Miciukiewicz,W. Zmierczak,F. E. Massoth, *Bull. Soc. Chim. Belg.*, 96 (1987) 915.
108. V. Stuchly, L. Beranek, *Appl. Catal.*, 35 (1987) 35.
109. M. Badawi,S. Cristol,J. Paul,E. Payen, *C. R. Chimie*, 12 (2009) 754.
110. T. Kabe, W. Quian, A. Ishihara, *J. Phys. Chem.*, 98 (1994) 912.
111. M. J. Girgis ,B. C. Gates, *Ind. Eng. Chem. Res.*, 33 (1994) 1098.
112. U. Roland, T. Braunschweig, F. Roessner, *J. Mol. Catal. A*, 127 (1997) 61.
113. T. Chiranjeevi, G. M. Kumaran, J. K. Gupta, G. M. Dhar, *Catal. Comm.*, 6 (2005) 101.
114. T. Chiranjeevi, G. M. Kumaran, J. K. Gupta, G. M. Dhar, *Thermochim. Acta.* , 443 (2006) 87.
115. T. Chiranjeevi, G. M. Kumaran, J. K. Gupta, G. M. Dhar, *Pet. Sci. Technol.* , 26 (2008) 690.
116. R. H. Bowker, M. C. Smith, M. L. Pease, K. M. Slenkamp, L. Kovarik, M. E. Bussell, *ACS Catal.*, 1 (2011) 917.
117. K. S. P. Rao,S. Khajamasthan,G. Muralidhar,K. V. R. Chary,V. S. Subrahmanyam, *J. Chem. Soc., Chem. Comm.*, (1988) 375.
118. K.V.R. Chary,K. S. Ramarao,G. Muralidhar,P. Kantarao, *Letter to Editor*, (1990).
119. Furimsky, E., *Ind. Eng. Chem. Prod. Res. Dev.*, 22 (1983) 31.
120. K. Kreuzer ,R. Kramer, *J. Catal.*, 167 (1997) 391.
121. M. Bartok,G. Szollosi,J. Apjok, *React. Kinect. Catal. Lett.*, 64 (1998) 21.
122. S. K. Maity, M. S. Rana, S. K. Bej, J. Ancheyta-Juarez, G. M. Dhar, T. S. R. P. Rao, *Catal. Lett.*, 72 (2001) 115.
123. U. Gennari, R. Krammer, H. L. Gruber, *Appl. Catal.*, 11 (1984) 341.
124. U. Gennari, R. Krammer, H. L. Gruber, *Appl. Catal.*, 44 (1988) 239.
125. F. Notheisz ,M. Bartok, *J. Catal.*, 71 (1981) 331.
126. M. Bartok ,F. Notheisz, *J. Catal.*, 68 (1981) 209.

Chapter 2

Rake Mechanism for the Deoxygenation of Ethanol over a Supported Ni₂P/SiO₂ Catalyst

D. Li, P. Bui, H. Zhao, S. T. Oyama, T. Dou, Z. H. Shen

Journal of Catalysis, Volume 290, June 2012, Pages 1-12

Used with permission of the Elsevier, 2013

2.1. Introduction

The utilization of biomass for the production of fuels and chemicals is currently an area of great activity because of the recognition that fossil fuels are a finite resource and because of the imminent threat of global warming from the release of carbon dioxide [1-6]. Among the major products of biomass conversion is ethanol, a commodity chemical derived from the fermentation of sugar cane or energy-rich crops such as corn [7, 8]. Although ethanol is produced in large quantities as a substitute or supplement for fuels derived from crude oil, it is currently unlikely to replace much less expensive chemical feedstocks derived from petroleum or natural gas. Nevertheless, in a future with limited hydrocarbon supplies there may be a role for ethanol as a primary feedstock [9] as recently demonstrated by the startup of a 200,000 metric ton ethylene from ethanol plant in Brazil [10], and for this reason research in ethanol conversion is warranted. It is also of interest to study ethanol for fundamental reasons. First, it is one of the simplest of oxygenated compounds and its deoxygenation can provide insight into oxygen removal from more complicated molecules. Second, it can react to produce different products, and for this

reason can be used as a probe to relate the reaction pathway to the properties of the catalysts, in particular their acid-base properties versus their metallic nature. This study is thus motivated in part to explore the catalytic chemistry of deoxygenation and in part to determine the role of intermediates in the reaction pathway. Use is made of a traditional acid catalyst, HZSM-5, which has been shown to be an effective agent for dehydration, and a metallic catalyst, Ni₂P, which has been demonstrated to have hydrogen transfer capabilities. The use of metallic catalysts is important because studies have shown that biomass conversion cannot be carried out by acid catalysts alone [1-3].

The decomposition of ethanol on solid catalysts typically occurs through competing reactions [8, 11-13]: 1) intermolecular dehydration, which gives diethyl ether and water, 2) intramolecular dehydration, which yields ethylene and water, 3) dehydrogenation which produces acetaldehyde and hydrogen, and 4) total decomposition to CO, H₂, CH₄, C and O [7]. The acidity and basicity of the solid catalysts are two important factors that influence their activity and selectivity. Dehydration generally occurs on acidic sites [14-16], and dehydrogenation usually proceeds on basic sites [17, 18].

An important pathway for ethanol conversion is dehydration to ethylene. Previous studies reported that HZSM-5 zeolite with strong Brønsted acid sites was an effective catalyst for this transformation [19]. However, deactivation by formation of coke on its surface led to decreasing activity and selectivity towards ethylene [20] and therefore made the process unsuitable for industrial applications [21]. Phillips and Datta [22] investigated the production of ethylene from hydrous ethanol over HZSM-5 under mild conditions and demonstrated that strong Brønsted acid sites led to rapid catalyst deactivation in the initial stages through the oligomerization of ethylene

and the formation of carbonaceous species. However, moderating the acidity could reduce coke formation and enhance the steady-state catalytic activity of HZSM-5.

Another important pathway for ethanol decomposition is dehydrogenation to acetaldehyde and hydrogen which is favored on basic [23] or metallic catalysts [24]. Chang et al. reported that copper catalysts supported on rice husk ash displayed high catalytic activity and selectivity towards dehydrogenation [24]. Much attention has been focused on preparing bifunctional catalysts with both acidic and basic sites in order to promote both dehydrogenation and dehydration [25-28]. Aramendía et al. [29, 30] claimed that basic sites were responsible for dehydrogenation and both weak acid and basic sites were associated with dehydration.

Although there are a wide variety of catalysts for ethanol conversion, there has been no report on the decomposition of ethanol over transition metal phosphide catalysts. Transition metal phosphide catalysts possess excellent hydrogen transfer properties and have been investigated extensively in hydrotreating applications. They have also been used in hydrodeoxygenation studies and have shown promising results [31]. Therefore, it is of interest to determine the activity of transition metal phosphides in ethanol conversion. In the present study, Ni₂P/SiO₂ catalyst was chosen for catalyzing the ethanol decomposition process because it is generally the most active of the transition metal phosphides for a variety of reactions (HDS, HDN, and HDO) [31-39]. Comparison is made to HZSM-5, the most widely studied acid catalyst.

2.2. Materials and Experiments

2.2.1. Materials

The HZSM-5 (Si/Al=15) commercial catalysts were obtained from Zeolyst International. The transition metal phosphide $\text{Ni}_2\text{P}/\text{SiO}_2$ was prepared on a fumed silica EH-5 support provided by the Cabot Corp. The chemicals used in the synthesis of the catalyst were $\text{Ni}(\text{NO}_3)_2 \cdot 6\text{H}_2\text{O}$ (Alfa Aesar, 99%), $(\text{NH}_4)_2\text{HPO}_4$ (Aldrich, 99%). The chemical utilized in the reactivity study was ethanol (Decon Laboratories, Inc, 200 Proof). The gases employed were H_2 (Airco, Grade 5, 99.99%), He (Airco, Grade 5, 99.99%), CO (Linde Research Grade, 99.97%), 0.5% O_2/He (Airco, UHP Grade, 99.99%), O_2 (Airco, UHP Grade, 99.99%), 10% CO_2 (Airco, UHP Grade, 99.99%), NH_3 (Alexander Chemical Corporation, AH200).

2.2.2. Nickel phosphide ($\text{Ni}_2\text{P}/\text{SiO}_2$) synthesis

The $\text{Ni}_2\text{P}/\text{SiO}_2$ catalyst was prepared by temperature-programmed reduction (TPR), following procedures reported previously [35, 38, 39]. Briefly, the synthesis of the catalysts involved two stages. First, a solution of the corresponding metal phosphate precursor was prepared by dissolving appropriate amounts of $\text{Ni}(\text{NO}_3)_2 \cdot 6\text{H}_2\text{O}$ with ammonium phosphate in distilled water, and the solution was used to impregnate silica by the incipient wetness method. The obtained samples were dried and calcined at 773 K for 6 h, then ground with a mortar and pestle, pelletized with a press (Carver, Model C), and sieved to particles of 650–1180 μm diameter (16/20 mesh). Second, temperature-programmed reduction (TPR) was carried out on the pelletized precursor phosphate (typically 200mg) placed in a U-shaped quartz reactor. The sample was heated from room temperature to 1073 K at 2 K min^{-1} in flowing hydrogen at $100 \text{ cm}^3 (\text{NTP}) \text{ min}^{-1} \text{ g}^{-1}$ to reduce the metal phosphate to the desired phosphide and to determine the

peak maximum for reduction. A portion of the exit gas flow was sampled through a leak valve into a mass spectrometer (MS, Dycor/Ametek, model MA100) and the masses 2(H_2), 18(H_2O), 31(P) and 34(PH_3) were monitored during the experiment. For large sample sizes sample was kept at the determined peak reduction temperature (883 K) for 2 h, followed by cooling to room temperature under He flow [$100 \text{ cm}^3 \text{ (NTP) min}^{-1}$], and then passivated at room temperature in a 0.5% O_2/He for 4 h. The Ni molar loading was 1.156 mmol per g of support, corresponding to a weight loading of Ni_2P of 7.9 wt% with an initial Ni/P ratio of 1/2.

2.2.3. Characterization

Irreversible CO uptake measurements were used to provide an estimate of the active sites on the catalysts. Usually, 200 mg of a passivated $\text{Ni}_2\text{P}/\text{SiO}_2$ catalyst was loaded into a U-shaped quartz reactor and then the sample was reduced in flowing H_2 [$200 \text{ cm}^3 \text{ (NTP) min}^{-1}$] at 723 K for 2 h. For HZSM-5 the pretreatment temperature was 773 K using He as the purging gas. After cooling in He [$200 \text{ cm}^3 \text{ (NTP) min}^{-1}$], pulses of CO in a He carrier at $43 \mu\text{mol s}^{-1}$ [$65 \text{ cm}^3 \text{ (NTP) min}^{-1}$] were injected at room temperature through a sampling valve. The mass 28 (CO) signal was monitored with a mass spectrometer (MS, Dycor/Ametek, model MA100). CO uptake was calculated by measuring the decrease in the peak areas caused by adsorption in comparison with the area of a calibrated volume ($19.5 \mu\text{mol}$).

Surface areas of the samples were obtained using the BET method based on adsorption isotherms at liquid nitrogen temperature, using a value of 0.162 nm^2 for the cross-sectional area of a N_2 molecule. The measurements were performed in a volumetric adsorption unit (Micromeritics ASAP 2000). X-ray diffraction (XRD) patterns of the samples were obtained with

a PANalyticalX'pert Pro powder diffractometer operated at 45kV, using Cu K α monochromatized radiation ($\lambda=0.154178\text{nm}$).

Transmission infrared spectra of pyridine adsorbed on the Ni₂P/SiO₂ catalyst and HZSM-5(Si/Al=15) were collected to characterize the surface acidic sites. Fourier transform infrared (FTIR) spectra measurement were carried out with a Digilab Excalibur Series FTS 3000 spectrometer equipped with a liquid N₂ cooled mercury-cadmium-telluride detector. The IR cell was equipped with water cooled KBr windows, connections for inlet and outlet flows, and thermocouples connected to a temperature controller to monitor and control the sample temperature. For the experiments, about 25 mg of finely ground Ni₂P/SiO₂ catalyst, or HZSM-5 samples were pressed into self-supporting wafers with a diameter of 13 mm (18.8 mg cm⁻²). Wafers were mounted vertically in a quartz sample holder to keep the incident IR beam normal to the sample. Before dosing pyridine, the sample of Ni₂P/SiO₂ was reduced in H₂ and HZSM-5 was purged in He flow at 723 K and 773 K, respectively, for 2 h at a flow rate of 100 $\mu\text{mol s}^{-1}$ [150 cm³ (NTP) min⁻¹]. After pretreatment, the samples were slowly cooled in flowing He [200 cm³ (NTP) min⁻¹] and background spectra were collected at 423K under He flow. The samples were dosed at atmospheric pressure and room temperature with 1.0 mol % pyridine in He carrier at a total flow rate of 140 $\mu\text{mol s}^{-1}$ [200 cm³ (NTP) min⁻¹] until saturation was achieved. The samples were then purged with carrier gas for 0.5 h to remove gaseous and weakly adsorbed pyridine. Spectra were acquired at 423 K and are shown with subtraction of the background contribution to highlight the pyridine adsorbate peaks.

Ethanol FTIR measurements were carried out with Ni₂P/SiO₂ catalyst in the same manner as with the pyridine experiments. After pretreatment background spectra were collected under He flow, and then ethanol was introduced with He flow until saturation was achieved.

Ammonia, pyridine and carbon dioxide temperature-programmed desorption (NH₃-TPD, pyridine-TPD and CO₂-TPD) were used to determine the quantities of acid and base sites on the catalysts. TPD experiments were carried out by loading catalyst samples (200 mg) in U-shaped quartz reactors connected to a MS pretreating as in the CO uptake experiments, and then dosing NH₃ or CO₂ or a mixture of 2.6 mol% pyridine in dry He flow from a bubbler containing pyridine at room temperature onto the samples at room temperature until saturation. Then samples were purged with pure He for 1 h at a flow rate of 200 cm³(NTP) min⁻¹ to remove physisorbed NH₃ or pyridine or CO₂, then heated from room temperature to 973 K at 10 K min⁻¹. The masses 17(NH₃) or 79(pyridine) or 44(CO₂) were monitored by the MS during the experiments. Peak areas were quantified by comparison to the areas of calibrated pulses of the pure compounds.

Ethanol temperature programmed desorption (EtOH-TPD) was used to compare the catalytic activity and product selectivity of ethanol over the two different catalysts. To start a reaction, catalysts (200 mg) were placed in a U-shaped reactor and pretreated at the same conditions as used for chemisorption. After pretreatment, a flow of He saturated with ethanol was introduced at 200 cm³ (NTP) min⁻¹ for 1 h at room temperature. After purging in He flow for 1 h, the temperature was raised at 10 K min⁻¹ to 1073 K in He flow [200 cm³ (NTP) min⁻¹]. The reaction products were analyzed using an online mass spectrometer (Dycor/Ametek, model MA100). The conversion of ethanol and the product selectivity for each sample were calculated and compared. The products were quantified using reaction response factors (RRF). The RRF were determined experimentally calibrating the mass spectrometer signals with pure standards of known concentration.

2.2.4. Reactivity Studies

Activity tests were conducted in a U-shaped reactor at atmospheric pressure using catalyst amounts corresponding to 121 μmol of active sites. For nickel phosphide the catalyst amount (903 mg) was based on the CO uptake ($134 \mu\text{mol g}^{-1}$) and for HZSM 5 the catalyst amount (214 mg) was based on the NH_3 uptake ($565 \mu\text{mol g}^{-1}$). To start, the catalyst was pretreated at the same conditions as used for chemisorption. After pretreatment, a mixture of 1.5 mol% ethanol in dry He flow from a bubbler containing ethanol at 273 K was passed onto the sample, and then the catalyst was stabilized for 0.5 h after the feed was introduced. Reactivity testing was performed as a function of temperature, starting at the highest temperature of 523 K and was varied downwards and upwards with the initial temperature repeated at the end, to establish catalyst stability. Mass balances closed within 5%.

Reactivity tests were also investigated as a function of contact time. The contact time is defined by the following equation, with the quantity of sites obtained from CO uptake experiment.

$$\text{Contact time [s]} = \frac{\text{Quantity of sites } [\mu\text{mol g}^{-1}] \times \text{Catalyst weight [g]}}{\text{Reactant flowrate } [\mu\text{mol s}^{-1}]}$$

The experiment started at the highest contact time of 270 s and was varied downwards and upwards with the initial contact time repeated at the end. Generally it took about 10 h of on stream time to collect the rate data at several reaction temperatures or contact times, and the smoothness of the data indicated no deactivation. The reaction products were analyzed using an online mass spectrometer (Dycor/Ametek, model MA100). The conversion and product yield

were evaluated by determining the amount of ethanol reacted and products formed using the formulas below.

$$\text{Conversion [\%]} = \frac{N(\text{ethanol})_{\text{in}} - N(\text{ethanol})_{\text{out}}}{N(\text{ethanol})_{\text{in}}} \times 100$$

$$\text{Yield [\%]} = \text{Fractional conversion} \times \text{Selectivity} \times 100$$

2.3. Results and Discussion

2.3.1. Synthesis and basic characterization

The supported nickel phosphide was prepared in two stages as described in the experimental part. First, solutions of the nickel and phosphorous components were impregnated on the silica support and the material was dried to form supported phosphate precursors. Second, the phosphate was transformed into a phosphide by temperature-programmed reduction (TPR). The TPR experiment was carried out to understand the phenomena involved in the reduction process and to determine the optimum reduction condition used for large scale catalyst preparation (Fig. 2.1a). A sample of HZSM-5 was also included in the studies because it is among the most effective of reported catalysts, and serves as a comparison to the Ni₂P material. Modification of ZSM-5, though interesting, would detract from the treated subject.

Only the results for mass 18 (H₂O) are shown, because the other monitored masses provided little additional information. The water evolution (mass 18) shows a reduction peak at

883 K. This temperature was chosen for preparation of larger scale samples used for characterization and testing.

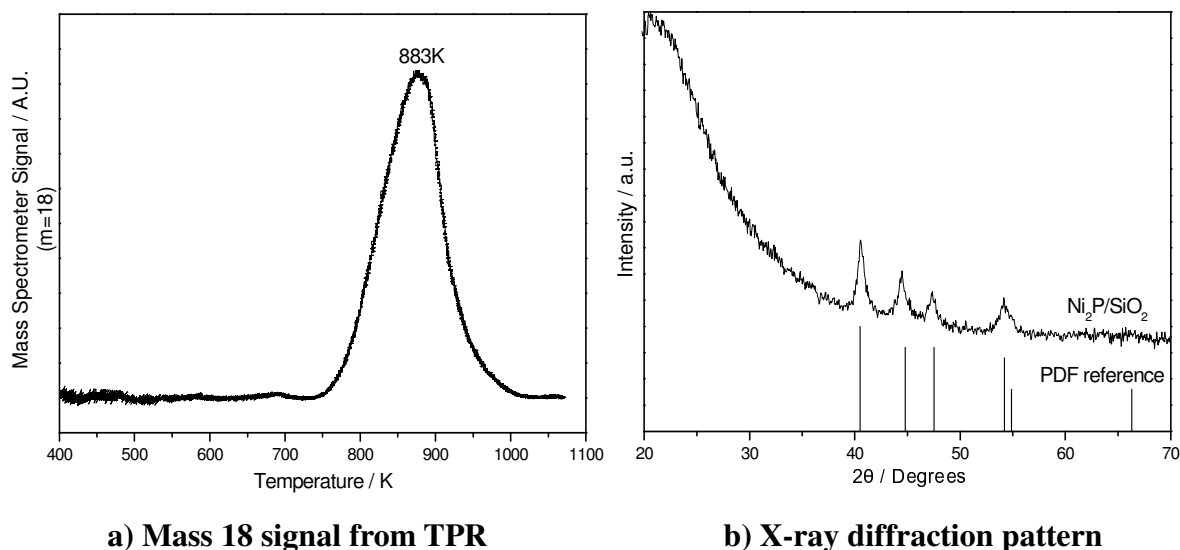


Fig. 2.1. Synthesis and XRD Analysis of Ni₂P/SiO₂.

Analysis of the product of TPR was carried out by XRD (Fig. 2.1b). The diffraction pattern for the silica supported nickel phosphide shows three major peaks at 40.5°, 44.8° and 47.5°, which line up well with the standard pattern for Ni₂P. The peaks are significantly broadened indicating that small Ni₂P crystals were formed. The XRD pattern after reaction was essentially unchanged, indicating that the catalyst was stable.

The width at half-maximum was corrected for instrumental broadening (0.2°) and the crystallite size of the supported Ni₂P was calculated using the Scherrer equation, $D_C = \frac{K\lambda}{\beta \cos(\theta)}$, where K is a constant taken as 0.9, λ is the wavelength of the X-ray radiation (0.154178 nm), β is the peak width in radians at half-maximum, and 2θ is the Bragg angle. Table 2.1 reports the true width at half-maximum of the peak and the crystallite size.

Table 2.1. The true width at half-maximum of the peak and crystallite size of Ni₂P/SiO₂ catalyst

Peak / degree	Direction	True width / rad	Crystallite size / nm
40.5	111	0.009	17
44.8	201	0.007	22
47.5	210	0.006	25
54.2	300	0.010	15
Average	--	0.008	20

There is no substantial anisotropy with crystallographic direction, indicating that the crystallites are spherical, in agreement with high resolution transmission electron microscopy results from the group of Bussell [40].

The CO chemisorption and BET characterization results are reported in Table 2.2. Earlier studies have shown that uptakes of CO on SiO₂ and Al₂O₃ were negligible [41-43]. The CO chemisorption uptake of the Ni₂P/SiO₂ catalyst was 134 $\mu\text{mol g}^{-1}$, which is in line with previous measurements. The CO uptake of HZSM-5 was small, and was probably due to CO interaction with strong Lewis acid sites, as HZSM-5 does not contain metal. Both the phosphide and the HZSM-5 samples have high BET surface areas, 310 and 410 $\text{m}^2 \text{g}^{-1}$, respectively. The BET surface area of Ni₂P/SiO₂ is lower than that of the SiO₂ support of 350 $\text{m}^2 \text{g}^{-1}$, and this was likely caused by sintering during the preparation process. Additionally, Table 2.2 also lists the pore volumes of the two catalysts obtained from N₂ physisorption measurements and shows that the major types of pores in Ni₂P/SiO₂ and HZSM-5 catalysts are mesopores and micropores, respectively.

Table 2.2. Characterization results for HZSM-5 and Ni₂P/SiO₂ catalysts

Catalyst	CO-Uptake $\mu\text{mol g}^{-1}$	BET area $\text{m}^2 \text{g}^{-1}$	Pore Volume ($\text{cm}^3 \text{g}^{-1}$)		
			$V_{\text{micro}}^{\text{a}}$	$V_{\text{meso}}^{\text{b}}$	V_{tot}
Ni ₂ P/SiO ₂	134	310	0.009	0.083	0.092
HZSM-5	11	410	0.124	0.036	0.160

^aMicropore volume from t-plot^b $V_{\text{total}} - V_{\text{micro}}$

It has been reported [44] that micropores are associated with coke formation that results in the zeolite's loss of activity during the ethanol dehydration process. The micropore size limits the size of the channels, cavities, and channel intersections, trapping the species responsible for coking. Mesopores are more active in the ethanol reaction, for the larger size allows easier passage of the reactant for reaching the active sites and for the products to leave. Gayubo et al. [45] studied the selectivity of olefin products from bioethanol and demonstrated that higher mesoporosity and moderate acid strength were suitable for the decomposition of bioethanol.

2.3.2. Temperature-programmed desorption (TPD) of NH₃, pyridine, and CO₂

Measurements of NH₃ [46, 47], pyridine-, and CO₂- [48, 49] temperature - programmed desorption (TPD) were carried out in order to clarify the relationship between the catalyst activity and the amount of acidic and basic sites on the catalysts. The results are shown in Figs.2-4 and summarized in Table 2.3. Although the signal is reported with arbitrary units, the peaks were quantitated by injection of known quantities of NH₃, pyridine, and CO₂.

Relevant to the NH₃-TPD results, previous studies showed that [50] peak maxima, T_m , from 293 K to 473 K correspond to weak acidity sites, T_m from 473 K to 673 K to intermediate acidity sites, and T_m higher than 673 K to strong acidity sites. The HZSM-5 sample shows two peaks at T_m of 500 K and 724 K, respectively (Fig. 2.2), clearly suggesting the presence of

moderate and strong acidic sites. The ratio of the moderate acidic sites to the strong ones is 0.75. Bi et al. [51] and Post and Hoof [52] reported that ethylene was easily polymerized on the strong Brønsted acid sites of HZSM-5, and suggested that elimination of the strong acidic sites could improve the stability of the catalyst. The $\text{Ni}_2\text{P}/\text{SiO}_2$ catalyst exhibits one broad peak from 402 K to 805 K with a maximum around 475 K, indicating that the catalyst has plenty of moderate acidity sites. The acid sites are probably associated with phosphorus on the support. In summary, the NH_3 -TPD characterization results show that Ni_2P has weak and moderate strength acid sites, while HZSM-5 has stronger acid sites the strongest of which might lead to side reactions.

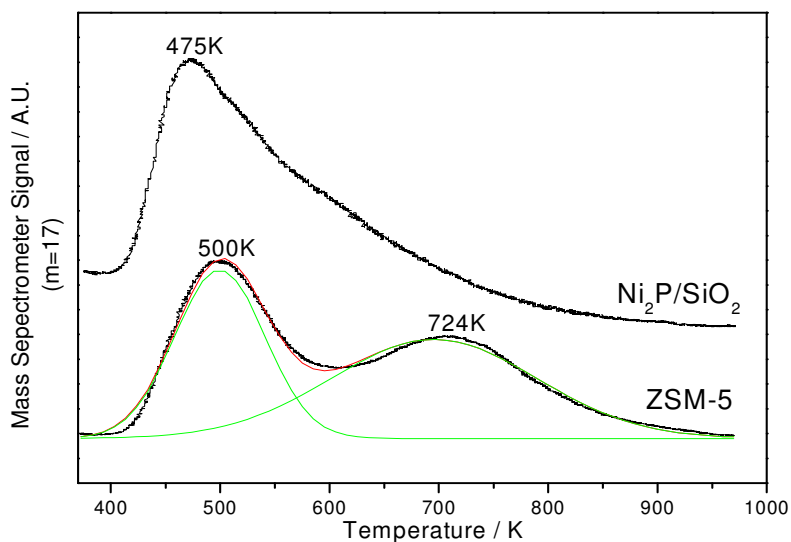


Fig. 2.2. Mass 17 signal from NH_3 -TPD

Previous references noted that [53, 54] pyridine is a strong base in the gas phase and requires higher temperature for complete desorption than ammonia from catalysts. Figure 3 displays the pyridine-TPD profiles and shows that all peak maxima occur at higher temperature than the corresponding NH_3 -TPD maxima (530 K for $\text{Ni}_2\text{P}/\text{SiO}_2$, 514 K and 991 K for HZSM-5, respectively). The conclusions are similar to those obtained with NH_3 -TPD, with $\text{Ni}_2\text{P}/\text{SiO}_2$

exhibiting moderate strength acidic sites and HZSM-5 possessing both moderate and strong acidic sites in a ratio of 0.60.

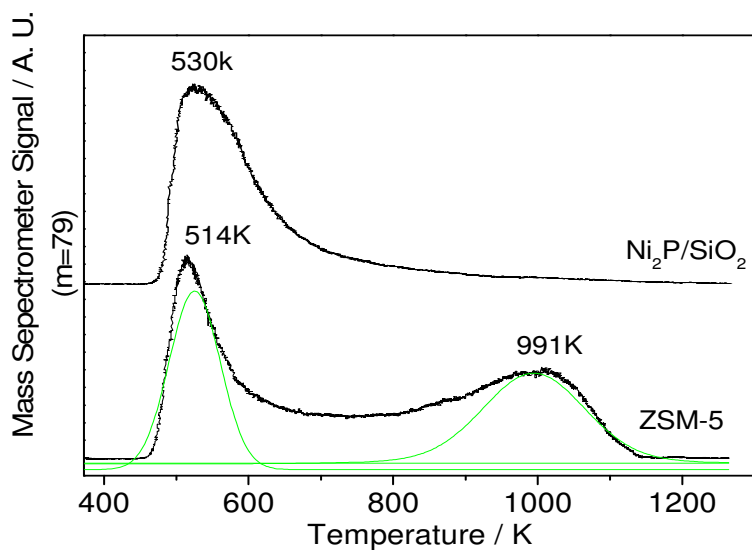


Fig. 2.3. Mass 79 signal from pyridine-TPD

Figure 2.4 shows the TPD profiles of CO₂ from the Ni₂P/SiO₂ and HZSM-5 samples, with peak maxima located at 389 K and 373 K, respectively. Table 2.3 summarizes the quantity of acidic and basic sites. The results suggest that Ni₂P/SiO₂ has fewer acidic sites and more basic sites than HZSM-5. Previous FTIR characterization of acid sites indicate that there are Si-OH and P-OH groups on the support that contribute to the total acidity [55-57]. The quantity of probe molecules on HZSM-5 is generally larger than on the Ni₂P/SiO₂, reflecting the large contribution of the total surface of the material to the adsorption.

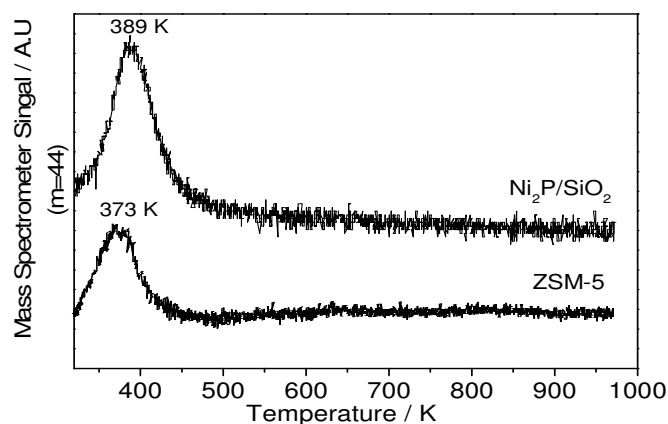


Fig. 2.4.. Mass 44 signal from CO₂-TPD

The influence of acidic and basic centers on dehydration has been well studied. Basic and acidic sites are necessary for the dissociative adsorption of ethanol [58, 59]. Golay et al. [60] investigated the influence of the catalyst's acid/base properties on the catalytic ethanol dehydration. They suggested that for the formation of ethylene a simultaneous adsorption on both acidic sites and basic sites was necessary and that the dehydration was affected by both the surface acidity and by the sorption kinetics on the basic sites.

2.3.3. Infrared spectroscopy of pyridine

Pyridine adsorption is often combined with in situ Fourier transform infrared spectroscopy (FTIR) to probe the surface acidic properties of supports and catalysts [61, 62]. Characteristic bands in the FTIR spectrum are used to determine if pyridine is protonated through the nitrogen atom by surface Brønsted acid sites and/or bonded to coordinative unsaturated metal sites (Lewis acids). Upon interaction with a Brønsted acid site, pyridine is protonated to a pyridinium ion and

absorbs with a characteristic band around 1545 – 1540 cm^{-1} . Interaction of pyridine with Lewis acid sites leads to a coordinatively bonded pyridinium complex with a well-resolved band centered around 1452 – 1447 cm^{-1} . A band located around 1490 cm^{-1} is common to both adsorbed species. Many studies have employed this technique to qualitatively and quantitatively study the acidic properties of catalytic materials and the resulting effect on catalyst properties and activity. Figure 2.5 displays FTIR spectra of adsorbed pyridine in He flow on HZSM-5 and $\text{Ni}_2\text{P}/\text{SiO}_2$ catalysts at 423 K and shows that both possess acidic sites. HZSM-5 contains mostly Brønsted acid sites whereas $\text{Ni}_2\text{P}/\text{SiO}_2$ has more Lewis acid sites.

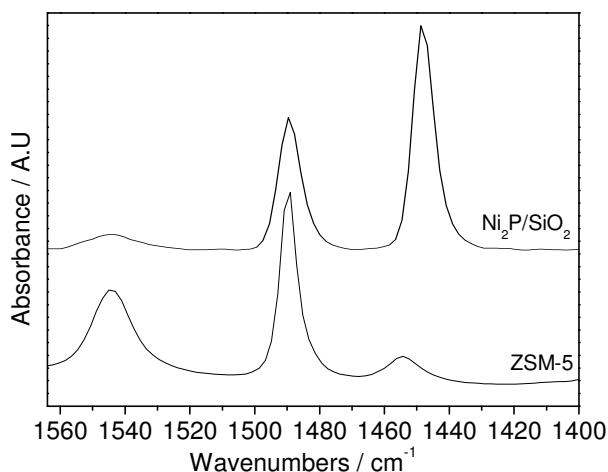


Fig. 2.5. Infrared spectra of adsorbed pyridine over samples at 423 K

The quantity of Brønsted acid sites and Lewis acid sites were calculated using the following equations [63], and the results are presented in Table 3.

$$C(B) = \text{IMEC}(B)^{-1} \times \text{IA}(B) \times \pi R^2 / W$$

$$C(L) = \text{IMEC}(L)^{-1} \times \text{IA}(L) \times \pi R^2 / W$$

Where: C: Concentration ($\mu\text{mol}/\text{g}$ catalyst).

IMEC(B, L): Integrated molar extinction coefficients (cm/ μmol).

IA(B, L): Integrated absorbances (cm^{-1}).

R: Radius of catalyst disk (cm).

W: Weight of disk (mg)

Table 2.3. Acid and base properties for HZSM-5 and Ni₂P/SiO₂ catalysts

Samples	CO ₂ -TPD $\mu\text{mol g}^{-1}$	NH ₃ -TPD $\mu\text{mol g}^{-1}$	Pyridine-FTIR			
			B / $\mu\text{mol g}^{-1}$	L / $\mu\text{mol g}^{-1}$	B+L / $\mu\text{mol g}^{-1}$	B/L
Ni ₂ P/SiO ₂ *	408	381	36	290	326	0.12
HZSM-5	218	565	428	58	486	7.38

* The Ni₂P/SiO₂ CO₂-TPD amount is corrected by 149 $\mu\text{mol g}^{-1}$ from the SiO₂ support and the NH₃-TPD amount is corrected by 229 $\mu\text{mol g}^{-1}$ from the SiO₂ support.

Comparing the quantity of acid sites obtained by the TPD and FTIR methods, it is found that on Ni₂P the NH₃ TPD amount (381 $\mu\text{mol g}^{-1}$) is slightly larger than the pyridine FTIR amount (326 $\mu\text{mol g}^{-1}$). This also is found on HZSM-5 where the TPD amount (565 $\mu\text{mol g}^{-1}$) is larger than the pyridine FTIR amount (486 $\mu\text{mol g}^{-1}$). There are two possible reasons for this. First, ammonia is smaller than pyridine, so it will pack more closely on the surface as well as enter more readily into smaller micropores. Second, the purge temperature of ammonia was room temperature whereas that of pyridine in the FTIR measurements was 423 K, so that some weakly bound pyridine was desorbed.

Phillips and Datta [22] reported that Brønsted acid sites were involved in the HZSM-5 catalyzed ethanol dehydration to ethylene; however, oligomerization of ethylene also occurred at

the same sites forming carbonaceous deposits that covered these sites and dramatically reduced the catalytic activity. Increasing Lewis acid sites and decreasing Brønsted acid sites were favorable for the catalytic decomposition of ethanol [21, 64].

The number of sites titrated by CO₂ is surprisingly high. For Ni₂P the quantity (408 μmol g⁻¹) exceeds the acidic sites (381 μmol g⁻¹) and the surface metal sites from CO chemisorption (134 μmol g⁻¹). For HZSM-5 the quantity of CO₂ adsorption (218 μmol g⁻¹) is about 1/3 the total acid amount (565 μmol g⁻¹). The adsorption of CO₂ is usually attributed to basic sites, but in this case for Ni₂P there is likely to be some adsorption on the metallic sites. For both Ni₂P and HZSM-5 there are likely contributions from physisorption.

2.3.4. Ethanol temperature-programmed desorption

Figures 2.6a and b show the signal of ethylene and acetaldehyde, respectively, obtained from ethanol temperature programmed desorption (EtOH-TPD). Figure 2.6a shows that ethylene formation over HZSM-5 occurred at around 419 K and 533 K, and over Ni₂P/SiO₂ occurred at around 407 K and 584 K. Thus, ethylene started to form and desorb from the Ni₂P/SiO₂ catalyst at a lower temperature than from HZSM-5.

Figure 2.6b reveals the desorption of acetaldehyde. The formation of acetaldehyde over HZSM-5 occurred at around 422 K and 541 K. Over Ni₂P/SiO₂ acetaldehyde desorbed at 411 K and 497 K.

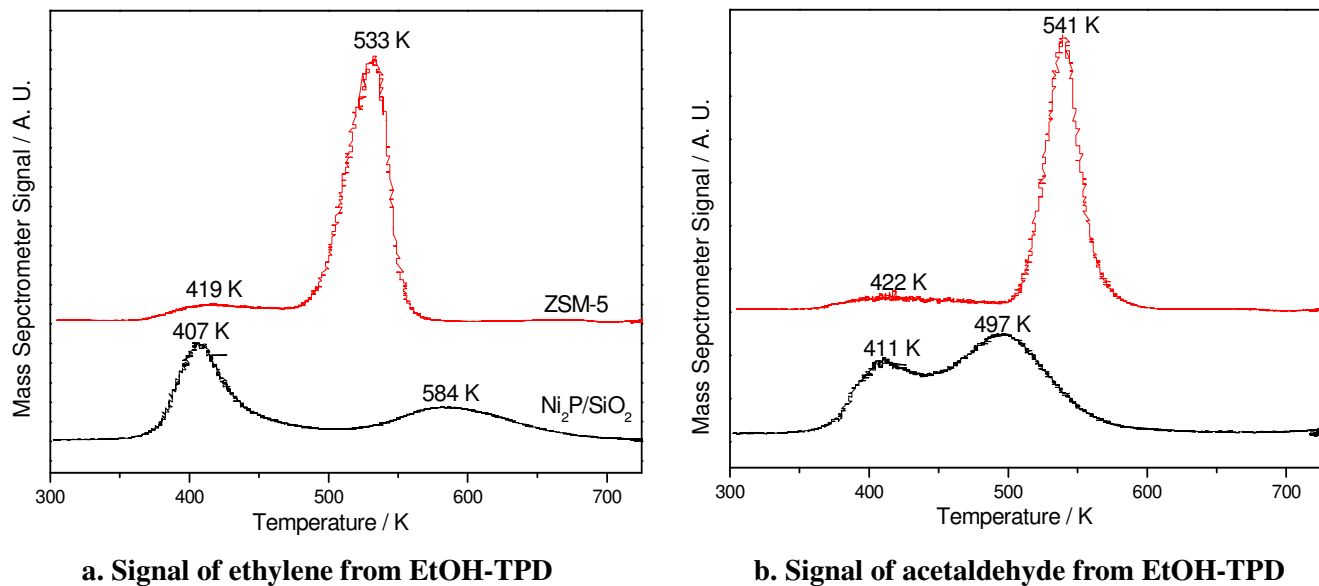


Fig. 2.6. Infrared spectra of adsorbed pyridine over samples at 423 K

Table 2.4 summarizes the distribution of ethylene and acetaldehyde over different temperatures in the EtOH-TPD experiments over HZSM-5 and Ni₂P/SiO₂ catalysts.

Table 2.4. Distribution of ethylene and acetaldehyde in different temperature ranges on EtOH-TPD

Catalyst	HZSM-5				Ni ₂ P/SiO ₂			
	Maximum Temperature / K	419	422	533	541	407	411	497
Percentage of ethylene / %	20	--	80	--	50	--	--	50
Percentage of acetaldehyde / %	--	16	--	84	--	28	72	--

Over HZSM-5, strong ethylene and acetaldehyde desorption were recorded at 530 K and 541 K, respectively. Over Ni₂P/SiO₂ an almost similar amount of ethylene was observed at 407

K and 584 K, and acetaldehyde desorption occurred primarily at 497 K, with a smaller peak at 411 K. The $\text{Ni}_2\text{P}/\text{SiO}_2$ catalyst shows reactivity at lower temperature than HZSM-5 particularly for acetaldehyde, which indicates it may be an initial product. This will be confirmed later.

Figure 2.7 shows the conversion of ethanol and the selectivity towards products from EtOH-TPD over the two catalysts.

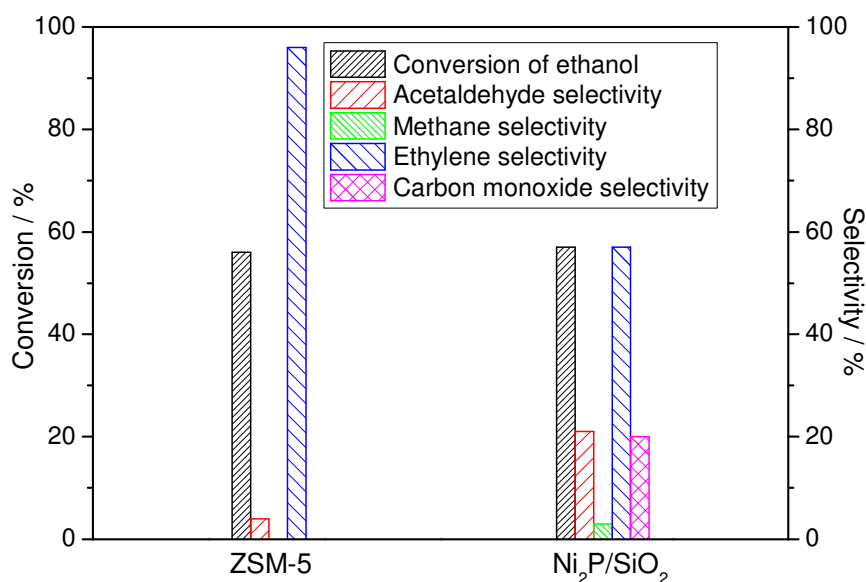


Fig. 2.7. Conversion and Selectivity from EtOH-TPD

Overall, $\text{Ni}_2\text{P}/\text{SiO}_2$ has a little higher conversion of ethanol (57%) than HZSM-5 (56%), but also exhibits a higher selectivity towards acetaldehyde (21%) than HZSM-5 (4%), and a lower selectivity towards ethylene (57%) than HZSM-5 (96%). At the same time, carbon monoxide, a product of conversion from acetaldehyde was detected at up to 20% in the product stream on the $\text{Ni}_2\text{P}/\text{SiO}_2$ catalyst along with a small quantity of methane (3%). In contrast, there was no carbon monoxide and methane detected from HZSM-5. The decomposition of ethanol

has been studied extensively on different metallic catalysts such as Pt/Al₂O₃ [65], CuO with 5% CoO and 1% Cr₂O₃ [66], Pt/ZrO₂ [67] and supported Au [68], and it has been reported that the dehydrogenation of ethanol yielded acetaldehyde and hydrogen: C₂H₅OH → CH₃CHO + H₂ (1). It is likely that the methane detected with the Ni₂P/SiO₂ came from an intermediate acetaldehyde which decomposed to methane and carbon monoxide: CH₃CHO → CH₄ + CO (2). It should be noted that in the presence of water (a dehydration by-product) the CH₄ steam reforming reaction may also occur to produce CO and H₂: CH₄ + H₂O → CO + 3H₂ (3). Farkas and Solymosi [69] studied the adsorption, desorption and dissociation of ethanol on MoC/Mo(100). They obtained a product mixture of 18% of ethylene, 12% of acetaldehyde and 44% of carbon monoxide. The formation of methane, however, was not reported. They suggested the reason for no methane formation was that no CH_x species formed from rupture of a C-C bond on the catalyst surface during the dehydrogenation process. These results are in agreement with the finding from this study that the amount of methane was much smaller than that of carbon monoxide.

Under our conditions of EtOH-TPD, the Ni₂P/SiO₂ displayed better ability for the conversion of ethanol and selectivity towards dehydrogenation than HZSM-5. Dehydrogenation is generally accepted to occur on basic sites and metallic sites. On Ni₂P the uptake of CO₂ is substantial (Table 3), but as discussed earlier, some of this may be due to chemisorption on metallic sites, and a considerable portion in physisorbed mode. It is more likely, from the known hydrogen transfer capabilities of the phosphide that dehydrogenation is occurring on metallic sites.

In order to ensure that the TPD results were not affected by the lag time for gas to diffuse out of pores, an analysis was carried using the criterion of Gorte [70] and Ibok and Ollis [71]. These researchers suggested that the effect of diffusion limitations could be ignored for a value

of less than 0.01 for the group $\frac{\beta l^2 \varepsilon}{(T_f - T_0) D}$, where β is the heating rate (K/s), l is the width of catalyst slab (cm), ε is the porosity (cm^3/cm^3), T_f and T_0 are the final and initial temperature (K), respectively, and D is effective diffusivity (cm^2/s). For our conditions a highest value of 6×10^{-5} is obtained (Table 5), and this indicates no diffusion limitations during the TPD experiments.

Table 2.5. Parameters in the Gorte Criterion

β	Heating rate / Ks^{-1}	0.17
l	Width of catalyst slab / cm	0.09
ε	Porosity / $\text{cm}^3 \text{cm}^{-3}$	0.45
$T_f - T_0$	Temperature difference / K	110
D	Effective diffusivity	0.1

2.3.5. Reactivity

The conversion of ethanol as a function of temperature was compared for HZSM-5 and $\text{Ni}_2\text{P}/\text{SiO}_2$ with equal sites loaded in the reactor ($121 \mu\text{mol g}^{-1}$). For HZSM-5 the main product at all temperatures was ethylene, with some acetaldehyde and a butylene isomer (not identified) also formed. On $\text{Ni}_2\text{P}/\text{SiO}_2$ the main product was initially acetaldehyde, but this decreased with increasing temperature and ethylene became the main product at high temperature. These results are consistent with previously studies [25-30]. In general $\text{Ni}_2\text{P}/\text{SiO}_2$ exhibited higher activity than HZSM-5 at all temperatures. Turnover frequencies were obtained from:

$$\left(\text{Turnover frequency } [\text{s}^{-1}] = \frac{\text{Reactant flowrate } [\mu\text{mol s}^{-1}] \times \text{Conversion}}{\text{Quantity of sites } [\mu\text{mol g}^{-1}] \times \text{Catalyst weight } [\text{g}]} \right)$$

A summary is provided in Table 2.6. Calculations of the Weisz–Prater Criterion (C_{WP}) were made to ascertain that no mass transfer limitations were present. The highest C_{WP} gave $0.030 \ll 1$, indicating that internal mass transfer effects can be neglected at the conditions employed for the reactivity study in this paper.

Table 2.6. Reactivity in ethanol deoxygenation (Contact time = 162 s)

Catalyst	Conversion / %			
	448 K	473 K	498 K	523 K
Ni ₂ P/SiO ₂	41	54	86	100
HZSM-5	9	25	68	91
	Turnover frequency / s ⁻¹			
Ni ₂ P/SiO ₂	0.0025	0.0033	0.0053	0.0062
HZSM-5	0.00057	0.0016	0.0042	0.0056

Apparent activation energies were calculated from fits to the conversion curves at low conversion and were 39 kJ mol⁻¹ for HZSM-5 and 46 kJ mol⁻¹ for Ni₂P/SiO₂.

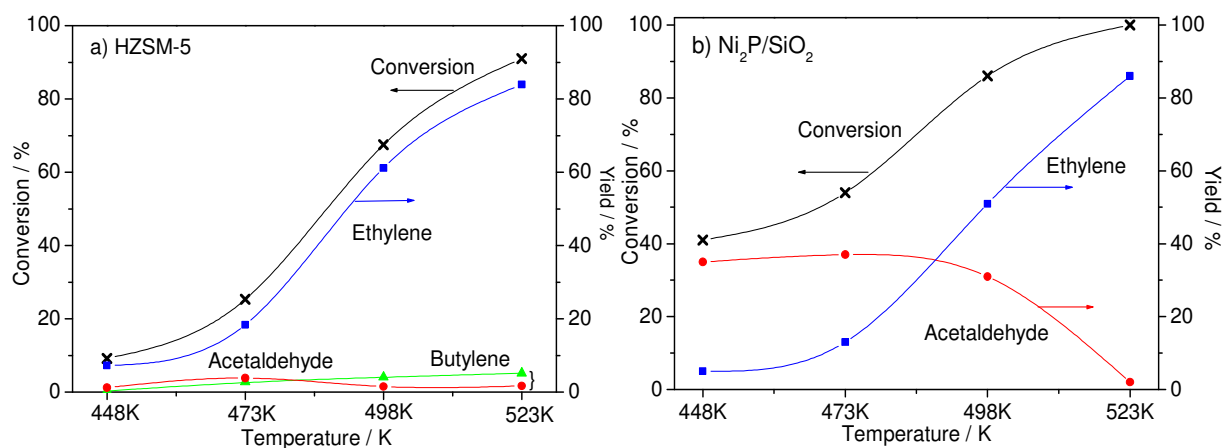


Fig. 2.8. Variation of ethanol conversion and product yield as a function of reaction temperature at a contact time of 162 s. a) HZSM-5 b) Ni₂P/SiO₂

Figure 2.9 shows the ethanol conversion and product yields as a function of contact time over the HZSM-5 catalyst at 473 and 498 K. It can be seen that the conversion increased with time and temperature, as expected. The product formed in highest yield was ethylene. At 473 K (Fig. 2.9a) the ethylene decreased slightly at high contact time, and this was accompanied by a corresponding growth in butylenes, indicating that part of the ethylene might have been consumed to form the C₄ products. Acetaldehyde was produced at low contact time together with ethylene, suggesting that these C₂ species were produced in parallel. However, acetaldehyde did not grow appreciably with time suggesting that it was an intermediate that also reacted to form the butylenes. At 498 K (Fig. 2.9b) ethylene grew monotonically with contact time. Acetaldehyde was formed in small amounts and went through a shallow maximum at short contact time, confirming that it is an intermediate. The butylenes were formed in small but growing amounts indicating that they were final products. Overall, the results indicated that

ethylene and acetaldehyde are formed in parallel, and react by a condensation reaction to form butylenes. At higher temperatures the ethylene was the preferred product and the acetaldehyde was largely consumed to form the butylenes resulting in a smaller acetaldehyde yield than at lower temperatures.

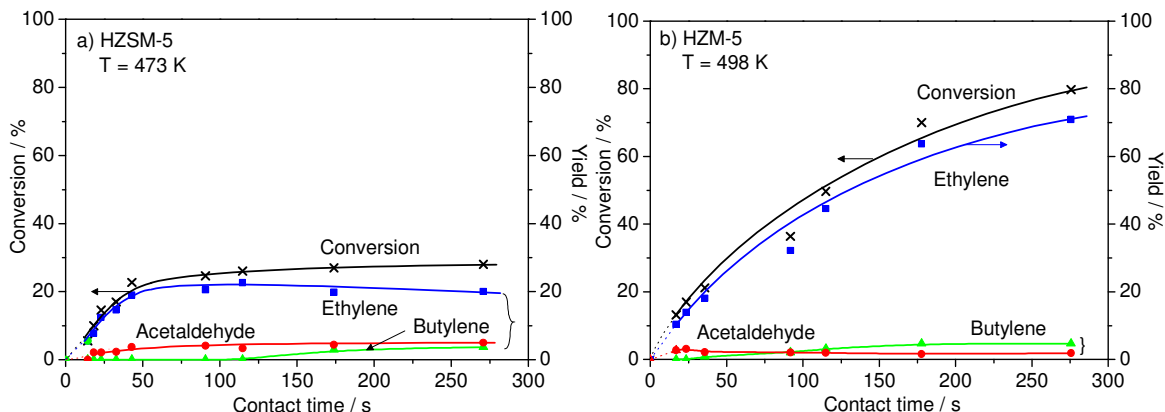


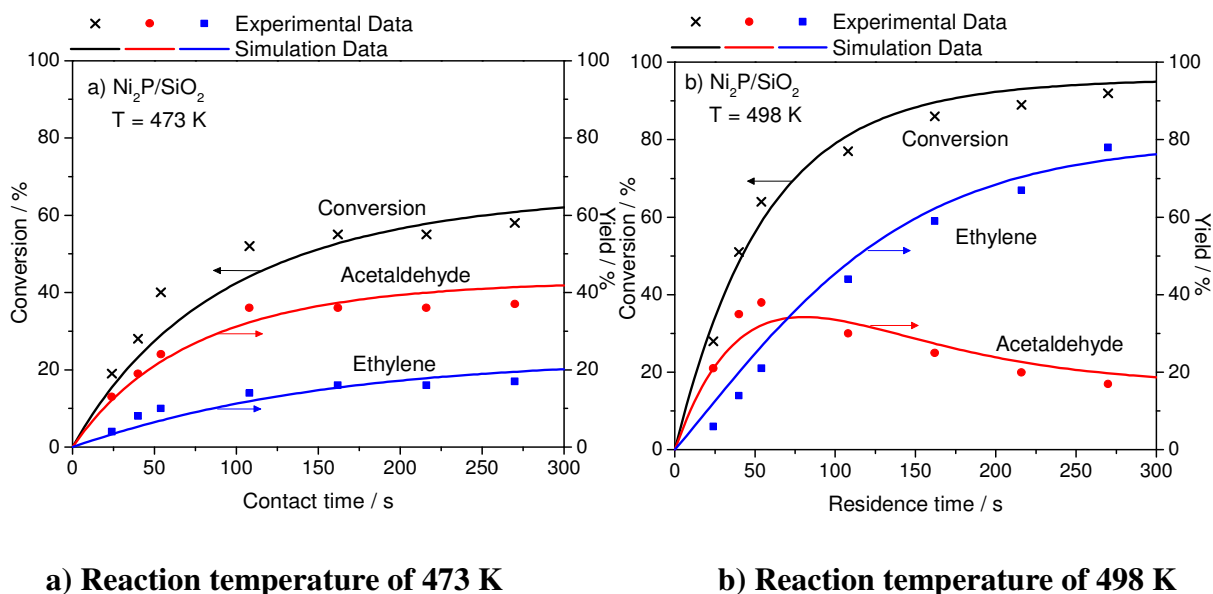
Fig. 2.9. Variation of ethanol conversion and product yield as a function of contact time on HZSM-5. a) Reaction temperature of 473 K b) Reaction temperature of 498 K

Figure 2.10 shows the ethanol conversion and yields of acetaldehyde and ethylene as a function of contact time at 473 and 498 K on $\text{Ni}_2\text{P}/\text{SiO}_2$. The curves are fits to the data that will be discussed later. The figure indicates that conversion and the yields of products increase with contact time. The data at 473 K (Fig. 2.10a) show both ethylene and acetaldehyde growing with time. From these data alone it is not possible to deduce the sequence of reaction steps. Indeed, it could be that acetaldehyde and ethylene are produced in parallel. As will be shown, this is not the case. The data at 498 K (Fig. 2.10b) this time shows that acetaldehyde goes through a maximum, while ethylene rises monotonically, behaviors characteristic of a sequential network. This result is in accordance with a previous report [72] in which the conversion of ethanol

increased with increasing contact time along with a drop in acetaldehyde selectivity. As will be discussed in the modeling section, both sets of data can be described by a reaction sequence involving adsorbed intermediates undergoing consecutive reactions.

It should be emphasized that the measurements were carried out by varying the contact time up and down over a period of 10 h so that the smoothness of the data provide evidence for the lack of deactivation. This fact and the establishment of a mass balance of $100 \% \pm 5\%$ indicate that the maximum in acetaldehyde yield is not due to its consumption to form products such as butylenes (not detected) or heavy materials like polymers.

It should be noted that no ethane was detected. At the conditions of this study the concentration of the ethanol reactant is low (1.5 mol%), and since the concentration of products is significantly lower, it is difficult for the hydrogen (from dehydrogenation) and ethylene (from dehydration) to come into contact to form ethane. Furthermore, the ethane formation reaction is favored by high temperature and pressure, which are not the conditions employed in our study. Thus, the lack of formation of ethane is understandable. Other studies report acetaldehyde and ethylene formation but not ethane [20, 26].



a) Reaction temperature of 473 K

b) Reaction temperature of 498 K

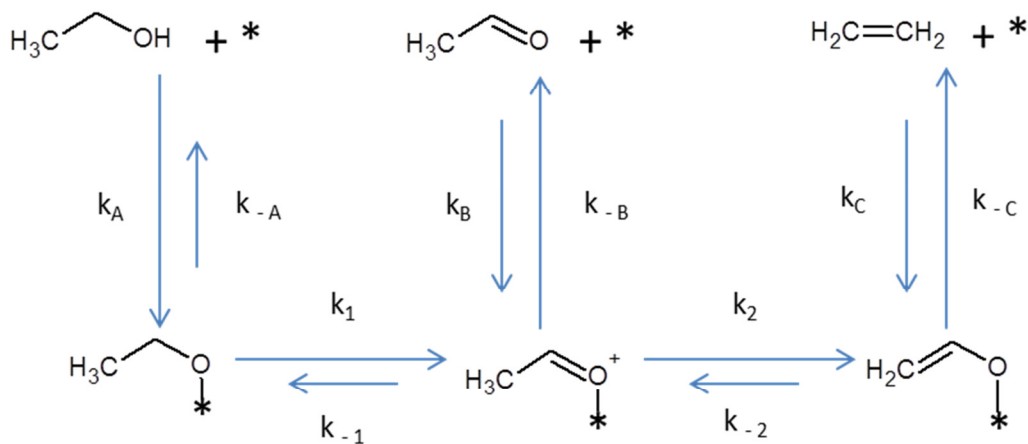
Fig. 2.10. Variation of ethanol conversion and product yield as a function of contact time on $\text{Ni}_2\text{P}/\text{SiO}_2$. The curves are fits from a simulation model discussed in the text.

Reaction temperature and contact time play important roles in the decomposition of ethanol, and their effect on the steady-state reactivity of HZSM-5 and $\text{Ni}_2\text{P}/\text{SiO}_2$ were examined. To summarize, on HZSM-5, the main product was ethylene with small amounts of acetaldehyde and butylenes. Butylenes formed at long contact time and could be attributed to condensation of ethylene and acetaldehyde on strong Brønsted acid sites on the surface of HZSM-5. On $\text{Ni}_2\text{P}/\text{SiO}_2$ the main products of the ethanol reaction were ethylene and acetaldehyde with small amounts of carbon monoxide and trace quantities of methane, without ethane. Acetaldehyde was formed as an intermediate compound.

The results in Fig. 2.10 suggest that there is a consecutive reaction: ethanol \rightarrow acetaldehyde \rightarrow ethylene. This seems odd, because this would entail the oxidation of ethanol before the formation of ethylene, which is unlikely at reductive conditions as used here. It was

reasoned that a more likely possibility was that there existed a common species at the surface that could react to form both acetaldehyde and ethylene in a sequential manner. This led to the following scheme.

Ethanol first adsorbs onto a vacant site to form an ethoxide species. This undergoes dehydrogenation through an alpha-H abstraction from the carbon proximal to the oxygen to form adsorbed acetaldehyde. The adsorbed acetaldehyde can desorb or can react further through an enolization reaction involving a beta-H abstraction from the carbon distal to the oxygen. This can then undergo hydrogenolysis with adsorbed hydrogen on active sites to form ethylene and an adsorbed OH group (not shown).



Scheme 2.1. "Rake" mechanism for ethanol reaction

The catalytic reaction network was simulated based on the disappearance rate of ethanol and the formation rate of acetylene and ethylene. Ethanol, acetylene, and ethylene were noted as A, B, and C respectively and the corresponding adsorbed ethoxy, acetaldehyde, and vinyl alcohol are denoted as A*, B* and C*.

The kinetic rate law equations are the following:

$$1/ \frac{V}{S} \frac{d[A]}{d\tau} = -k_A[A][*] + k_{-A}[A^*]$$

$$2/ \frac{V}{S} \frac{d[B]}{d\tau} = -k_B[B][*] + k_{-B}[B^*]$$

$$3/ \frac{V}{S} \frac{d[C]}{d\tau} = -k_C[C][*] + k_{-C}[C^*]$$

The rate of consumption of A, $-r_A = \frac{V}{S} \frac{d[A]}{d\tau}$ has units of $\text{mol m}^{-2}\text{s}^{-1}$, in which V (m^3) is the bed volume and S (m^2) is the catalyst surface area. This rate is generally expressed as $-r_A = [L]kf(Y)$ where [L] (mol m^{-2}) is the total concentration of sites, k is a rate constant, and f(Y) is a dimensionless function of concentrations.

The bed volume is given by $V = w/\rho_A$, where ρ_A (0.3 g cm^{-3}) is the apparent density. The total surface area of Ni_2P (m^2) given by $S = awf$, where a ($42 \text{ m}^2\text{g}^{-1}$) is the Ni_2P effective surface area, obtained from the equation $a = \frac{6}{\rho D_C}$, w (0.900 g) is the weight of catalyst, f (0.079) is the fractional weight loading of the Ni_2P , ρ (7.09 g cm^{-3}) is the true density, and D_C (20 nm) is the average crystallite size. Finally, τ is the contact time calculated from the volume of the catalyst bed divided by the volumetric flow rate $\frac{V}{v}$. Simplification gives $\frac{V}{S} = \frac{\rho D_C}{6\rho_A f}$. The concentrations of the intermediates as well as the vacant active sites were obtained by solving the following set of equations, assuming that at steady state, the net rate of the formation of the intermediates is zero.

$$4/ \frac{d[A^*]}{d\tau} = k_A[A][*] - (k_{-A} + k_1)[A^*] + k_{-1}[B^*] = 0$$

$$5/ \frac{d[B^*]}{d\tau} = k_B[B][*] + k_1[A^*] - (k_{-B} + k_{-1} + k_2)[B^*] + k_{-2}[C^*] = 0$$

$$6/ \frac{d[C^*]}{d\tau} = k_2[B^*] - (k_{-C} + k_{-2})[C^*] + k_C[C][*] = 0$$

Use was made of an active site balance, where $[L]$ is the total concentration of active sites:

$$7/ [L] = [*] + [A^*] + [B^*] + [C^*]$$

This kind of scheme is known in the literature as a “rake” mechanism because the adsorption and desorption steps when written out as in Scheme 1 resemble the prongs of the device used to gather leaves. The rake mechanism was first described by Cormerais et al. [73] and has been suggested to apply to many types of reactions [74, 75], but in the early days of its introduction 30 years ago the solution of the equations was not readily possible. Even to this day many kinetic studies still use simple first-order analysis of networks that ignore the existence of the adsorption steps. In this case the equations were solved numerically using Polymath[®] software (Table 2.7) to obtain plots of acetaldehyde and ethylene yields and conversion versus time.

Table 2.7. Rate constants used in the simulation

Temperature K	k_A $\text{cm}^3 \text{mol}^{-1} \text{s}^{-1}$	k_{-A} s^{-1}	k_B $\text{cm}^3 \text{mol}^{-1} \text{s}^{-1}$	k_{-B} s^{-1}	k_C $\text{cm}^3 \text{mol}^{-1} \text{s}^{-1}$	k_{-C} s^{-1}	k_1 s^{-1}	k_{-1} s^{-1}	k_2 s^{-1}	k_{-2} s^{-1}
473	2.80×10^7	8.5	3.5×10^7	6.75	2.75×10^7	2.25	9.0	4.5	3.75	3.0
498	3.5×10^7	9.0	4.0×10^7	12.0	3.25×10^7	30.0	17.0	5.0	5.5	3.5

As can be seen by the curves shown in Figs. 2.10a and 2.10b the simulation results are in good agreement with the experimental points, even though the behavior of the species is different. At 473 K the acetaldehyde yield grows together with that of ethylene, while at 498 K there is a clear maximum in the acetaldehyde yield. The rate constants have smaller values at lower temperature as expected. The closeness of the fits indicates that the proposed mechanism describes the physical situation accurately.

In order to further check the reasonableness of the mechanism measurements of adsorbed surface intermediates were undertaken. Data were taken at different temperatures with ethanol adsorbed using He as carrier (Fig. 2.11).

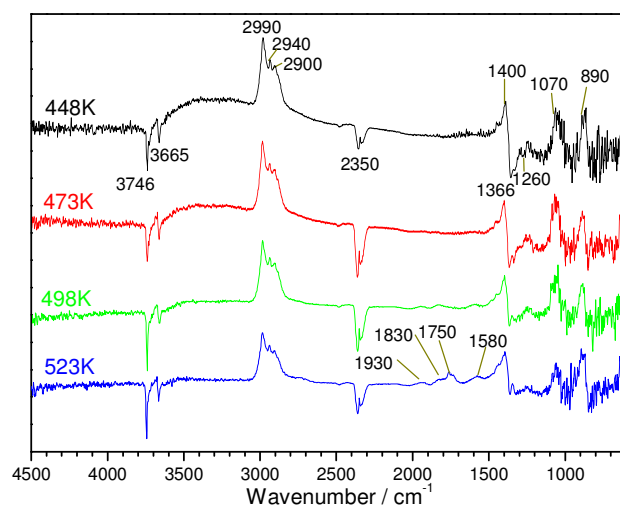


Fig. 2.11. EtOH FTIR over Ni₂P/SiO₂ with 0.15% EtOH in He flow

Table 2.8 summarizes the assignments in the spectra. At high wavenumber two sharp negative bands at 3746 and 3665 cm^{-1} are due SiO-H and PO-H stretching vibrations and appear negative because the hydroxyls are being consumed [55]. At 2990, 2940, and 2900 cm^{-1} a cluster of peaks appear which are due to C-H stretching vibrations for methyl and methylene groups.

Next in the center of the spectrum appear bands at 2365, 2330 due to gas-phase CO₂ interference. For the highest temperature data weak broad bands are present at 1930 and 1830 cm⁻¹, which are attributed to combination bands. A small feature at 1750 cm⁻¹ is due to adsorbed aldehyde CHO. At 1580 cm⁻¹ a small peak is observed which grows with temperature. This position is characteristic of a C=C double bond. An oddly shaped feature at 1400 cm⁻¹ followed by a negative peak at 1366 cm⁻¹ is due to background subtraction. A feature at 1260 cm⁻¹ corresponds to a CH₂ wag. Peaks at 1070 and 890 cm⁻¹ are assigned to the SiO₂ support. Peaks at lower wavenumber are obscured by interference from the silica.

Overall, in He atmosphere, the diminution of OH bands and the growth of C-H stretching vibrations are consistent with the formation of ethoxide species bound to Si and P functionalities. There is also evidence for an adsorbed acetaldehyde species with a band at 1750 cm⁻¹ and the formation of an ethylene or vinyl alcohol species contributing to the C=C signal at 1580 cm⁻¹.

In order to obtain more information on the behavior of the adsorbed species, a transient experiment was carried out. The objective was to simulate the contact time measurements described in Fig. 2.10b. The spectra of ethanol FTIR at 497 K as a function of time are shown in Fig. 2.12.

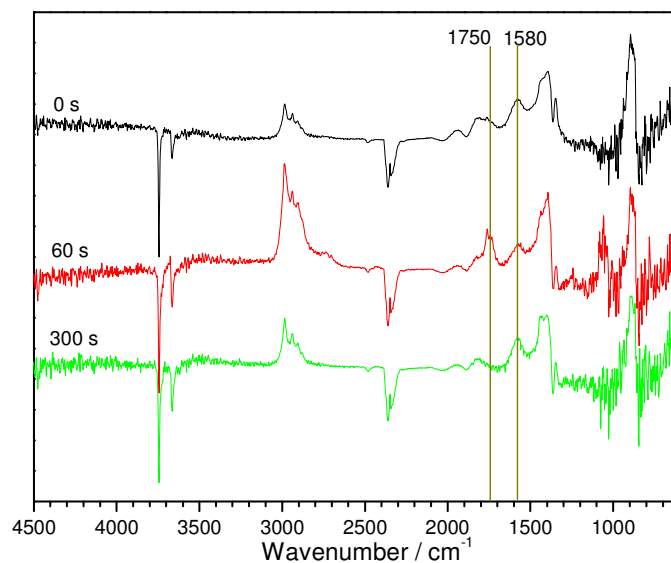


Fig. 2.12. EtOH FTIR over Ni₂P/SiO₂ in He at 497 K

The assignments in Fig. 2.12 are the same as in Fig. 2.11. In Fig. 2.12 vertical lines have been placed at 1750 cm⁻¹ (position for an aldehyde functionality, HC=O) and at 1580 cm⁻¹ (position for an olefin double bond). Examination shows that the peak at 1750 cm⁻¹ increased significantly at first and then disappeared with contact time. At the same time the peak at 1580 cm⁻¹ due to an olefin (C=C) increased with time. These results are consistent with the proposed rake mechanism in which the adsorbed acetaldehyde is an intermediate that is converted to an ethylene precursor on the surface of the catalyst. There was no growth in the band at 2075 cm⁻¹ due to adsorbed carbon monoxide (CO). This further indicates that the adsorbed aldehyde did not decompose to CH₄ and CO but was converted to ethylene.

The picture that emerges from the FTIR measurements is consistent with the reaction scheme presented earlier. Ethanol adsorbs on hydroxyl species on the silica to form ethoxide species. Substantial work [76, 77] indicates that alkoxide species on silica are highly mobile so these can readily move to the Ni₂P surface, which is excellent in hydrogen transfer reactions [37-46]. A

first reaction that occurs is dehydrogenation to form an adsorbed acetaldehyde (growth in band of 1750 cm^{-1}). This may be assisted by basic sites present on the Ni_2P surface as indicated by the CO_2 adsorption measurements (Table 2.3). Subsequently, in He the acetaldehyde undergoes an enolization to vinyl alcohol (growth in band at 1580 cm^{-1}). This set of steps accounts for the main species formed and the main catalytic pathway in the reaction. There is also a side reaction, which is not major in the steady-state, but which proceeds in temperature-programmed reaction, namely the formation of adsorbed CO. This is likely the result of the decomposition of adsorbed acetaldehyde in the presence of H_2 (not He) to a methyl species and CO. The hydrogen is likely adsorbed atomic hydrogen, and the driving force is the formation of methane and strongly bonded CO. Although not a primary path in the steady-state reaction, this pathway accounts for the observation of CH_4 and CO in the ethanol TPD spectra (Fig. 2.7).

Table 2.8. Summary of FTIR assignments

Band (cm^{-1})	Assignment	Species	Reference
3746 (neg)	SiO-H stretch	Si-OH	[55]
3665 (neg)	PO-H stretch	P-OH	[55]
2990, 2940, 2900	C-H stretch	CH_3CH_3 , $\text{CH}_2=\text{CH-OH}$, CH_3CHO , $\text{CH}_3\text{CH}_2\text{OH}$, $\text{CH}_2=\text{CH}_2$,	[78, 79]
2075	C=O	CO	[40, 55]
1930, 1830	Combination		
1750	HC=O	HCHO	[76, 77]
1580	C=C	$\text{CH}_2=\text{CH-OH}$	[78]
1400	OH bend		[76]
1366 (neg)	Background subtraction		
~1310, 1260	CH_2 wag	$\text{CH}_3\text{CH}_2\text{OH}$	[78]
~1160	C-C stretch combination	CH_3CHO , $\text{CH}_3\text{CH}_2\text{OH}$ $\text{CH}_2=\text{CH-OH}$	[78]
~1070	Si-O	SiO_2	
~890	Si-O-Si	SiO_2	

~990	C=C wag C-C stretch	CH ₂ =CH ₂ CH ₃ CH ₃ , CH ₃ CH ₂ OH	[78, 79]
790-830	CH ₃ rock CH ₂ rock	CH ₃ CH ₃ , CH ₃ CHO CH ₂ =CH ₂	[76, 78]
~760	C-H bend	CH ₃ CHO	[78]
~600	CH ₂ =C out of plane	CH ₂ =CH-OH	[77]
~500	C-C-O deform	CH ₃ CHO	[78]
300-400	torsion	CH ₂ =CH-OH	[77]

The reaction of ethanol on HZSM-5 and Ni₂P/SiO₂ provides information on the reaction pathways on a typical acid catalyst and a metal catalyst. The acid catalyst, HZSM-5 carries out simple dehydration to form ethylene. The metal catalyst also forms mainly ethylene, but through a non-direct pathway in which an adsorbed ethoxide species is first dehydrogenated to a surface acetaldehyde species, which undergoes enolization to a vinyl alkoxide and subsequent hydrodeoxygenation. This route is non-direct and occurs because of the strongly metallic hydrogenation/dehydrogenation properties of the Ni₂P. It is important because the pathway may also be involved in the reactions of more complex molecules and for this reason its participation should be considered in the study of their conversion.

2.4. Conclusions

The experiments described in this work lead us to the following conclusions:

1. Comparison between the properties of commercial HZSM-5(Si/Al=15) and synthesized Ni₂P/SiO₂ catalysts showed that HZSM-5 possesses higher surface area and stronger acidic sites than the Ni₂P/SiO₂ catalyst. The Ni₂P/SiO₂ catalyst essentially has more mesopores and moderate acid and basic sites. Infrared spectroscopy of pyridine reveals that acidity of HZSM-5

and Ni₂P/SiO₂ catalysts consist mainly of Brønsted and Lewis acid sites, respectively. In the ethanol temperature programmed desorption process (EtOH-TPD), the Ni₂P/SiO₂ catalyst exhibited a higher selectivity towards dehydrogenation products (acetaldehyde) than HZSM-5.

2. Steady-state reaction results confirm that the Ni₂P/SiO₂ produces both acetaldehyde and ethylene, and contact time studies indicate that acetaldehyde is a primary product and ethylene is a secondary product. The reaction, however, does not consist of an oxidation reaction followed by a reduction reaction, but involves sequential reactions on the surface, namely, a rake mechanism. Analysis of the reaction sequence and simulation of the results give support for this interpretation. Measurements by in situ Fourier transform infrared spectroscopy also give evidence for the presence of the suggested intermediate, adsorbed acetaldehyde, on the surface of the catalyst at reaction conditions. Measurements at increasing contact times show that it increases and then disappears, in agreement with the corresponding reactivity results.

References

1. A. Wawrzetz, B. Peng, A. Hrabar, A. Jentys, A. A. Lemonidou, J. A. Lercher, *J. Catal.*, 269 (2010) 411.
2. J. Zakzeski, P.C.A. Bruijninx, A.L. Jongerius, B.M. Weckhuysen, *Chem. Rev.*, 110 (2010) 3552.
3. O. Casanova, S. Iborra, A. Corma, *J. Catal.*, 275 (2010) 236.
4. T. V. Choudhary, C. B. Phillips, *Appl. Catal. A: Gen.*, 397 (2011) 1.
5. J. J. Bozell, G. R. Petersen, *Green Chem.*, 12 (2010) 539.
6. J. C. Serrano-Ruiz, D. Wang, J. A. Dumesic, *Green Chem.*, 12 (2010) 574.
7. A. Birot, F. Epron, C. Descorme, D. Duprez, *Appl. Catal. B: Environ.*, 79 (2008) 17.
8. J. Rass-Hansen, R. Johansson, M. Moller, C. H. Christensen, *Int. J. Hydrogen Energy* 33 (2008) 4547.
9. E. B. Pereira, P. R. de la Piscina, N. Homs, *Biores. Tech.*, 102 (2011) 3419.
10. Tullo, A. H., *Chem. Eng. News*, 89 (2011) 24.
11. R. L. Guenard, L. C. F. Torres, B. Kim, S. S. Perry, P. Frantz, S. V. Didziulis, *Surf. Sci.*, 515 (2002) 103.
12. P. A. Clayborne, T. C. Nelson, T. C. De Vore, *Appl. Catal. A: Gen.*, 257 (2004) 225.
13. B. M. Nagaraja, A. H. Padmasri, P. Seetharamulu, K. H. P. Reddy, B. D. Raju, K. S. R. Rao, *J. Mol. Catal. A*, 278 (2007) 29.
14. E. A. El-Katatny, S. A. Halawy, M. A. Mohamed, M. I. Zaki, *Appl. Catal. A: Gen.*, (1999) 83.
15. N. R. C. F. Machado, V. Calsavara, N. G. C. Astrath, C. K. Matsuda, A. P. Junior, M. L. Baesso, *Fuel*, 84 (2005) 2064.
16. V. Calsavara, M. L. Baesso, N. R. C. F. Machado, *Fuel*, 87 (2008) 1628.
17. N. Takezawa, C. Hanamaki, Kobayashi H, *J. Catal.*, 38 (1975) 101.
18. Y. Matsumura, K. Hashimoto, S. Yoshida, *J. Catal.*, 117 (1989) 135.
19. I. Takahara, M. Saito, M. Inaba, K. Murata, *Catal. Lett.*, 105 (2005) 249.
20. X. Zhang, R. Wang, X. Yang, F. Zhang, *Microp. Mesop. Mater.*, 116 (2008) 210.
21. J. Schulz, F. Bandermann, *Chem. Eng. Technol.*, 17 (1994) 179.
22. C. B. Phillips, R. Datta, *Ind. Eng. Chem. Res.*, 36 (1997) 4466.
23. J. M. Vohs, M. A. Barteau, *Surf. Sci.*, 211 (1989) 590.
24. F. W. Chang, W. Y. Kuo, K. C. Lee, *Appl. Catal. A: Gen.*, 246 (2003) 253.
25. M. A. Aramendía, V. Borau, C. Jiménez, J. M. Marinas, A. Porras, F. J. Urbano, *J. Catal.*, 161 (1996) 829.
26. Y. Shinohara, T. Nakajima, S. Suzuki, *J. Mol. Struct.*, 460 (1999) 231.
27. M. M. Doheim, H. G. El-Shobaky, *Surf. Sci. A*, 204 (2002) 169.
28. F. S. Ramos, A. M. Duarte de farias, L. E. P. Borges, J. L. Monteiro, M. A. Fraga, E. F. Sousa-Aguiar, L. G. Appel, *Catal. Today*, 101 (2005) 39.
29. M. A. Aramendía, V. Boráu, C. Jiménez, J. M. Marinas, A. Porras, F. J. Urbano, *React. Kinet. Catal. Lett.*, 65 (1998) 25.
30. M. A. Aramendía, V. Boráu, I. M. García, C. Jiménez, A. Marinas, J. M. Marinas, F. J. Urbano, A. Porras, *Appl. Catal. A: Gen.*, 184 (1999) 115.
31. H. Y. Zhao, D. Li, P. Bui, S. T. Oyama, *Appl. Catal. A: Gen.*, 391 (2011) 305.
32. Y. Shu, Y. -K Lee, S. T. Oyama, *J. Catal.*, 236 (2005) 112.

33. T. Kawai, K. K. Bamdo, Y. -K. Lee, S. T. Oyama, W. -J. Chun, K. Asakura, *J. Catal.*, 241 (2006) 20.
34. X. Wang, P. Clark, S. T. Oyama, *J. Catal.*, 208 (2002) 321.
35. S. T. Oyama, X. Wang, Y. -K. Lee, K. Bando, F. G. Requejo, *J. Catal.*, 210 (2002) 207.
36. S. T. Oyama, T. Gott, H. Zhao, Y. -K. Lee, *Catal. Today*, 143 (2009) 94.
37. Oyama, S. T., *J. Catal.*, 216 (2003) 343.
38. S. T. Oyama, X. Wang, F. Requejo, T. Sato, Y. Yoshimura, *J. Catal.*, 209 (2002) 1.
39. S. T. Oyama, X. Wang, Y. -K. Lee, W. -J. Chun, *J. Catal.*, 221 (2004) 263.
40. S. J. Sawhill, K. A. Layman, D. R. Van Wyk, M. H. Engelhard, C. Wang, M. E. Bussell, *J. Catal.*, 231 (2005) 300.
41. P.A. Clark, X. Wang, P. Deck, *J. Catal.*, 210 (2002) 116.
42. P. A. Clark, S. T. Oyama, *J. Catal.*, 218 (2003) 78.
43. S.T. Oyama, Y.-K. Lee, *J. Catal.*, 258 (2008) 393.
44. M. Guisnet, P. Magenoux, *Stud. Surf. Sci. Catal.*, 88 (1994) 53.
45. A. G. Gayubo, A. Alonso, B. Valle, A. T. Aguayo, J. Bilbao, *Appl. Catal. B: Environ.*, 97 (2010) 299.
46. P. Berteau, B. Delmon, *Appl. Catal.*, 70 (1991) 307.
47. W. Wang, S. P. Wang, X. B. Ma, J. L. Gong, *Catal. Today*, 148 (2009) 323.
48. S. R. Jagtap, Y. P. Patil, *Appl. Catal. A: Gen.*, 341 (2008) 133.
49. A. S. Ndou, N. Plint, N. J. Coville, *Appl. Catal. A: Gen.*, 251 (2003) 337.
50. P. Berteau, B. Delmon, *Catal. Today*, 5 (1989) 121.
51. J. D. Bi, X. W. Guo, M. Liu, X. S. Wang, *Catal. Today*, 149 (2010) 143.
52. J. G. Post, H. G. V. Hoof, *Zeolites*, 4 (1984) 9.
53. D. J. Parrillo, C. Lee, R. J. Gorte, *Appl. Catal. A: Gen.*, 110 (1994) 67.
54. H. G. Karge, V. Dondur, J. Weitkamp, *J. Phys. Chem.*, 95 (1991) 283.
55. Y. -K. Lee, S. T. Oyama, *J. Catal.*, 239 (2006) 376.
56. T. Gott, S. T. Oyama, *J. Catal.*, 263 (2009) 359.
57. S. T. Oyama, T. Gott, K. Asakura, S. Takakusagi, K. Miyazaki, Y. Koike, K. K. Bando, *J. Catal.*, 268 (2009) 209.
58. K. M. A. El-Salaam, E. A. Hassan, *Surf. Technol.*, 16 (1982) 121.
59. F. F. Roca, L. D. Mourgues, Y. Trambouze, *J. Catal.*, 14 (1969) 107.
60. S. Golay, L. Kiwi-Minsker, R. Doepper, A. Renken, *Chem. Eng. Sci.*, 54 (1999) 3593.
61. R. L. Mao, T. S. Le, M. Fairbairn, A. Muntasar, S. Xiao, G. Denes, *Appl. Catal. A: Gen.*, 185 (1999) 41.
62. M. Lenarda, M. D. Ros, M. Casagrande, L. Storaro, R. Ganzerla, *Inorg. Chim. Acta.*, 349 (2003) 195.
63. Emeis, C. A., *J. Catal.*, 141 (1993) 347.
64. G. A. M. Hussein, N. Sheppard, *J. Chem. Soc., Faraday Trans.*, 87 (1991) 2661.
65. M. Dömöka, M. Tótha, J. Raskób, A. Erdöhelyi, *Appl. Catal. B: Environ.*, 69 (2007) 262.
66. J. Franckaerts, G. F. Froment, *Chem. Eng. Sci.*, 19 (1964) 807.
67. T. Yamazaki, N. Kikuchi, M. Katoh, T. Hirose, H. Saito, T. Yoshikawa, M. Wada, *Appl. Catal. B: Environ.*, 99 (2010) 81.
68. A. Gazsi, A. Koos, T. Bansagi, F. Solymosi, *Catal. Today*, 160 (2011) 70.
69. Solymosi, A. P. Farkas and F., *Surf. Sci.*, 601 (2007) 193.
70. J. Gorte, R., *J. Catal.*, 75 (1982) 164.
71. E. E. Ibok, D. F. Ollis, *J. Catal.*, 66 (1980) 391.

72. B. M. Abu-Zied ,A. M. El-Awad, J. Mol. Catal. A, 176 (2001) 227.
73. F.X. Cormerais,G. Perot,F. Chevalier,M. Guisnet, J. Chem. Res., S (1980) 362.
74. S. Lars, T. Andersson, J. Catal., 98 (1986) 138.
75. Stöcker, M., Mesop. Micropor. Mat. , 29 (1999) 3.
76. M. Seman,J. N. Kondo,K. Domen,R. Radhakrishnan,S. T. Oyama, J. Phys. Chem. B, 106 (2002) 12965.
77. M. Seman,J. N. Kondo,K. Domen,R. Radhakrishnan,S. T. Oyama, Chem. Lett., 11 (2002) 1082.
78. Shimanouchi, T. *Molecular vibrational frequencies*. NIST Chemistry WebBook, NIST Standard Reference Database Number 69 [cited 2011 June 23].
79. M. Hawkins ,L. Andrews, J. Am. Chem. Soc. , 105 (1983) 2523.

Chapter 3

Synthesis of Transition Metal Phosphides via Phosphate and Phosphite Method and their Activity in the Hydrodeoxygenation of 2-Methyltetrahydrofuran

P. Bui, J. A. Cecilia, S. T. Oyama, A. Takagaki, A. Infantes-Molina, H. Zhao, D. Li, E.

Rodríguez-Castellón, A. J. López

Journal of Catalysis, Volume 294, October 2012, Pages 184-198

Used with permission of the Elsevier, 2013

3.1. Introduction

The need to meet stringent environmental regulations and the depletion of fossil fuel reserves have led to interest in biomass as a renewable energy source. The utilization of biomass-derived fuels has several advantages over the use of conventional fuels, such as reduction in greenhouse gas emissions, localized production, and favorable economics of utilization [1-4]. One method of biomass conversion is pyrolysis – a thermal decomposition of biomass in the absence of oxygen that yields an energy-rich liquid mixture of oxygenated aromatic and aliphatic compounds called bio-oil [5, 6]. Bio-oil, however, has a high oxygen content (35-50 wt%) with 15-30 wt% of water that results in low heating value, immiscibility with hydrocarbon fuels, high acidity, and chemical and thermal instability compared with hydrocarbon fuels [7, 8]. To upgrade the bio-oil into a usable fuel it is necessary to remove the oxygen [9]. A first objective of this work is to study the deoxygenation of a model compound, 2-methyltetrahydrofuran. This is a

five-atom saturated ring compound and was chosen as a model substrate because previous work has shown that ring compounds are difficult to deoxygenate [10]. Furans are also common products in the thermal degradation of biomass, such as pyrolysis [11]. The presence of the methyl group allows distinguishing between the ring-opening products and hence gives mechanistic information.

Standard catalysts for the elimination of S and N heteroatoms from petroleum feedstocks are sulfided CoMo and NiMo; these may also be used for the removal of O, for example from phenols and furans in biomass-derived liquids [12-14], however, the results have been modest. It is clear that new catalysts are needed. Among new compositions that have been explored in hydrotreating processes, phosphides of transition metals are considered potential substitutes for the CoMo and NiMo sulfided materials [15-17]. In the past decade a plethora of works has shown that MoP [18, 19], WP [18, 20], CoP [21, 22], Fe₂P [22], and Ni₂P [22-25] are highly active for hydrodesulfurization and hydrodenitrogenation of petroleum feedstocks. Recently their good hydrogen transfer properties have been applied to the hydrodeoxygenation (HDO) of biomass-derived feedstocks [26-28].

The most common method for the preparation of phosphides is temperature-programmed reduction (TPR), a simple process that can be carried out at relatively moderate temperatures with supported or unsupported precursors [15]. With regard to the use of supports, previous research has shown that less acidic supports such as silica or hexagonal mesoporous silica (SBA-15 [29] and MCM-41 [24]) favor the formation of metal phosphides due to the low interaction between the support and the precursor, usually a metal phosphate. Recently, precursors other than phosphates have also been investigated, for example, phosphosulfides [30]. A substantial recent development is the use of metal phosphites (e.g. Ni(HPO₃H)₂) instead of phosphates (e.g.

NiHPO₄) as precursors [24]. The former have phosphorous in a lower oxidation state which make it potentially reducible at a lower temperature; for example, using a batch reduction method, an active Ni₂P was formed at 300 °C compared to 450 °C using the traditional phosphate method [24, 25, 31, 32].

A second objective of this work besides studying the HDO reaction is to compare the traditional phosphate method and the new phosphite method for the preparation of a variety of transition metals. This has not been done before. For this purpose five pairs of metal phosphides (Ni₂P, CoP, FeP, MoP, and WP) supported on silica were chosen. Their activity for HDO of the model compound 2-methyltetrahydrofuran was evaluated and compared. Furthermore, for the most active phosphide compounds a study of reaction pathway was carried out.

3.2. Materials and Experiments

3.2.1. Materials and catalysts

The transition metal phosphides Ni₂P, CoP, WP, MoP, and FeP supported on a high surface area fumed silica support (Cab-osil ® EH5, surface area of 334 m² g⁻¹ and pore volume of 0.6 cm³ g⁻¹) provided by Cabot Corp. were synthesized. Sources of iron, tungsten, and molybdenum were iron(III) nitrate (Fe(NO₃)₃·9H₂O (Aldrich 98+%)), ammonium metatungstate hydrate ((NH₄)₆W₁₂O₃₉·H₂O (Aldrich, 99.99%)), and ammonium heptamolybdate tetrahydrate ((NH₄)₆Mo₇O₂₄·4H₂O (Alfa Aesar, 99.98%)). For the phosphate method, sources of cobalt and nickel were cobalt(II) nitrate (Co(NO₃)₂·6H₂O (Aldrich, 99.99%)) and nickel(II) nitrate (Ni(NO₃)₂·6H₂O (Alfa Aesar, 99.6%)). For the phosphite method, the precursors of cobalt and

nickel were cobalt(II) hydroxide ($\text{Co}(\text{OH})_2$ (Aldrich 95%)) and nickel(II) hydroxide ($\text{Ni}(\text{OH})_2$ (Aldrich, 98+%). The sources of phosphorus were ammonium hydrogen phosphate ($(\text{NH}_4)_2\text{HPO}_4$ (Aldrich 99%)) and phosphorous acid ($\text{H}_2\text{PO}_3\text{H}$ (Aldrich 99%)). The 5% Pd/ Al_2O_3 commercial catalyst was provided by BASF Catalysts, Inc. The model compound used in reactivity study was 2-methyltetrahydrofuran (Aldrich 99.95%). The gases employed were H_2 (Airgas, Grade 5), He (Airgas, Grade 5), CO (Linde Research Grade, 99.97%), 0.5% O_2/He (Airgas, UHP Grade), O_2 (Airgas, UHP Grade), N_2 (Airgas, Grade 5).

The synthesis of the supported phosphide catalysts was carried out by a standard phosphate method and a more recently developed phosphite method. A silica support (Cab-osil ® EH5) was employed in both methods. The support was dried at 120 °C for 6 h and calcined at 500 °C for 4 h prior to use. Both synthetic routes required the preparation of a precursor in three steps. First, a mixed solution of metal and phosphorus compounds was made by adding an appropriate amount of a desired metal salt into a phosphorus solution; the phosphorous solution was made by mixing ammonium phosphate (phosphate method) or phosphorous acid (phosphite method) into distilled water. Second, the mixed solution was used to impregnate the silica support to the incipient wetness point (about 2 cm³ of solution per gram of support). Finally, the obtained phosphate precursor mixture was dried at 120 °C for 6 h and calcined at 500 °C for 6 h; whereas the phosphite precursor mixture was only dried in air at 80 °C overnight without any calcination. Then all samples were pelletized and sieved to 16/20 mesh size. In the same manner, the precursors from both methods were reduced to phosphides by a temperature-programmed reduction (TPR) at a heating rate of 2 °C min⁻¹ in flowing H_2 [1000 cm³ (NTP) min⁻¹ g⁻¹] and kept at the reduction temperature for 2 h. The reduction temperatures were determined in separate temperature reduction experiments as the temperature at which water production peaked

(details are described in the characterization section). The resulting phosphides were cooled to room temperature in He [$100 \text{ cm}^3 \text{ (NTP) min}^{-1}$], followed by passivation in a He stream containing 0.5% O_2 for 2 h.

Table 3.1 summarizes the loadings of metal and phosphorous used in the preparation of the catalysts. For all metals Fe, Co, Ni, Mo, and W equal moles of the element per gram of support (1.16 mmol/g support) were used.

Table 3.1. Materials and amounts used in the preparation of phosphides supported on silica

Sample	Conventional (Phosphate) Method (A)			New (Phosphite) Method (I)			
	Metal source (mmol/g support)		Phosphorous (NH_4) ₂ HPO ₄ (mmol/g support)	Metal (mmol/g support)		Phosphorous H ₃ PO ₃ (mmol/g support)	Metal phosphide (wt%)
Ni ₂ P	Ni(NO ₃) ₂ ·6H ₂ O	1.16	2.31	Ni(OH) ₂	1.16	2.31	7.9
CoP	Co(NO ₃) ₂ ·6H ₂ O	1.16	2.31	Co(OH) ₂	1.16	2.31	9.4
WP	(NH ₄) ₆ W ₁₂ O ₃₉ ·H ₂ O	1.16	1.16	(NH ₄) ₆ W ₁₂ O ₃₉ ·H ₂ O	1.16	2.31	19.9
MoP	(NH ₄) ₆ Mo ₇ O ₂₄ ·4H ₂ O	1.16	1.16	(NH ₄) ₆ Mo ₇ O ₂₄ ·4H ₂ O	1.16	2.31	12.8
FeP	Fe(NO ₃) ₃ ·9H ₂ O	1.16	2.31	Fe(NO ₃) ₃ ·9H ₂ O	1.16	2.31	9.1

The synthesis of the materials was carried out by temperature-programmed reduction and monitored by mass spectrometry. The samples were characterized with carbon monoxide (CO) chemisorption, Brunauer Emmett Teller (BET) surface area measurements, X-ray diffraction (XRD), and X-ray photoelectron spectroscopy (XPS).

The temperature-programmed reduction was carried out in a U-shaped quartz reactor placed in a furnace controlled by a temperature programmer (Omega Model CN 2000). The temperature was measured with a local type K thermocouple placed near the center of the reactor bed. An amount of 0.3 g of precursor was reduced in H₂ [$300 \text{ cm}^3 \text{ (NTP) min}^{-1}$] at a heating rate of 2 °C min⁻¹ from room temperature to 800 °C. A portion of the exhaust gas flow was

introduced through a leak valve into a mass spectrometer (Ametek/Dycor MA100), which monitored masses 2(H₂), 4(He), 18(H₂O), and 34(PH₃) during the experiment. The reduction profiles revealed reduction stages in the transformation of the precursors to the phosphides.

Irreversible CO uptake measurements were used to titrate the surface metal atoms and to estimate the number of active sites on the catalysts. Uptakes were obtained after 0.3 g of passivated samples were re-reduced in H₂ at 450 °C for 2 h and cooled to room temperature in He. Pulses of known amounts of CO carried by He at 30 μmol s⁻¹ were injected into the sample. An on-line mass spectrometer monitored the signal of mass 28 (CO) throughout the experiment. CO uptake was calculated from the decrease in peak areas caused by adsorption of CO onto the catalysts surface. Measurements from CO chemisorption allowed estimation of the dispersion of metal sites using the following equation:

$$\text{Dispersion (\%)} = \frac{\text{CO uptake } \left(\frac{\mu\text{mol}}{\text{g}}\right)}{\text{Loading } \left(\frac{1.16 \mu\text{mol}}{\text{g}}\right)} 100\%$$

The BET surface areas of the catalysts were obtained from their nitrogen adsorption isotherms carried out in a volumetric adsorption unit (Micromeritics, ASAP 2010). The catalysts were degassed at 120 °C in vacuum for 6 h prior to the measurements. Adsorption at liquid nitrogen temperature was performed using a value of 0.162 nm² as the cross-sectional area of the N₂ molecule.

XRD measurements were made with a PANalytical X'pert Pro powder diffractometer operated at 45 kV and 40 mA, using Cu Kα monochromatized radiation (λ = 0.154178 nm). Crystallite size was calculated using the Scherrer equation $D_c = \frac{K\lambda}{\beta\cos(\theta)}$ in which K is the shape

factor with a value of 0.9, λ is the X-ray wavelength, β is the line broadening at half the maximum intensity in radians (accounting for instrumental broadening of 0.1°), and θ is the Bragg angle.

X-ray photoelectron spectra were collected using a physical electronics PHI 5700 spectrometer with non-monochromatic Al K α radiation (300 W, 15 kV, and 1486.6 eV) with a multi-channel detector. Spectra of pelletized samples were recorded in the constant pass energy mode at 29.35 eV, using a 720 μ m diameter analysis area. Charge referencing was measured against adventitious carbon (C 1s at 284.8 eV). A PHI ACCESS ESCA – V6.0 F software package was used for acquisition and data analysis. A Shirley-type background was subtracted from the signals. Recorded spectra were always fitted using Gaussian – Lorentzian curves in order to determine the binding energies of different element core levels more accurately. Reduced and spent catalysts were stored in sealed vials with an inert solvent. Prior to XPS measurement in the analysis chamber, the solvent was evaporated off the catalyst sample in a dry box under a N₂ flow.

3.2.2. Reactivity studies

Hydrodeoxygenation of 2-methyltetrahydrofuran (2-MTHF) was carried out in a packed bed reactor as a function of temperature at atmospheric pressure. Quantities of catalysts loaded into the reactor were equivalent to 30 μ mol of active-surface metal atoms (from CO uptake measurements). The reactivity tests were conducted as a function of temperature at a space velocity (GHSV) of 8000 h⁻¹ corresponding to a contact time of 6.7 s. The space velocity and contact time were respectively defined by the following equations:

$GHSV = \frac{\text{Feed volume flow rate}}{\text{Volume of the catalyst bed}}$ in which feed volume flow rate is 12000 [cm³ (NTP) h⁻¹]

and volume of the catalyst bed is 1.5 cm³.

$\text{Contact time} = \frac{\text{Quantity of active sites of catalyst loaded}}{\text{Reactant molar flow rate}}$

The catalysts were pretreated at the same conditions as for the chemisorption measurements followed by cooling to 350 °C. Then, a flow of H₂ [200 cm³ (NTP) min⁻¹] through a saturator containing 2-MTHF was introduced to the reactor. The saturator was kept at 0 °C and contained 95 volume % of 2-MTHF and 5% of heptane as an internal standard. Antoine equation was used to obtain the vapour pressure of the components of the liquid mixture and Raoult's law was used to give the gas-phase concentration in the feed. Antoine equation is as follows: $\log P^{\text{sat}} = A - \frac{B}{T+C}$ where P^{sat} is the vapour pressure in mmHg, T is the bubbler temperature (0 °C) and the coefficients A, B, and C are 7.13891, 1339.48, and 234.353 respectively for 2-MTHF and 7.04605, 1341.89, and 223.733 respectively for heptane [33]. After unit conversion, the saturated vapour pressures of 2-MTHF and heptane were 0.035 atm and 0.015 atm respectively. Using Raoult's law, the vapour pressure of the liquid mixture was expressed as $P^{\text{vap}} = P_{2\text{-MTHF}}^{\text{sat}}x_{2\text{-MTHF}} + P_{\text{heptane}}^{\text{sat}}x_{\text{heptane}}$ where x is molar fraction of each component in the liquid. The vapour pressure of the liquid has a value of 0.034 atm, thus, at atmospheric pressure, the gas-phase concentration of 2-MTHF in the feed stream is 3.2 molar %. The catalysts were stabilized for 12 h after 2-MTHF was first introduced. Temperature was varied as follows: 350 °C → 300 °C → 250 °C → 275 °C → 325 °C → 350 °C, with the reaction held at each temperature for 4 h. The use of a high temperature at the onset and the cycling

down to a low temperature and back up minimizes potential changes in the catalyst and can indicate if deactivation has occurred. Starting at a low temperature and simply going up can change the catalyst and give unreliable data. The catalysts showed good stability over the 48 h of reactivity testing. The reaction products were monitored by an online gas chromatograph (SRI 8610B) equipped with an HP-1 100m x 0.25mm capillary column and a flame ionization detector. The reactants and products were identified by comparing their retention times with those of commercial standards and confirmed by gas chromatography – mass spectrometry (GC-MS) (Hewlett – Packard, 5890-5927A). Results from the reactivity as a function of temperature were used to calculate turnover frequencies.

Contact time studies for nickel phosphide and tungsten phosphide supported on silica were conducted in a similar manner. An amount of catalyst corresponding to 5 μmol active sites was used for each test. The experiment was carried out at a constant temperature (300 °C) while the feed flow rate was varied so as to achieve contact times in the range of 0.3 - 7s. Contact time studies provide information on intermediate species and reaction steps involved in the deoxygenation of 2-methyltetrahydrofuran on the phosphides.

3.3. Results and Discussion

3.3.1. Temperature-programmed reduction

Temperature-programmed reduction (TPR) experiments were carried out to understand the phenomena involved in the reduction process and to determine the optimum reduction conditions for large scale catalyst preparation. Fig. 3.1 shows water ($m/z = 18$) and phosphine ($m/z = 34$)

evolution during the reduction of the precursors. Throughout this paper, catalysts prepared by the phosphate method are denoted with (A) and those prepared by the phosphite method are denoted with (I).

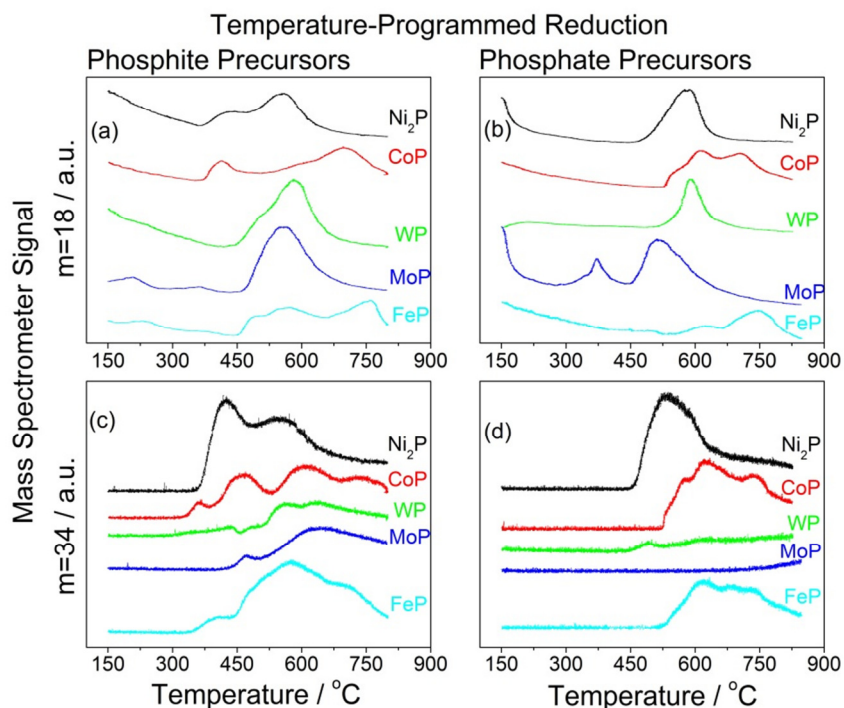


Fig. 3.1. Temperature-programmed reduction of transition metal phosphide catalysts supported on silica; heating rate of 2°C/min, H₂ flow rate of 100ccm/g of catalyst. a) Mass 18 signal, phosphite precursors, b) Mass 18 signal, phosphate precursors, c) Mass 34 (PH₃) signal, phosphite precursors, d) Mass 34 (PH₃) signal, phosphate precursors.

The details of the synthesis of transition metal phosphides by H₂-TPR depend on the metal. In all cases it is likely that the partly or completely reduced transition metal catalyzes the reduction of the phosphite or phosphate components to form phosphine (PH₃) that itself reacts with the reduced metal to form the transition metal phosphide [34]. The ratio of phosphorus-to-metal (P:M) clearly affects the phosphine evolution of the catalysts reduction. Supported

tungsten and molybdenum phosphate precursors did not give off phosphine in the reduction because their stoichiometric P:M ratio (1:1) dictated that all phosphorous would be consumed. On the other hand, phosphine was released when the use of M:P ratio was 1:2. A P:M ratio equal to 2 is required in the phosphite method in order to form $\text{Ni}(\text{HPO}_3\text{H})_2$ and $\text{Co}(\text{HPO}_3\text{H})_2$ precursors. The same ratio was used for iron, tungsten and molybdenum precursors for comparative purposes. TPR profiles will be discussed over iron group phosphides (Ni_2P , CoP , and FeP) and then group 6 metal phosphides (MoP and WP).

The reduction profile for FeP/SiO_2 using the phosphite precursor (Fig. 3.1a) shows a broad signal composed of three unresolved water peaks (480, 570, 760 °C), while that using phosphate precursor (Fig. 3.1b) also has three overlapping water peaks but at higher temperature (600, 700, 770 °C). The temperatures of the latter are higher than those reported earlier (650 °C) for the reduction of $\text{Fe}_2\text{PO}_4/\text{SiO}_2$ likely due to the use of a heating rate (2 °C min^{-1}) double the previous (1 °C min^{-1}) [22]. In the earlier study the multiple peaks were ascribed to the presence of iron oxide intermixed with the phosphate in the precursor, and this is likely the case here. The formation of PH_3 occurred mostly simultaneously with the reduction of the phosphite (Fig. 3.1c) and phosphate (Fig. 3.1d), although by itself phosphate is not reducible except at high temperature [35]. This indicates that reduced Fe is catalyzing its reduction. Overall, the reduction of the phosphite precursor begins at a lower temperature, but finishes at approximately the same temperature.

The reduction profile for CoP using the phosphite precursor (Fig. 3.1a) shows an initial water peak (410 °C) followed by a slowly-developing broad feature with a high temperature maximum (700 °C), while that using the phosphate precursor lacks the initial peak and consists of a broad twin-peaked signal (610, 700 °C). In previous work with the phosphate precursor a

narrower cluster of peaks (560 °C) was observed [22]. The production of PH₃ during the reduction of the phosphite precursor (Fig. 3.1c) shows four peaks that do not correspond clearly to stages in the overall reduction trace. In contrast, the formation of PH₃ during the reduction of the phosphate precursor (Fig. 3.1d) follows the reduction process, indicating that metal reduction and PH₃ formation occurred simultaneously. In summary for CoP the reduction of the phosphite occurs at similar temperatures to the phosphate.

The reduction profile for Ni₂P using the phosphite precursor (Fig. 3.1a) shows an initial small water peak (420 °C) followed by a larger peak at a moderate temperature (560 °C), while that using the phosphate precursor shows a single peak (590 °C). Results from the phosphite method match well with previous work [23]. Previous work with the phosphate method also showed a single reduction peak but at a lower temperature (530 °C) – an outcome of the slower heating rate (1 °C min⁻¹) [17]. Studies of calcined precursors with different Ni/P ratios supported on different types of silica clearly showed a trend that the reduction temperature of Ni increases with increasing P content [17, 34]. This is consistent with the results obtained here since the sample using the phosphate method has excess phosphorous (P:Ni = 2). Another study that used in situ X-ray diffraction to follow the reduction of a phosphorous-poor Ni composition showed that Ni was reduced at low temperatures (400 °C), and subsequent phosphidation did not occur until moderate temperatures (550 °C) [36]. The moderate temperature is similar to the results here. The PH₃ formation during reduction of the phosphate (Fig. 3.1d) follows the overall reduction process, with attenuation at higher temperature again due to the formation of the phosphide. In general, Ni₂P/SiO₂ by the phosphite method was formed at a slightly lower temperature than the catalyst from the phosphate method.

The reduction profile for MoP/SiO₂ using the phosphite precursor (Fig. 3.1a) shows a small water peak at 350 °C followed by a large peak at 560 °C. On the other hand, for the phosphate precursor (Fig. 3.1b), the reduction of Mo occurred through an intermediate stage (375 °C) followed by simultaneous reduction and phosphidation (520 °C), in agreement with a previous study [18]. Previous research has established that the lower temperature water peak was due to the reduction of MoO₃ to MoO₂ and that the higher temperature peak was due to the further reduction of both molybdenum and phosphorus to form MoP [37]. For the phosphite method, the first small PH₃ peak at 450 °C is at the start of a large water peak, followed by a broad figure at 625 °C (Fig. 3.1c). The peaks do not correspond clearly to stages of MoO₃ and MoO₂ reduction indicating that metal phosphidation and PH₃ formation take place simultaneously. The MoP/SiO₂ phosphate precursor does not have excess phosphorus and no phosphine is detected during the reduction, indicating that all phosphine produced was consumed for phosphidation.

Finally, the reduction profile for WP using the phosphite precursor (Fig. 3.1a) exhibits a major water peak at 580 °C with a small shoulder at 500 °C while using the phosphate precursor (Fig. 3.1b) the profile shows a single peak at a slightly higher temperature (600 °C). Though there were no previous studies of the preparation of WP/SiO₂ by the phosphite method, the results for the phosphate method agree well with the previous work [20]. The TPR profile of WP does not indicate reduction of WO₃ into WO₂ at similar temperatures to those found in MoP synthesis. At higher temperatures (~ 600 °C) the tungsten precursor was reduced to W⁰ which then reacted with phosphine to form WP [20]. Phosphine (Fig. 3.1c, 1d) displays a PH₃ evolution peak from the phosphite method but very little PH₃ is detected from the phosphate method. The phosphorous to metal (P:M) ratio is the key to explain this result. The WP/SiO₂ (I) precursor has a 2:1 P:M ratio and thus the excess phosphorus is released during the reduction,

while the WP/SiO₂ (A) precursor has a 1:1 P:M ratio and there is no excess phosphorus to release. This may also imply that all the phosphine produced was immediately consumed to make tungsten phosphide.

In conclusion, cobalt and iron phosphides from either type of precursor were formed at similar temperatures – CoP at 700 °C and FeP at 760 °C. The phosphite precursor of nickel phosphide was reduced at a slightly lower temperature (560 °C) than the phosphate precursor (590 °C). Similarly, WP (I) was formed at 580 °C and WP (A) at 600 °C. Molybdenum phosphide did not follow the trend; MoP (I) was formed at 560 °C, whereas MoP (A) was produced at a lower temperature (520 °C). The highest temperature at which water was detected by the mass spectrometer plus twenty degree was chosen to be the reduction temperature in the synthesis of larger quantities of catalysts. The materials were held at these temperatures for 2 h to ensure complete reduction.

3.3.2. BET surface area

Table 3.2 summarizes characterization results on BET surface areas, CO chemisorption, crystallite size, and dispersion (D) for all catalysts. The BET surface areas of the phosphides range from 149 to 217 m² g⁻¹. As reported before, supports with a low acidity such as silica or hexagonal mesoporous silica favour the synthesis of transition metal phosphides due to the weak interaction between support and precursor [21, 23]. It is likely that part of the pores were partially blocked by the presence of the phosphides and the phosphorus excess on the surface, causing a reduction in surface area. Nevertheless, all synthesized catalysts show a high surface area, indicating a high dispersion of the active phase on the support.

Table 3.2. Characterization results for the supported phosphide catalysts. (I) – catalysts made by the phosphite method, (A) – catalysts made by the phosphate method

Samples	Reduction temperature (°C)	BET Surface Area (m ² /g)	CO uptake (μmol/g)	Crystallite size (nm)	Dispersion (%)
Ni ₂ P (I)	580	217	137	-	12
Ni ₂ P (A)	610	177	115	15	10
CoP (I)	720	197	138	29	12
CoP (A)	720	158	56	32	5
WP (I)	600	178	37	19	3
WP (A)	620	149	42	-	4
MoP (I)	580	220	111	5	10
MoP (A)	540	174	201	-	17
FeP (I)	780	194	102	22	9
FeP (A)	780	185	15	29	1
Pd/Al ₂ O ₃	380	80	413	4	35

As expected, all catalysts from the phosphite method show higher surface areas than those from the phosphate method. This is because the phosphite method eliminates the high-temperature calcination step, which is used in the phosphate method. Thus, the catalysts prepared by the phosphite method are not subjected to a “double sintering” (from calcination and reduction) that reduces the surface area.

3.3.3. CO chemisorption

The chemisorption of CO provides an estimate of the number of active metal sites on the surface of the catalysts. Infrared studies of CO adsorption on Ni₂P [38] and MoP [39] show that CO adsorption is mostly linear on metal sites; therefore it is reasonable to assume a stoichiometry of one CO molecule per surface metal atom. The measured CO adsorption capacities are presented in Table 3.2.

The CO chemisorption values of the different samples vary over a wide range from 15 to 200 $\mu\text{mol g}^{-1}$. The results of catalysts from the phosphate method are close to those reported previously [26]. The phosphite method shows higher CO uptake than the phosphate method for the iron group transition metal phosphides – $\text{Ni}_2\text{P/SiO}_2$, CoP/SiO_2 , and FeP/SiO_2 . The significantly low value of FeP/SiO_2 from the phosphate method is possibly due to blockage of active metal sites by species that prevents adsorption. The phosphate precursor has phosphorus in the high +5 oxidation state so is not easily reducible except at high temperatures [22, 24]. Iron phosphate itself also requires high reduction temperature to convert to the phosphide [22]. It is likely that excess phosphorus and unreduced phosphate might have remained on the surface of the catalyst even after reduction and blocked the metal active sites. WP/SiO_2 catalysts present similar values for both synthesis methods. Meanwhile, MoP/SiO_2 from the phosphate method shows a higher CO chemisorption than the phosphite method. There is a relation between the crystallite size (calculated from the XRD data) and CO uptake. For each pair of catalysts the smaller crystallite size corresponds to the larger value of CO uptake, which is as expected due to the higher dispersion of smaller catalyst particles on the support. The average CO uptake values of the catalysts follow the order of: $\text{MoP/SiO}_2 > \text{Ni}_2\text{P/SiO}_2 > \text{CoP/SiO}_2 > \text{FeP/SiO}_2 > \text{WP/SiO}_2$. The dispersion was calculated from CO chemisorption and the known loading of the samples, and ranged from 1% to 17%.

3.3.4. X-ray diffraction

X-ray diffraction (XRD) data were collected to identify the crystalline phases in the catalysts (Fig. 3.2). All catalysts show a broad diffraction line at 2θ ($^\circ$) = 23-25 $^\circ$, typical of

amorphous silica. Except for Ni₂P/SiO₂, catalysts made from phosphite precursors show clearer diffraction patterns.

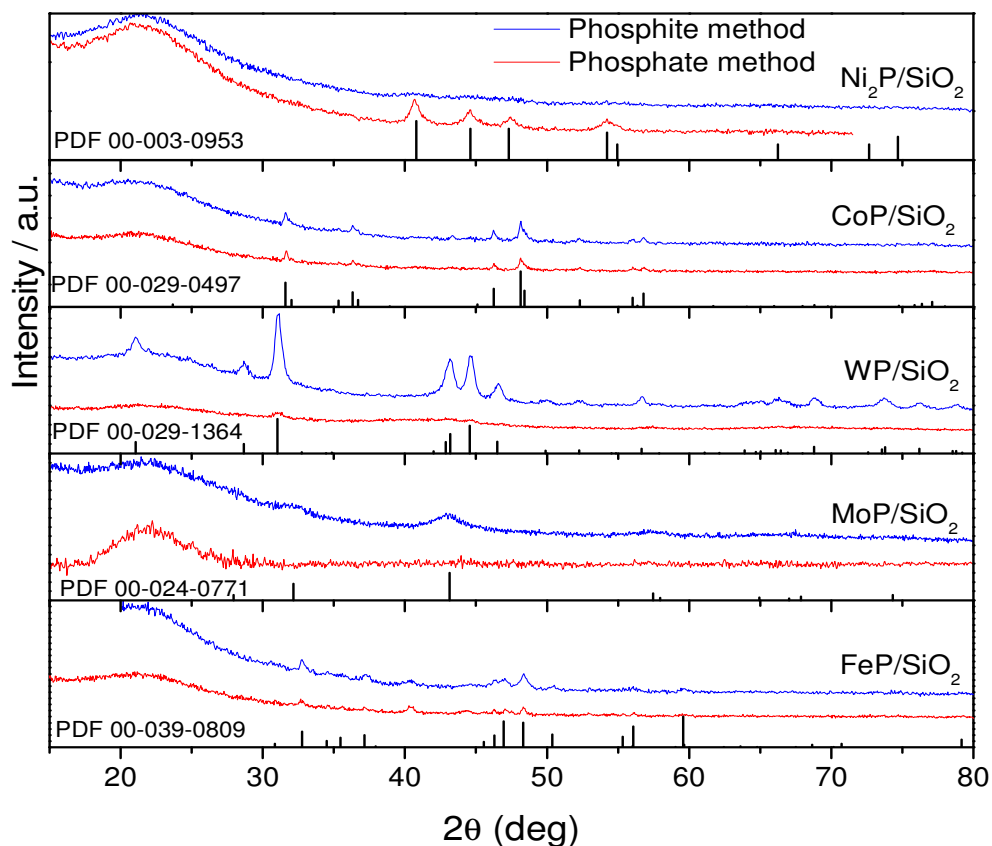


Fig. 3.2. X-ray diffraction patterns of supported phosphide catalysts

The XRD features for the supported iron phosphide catalysts by both methods are weak because of fluorescence by iron; however, FeP still can be identified from the peaks at 2θ (°) = 32.7, 46.3, 47.1 and 48.3° (PDF 00-039-0809). This result is consistent with previous findings for FeP synthesis, which in addition, showed that the synthesis requires an excess amount of phosphorus in the precursor [22]. The XRD pattern is slightly more defined for the phosphite

method. A small amount of Fe_2P was also detected with a feature at 2θ ($^\circ$) = 40.3° (PDF 01-076-0089).

For CoP/SiO_2 , though having different TPR profiles, the formation of CoP in both methods is confirmed with clear signature peaks at 2θ ($^\circ$) = 31.6 , 46.2 , and 48.1° (PDF 00-029-0497). Earlier research on Co_2P and CoP has established that CoP exhibits a higher activity and stability than Co_2P in the hydrotreating processes [40].

Nickel phosphide catalyst from the phosphate precursor shows the characteristic peaks of Ni_2P at 2θ ($^\circ$) = 40.7 , 44.5 , 47.4 , and 54.2° (PDF 00-003-0953). In contrast, the diffraction pattern of nickel phosphide from the phosphite method only shows a weak, broad feature at 40.7° , reflecting low crystallinity and small particle size probably as a consequence of the milder preparation conditions. Using this method, small particles can be formed even with higher loading up to (10 wt%) [24].

The MoP/SiO_2 (I) shows broad peaks for MoP at 2θ ($^\circ$) = 32.2 and 43.1° , whereas, the MoP/SiO_2 (A) does not present any peaks, probably because the lower reduction temperature (540°C) produced poorly crystallized phases. The MoP/SiO_2 (I) sample and a previously reported MoP/SiO_2 (A) synthesis [18] which displayed XRD peaks used a higher temperature (580°C). Other phases such as metallic Mo were not detected [37].

The XRD profile for WP/SiO_2 (I) shows sharp peaks, indicating a high crystallinity WP phase. On the other hand, though synthesized at higher reduction temperature, the WP/SiO_2 (A) only shows slight features for WP at 31.1 , 43.2 , and 44.6° . Apparently, it is more difficult to form the WP phase from the phosphate precursor, which starts at a higher oxidation state.

The particle size of the transition metal phosphides were calculated using the Scherrer equation for catalysts with substantive XRD patterns. CoP/SiO₂ (A and I) had the largest crystallite size followed by FeP/SiO₂ (A and I), Ni₂P/SiO₂ (A), and MoP/SiO₂ (I) (Table 3.2).

3.3.5. X-ray photoelectron spectroscopy

X-ray photoelectron spectroscopy (XPS) experiments were carried out on the most active catalysts from each category: Ni₂P/SiO₂ for the iron group phosphides (Fig. 3.3) and WP/SiO₂ for the group 6 phosphides (Fig. 4). Table 3 lists the binding energies for Ni 2*p*_{3/2}, W 4*f*_{7/2} and P 2*p*_{3/2} core levels and the observed phosphorous to metal atomic ratios. Ni 2*p* and W 4*f* core-level spectra were similar for both methods, although WP (I) and WP (A) were synthesized with different molar ratios. Calculated surface atomic ratio shows similar results for Ni₂P catalysts while on WP (I) there was twice as much phosphorous as on WP (A).

Table 3.3. Spectral parameters for Ni₂P/SiO₂ and WP/SiO₂ catalysts

Sample	Binding Energy (eV)				Surface atomic ratio	
	Ni 2 <i>p</i> _{3/2}		P 2 <i>p</i> _{3/2}		Ni ₂ P	P/Ni
	Ni ²⁺	Ni ⁺ /Ni ⁰	HPO ₃ H ⁻	PO ₄ ³⁻		
Ni ₂ P (I)	856.6	853.1	133.6	134.9	128.6	1.7
Ni ₂ P (A)	856.8	853.2	-	135.0	128.6	2.1

	W 4 <i>f</i> _{7/2}		P 2 <i>p</i> _{3/2}		WP	P/W
	W ⁶⁺	W ⁵⁺ /W ⁰	HPO ₃ H ⁻	PO ₄ ³⁻		
	WP (I)	36.3	31.1	133.7	135.0	128.7
WP (A)	36.4	31.3	-	134.7	128.6	1.7

Ni 2*p* core-level spectra, for both catalysts, involve two contributions (Fig. 3.3a). The first one is centered at 852.6 eV [24, 41, 42] and is assigned to Ni^{δ+} in the Ni₂P phase. The second one is between 856.6 and 856.8 eV, and corresponds to Ni²⁺ ions interacting possibly with the

unreduced (HPO_3H^-) or $\text{PO}_3^-/\text{PO}_4^{3-}$ anions as a consequence of a superficial passivation. Moreover, a broad shake-up satellite signal at approximately 6.0 eV above the Ni^{2+} species is observed due to the presence of divalent species [24, 40, 41]. The reduced Ni species from the Ni_2P phase has a binding energy that is very close to that of Ni metal (852.5-852.9 eV) [43], so its presence cannot be ruled out in both catalysts. The similarity of the XPS features for $\text{Ni}_2\text{P}/\text{SiO}_2$ via both methods and the confirmation by XRD of the presence of Ni_2P in the catalyst made by the phosphate method, and the catalytic activity to be presented later provide reasonable support for the presence of Ni_2P on the catalyst made by phosphite method even though no peaks were observed in the XRD profile of $\text{Ni}_2\text{P}/\text{SiO}_2$ (I).

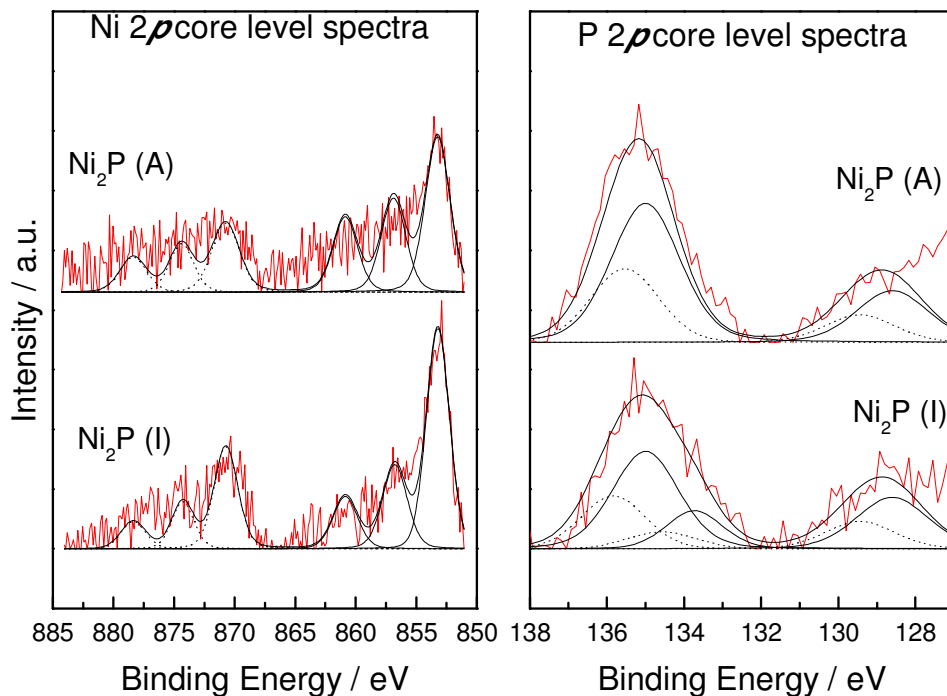


Fig. 3.3. Ni 2p and P 2p core-level spectra for silica supported nickel phosphide catalysts

The P 2*p* core-level spectrum for Ni₂P (A), phosphate method, shows two contributions (Fig. 3.3). The band at low binding energy values, 129.3 eV, is assigned to phosphorus in the form of metal phosphide, Ni₂P [24], while the band located at 135.0 eV is due to PO₄³⁻ species which appears as a consequence of the superficial passivation of phosphide species. The P 2*p* core-level spectrum for Ni₂P (I), phosphite method, shows an additional band assigned to unreduced phosphite species at 133.4 eV.

The W 4*f* photoemission spectra of the tungsten phosphides prepared by both methods are shown in Fig. 3.4. The decomposition of the spectra reveals several overlapping bands (Fig. 3.4). The first contribution is located at 31.2 eV and is ascribed to W^{δ+} or W⁰ species as previously reported [44] and is akin to that observed in tungsten phosphide [20]. The second contribution located at about 36.3 eV is assigned to W⁶⁺ species [45].

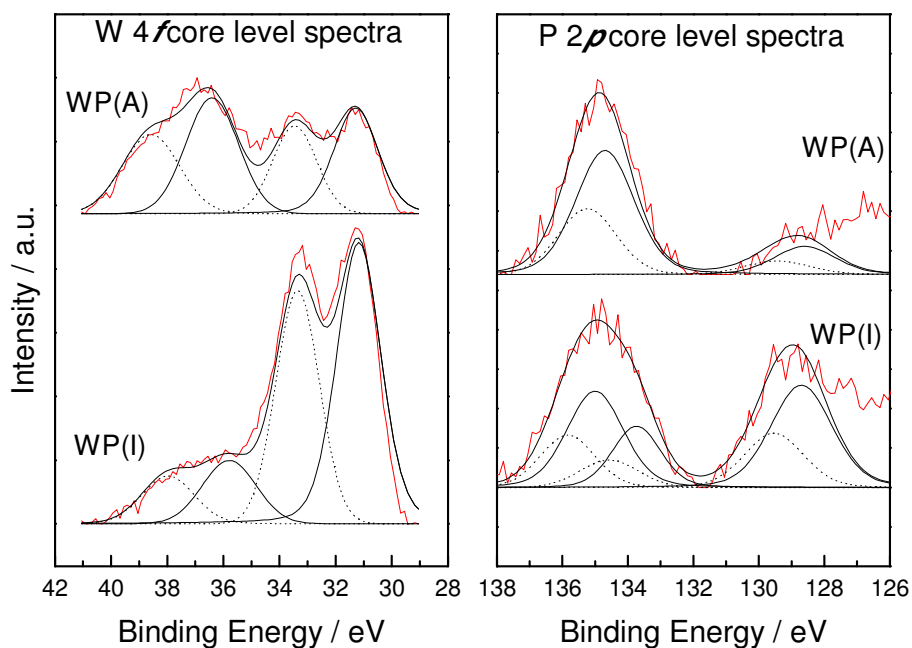


Fig. 3.4. W 4*f* and P 2*p* core-level spectra for silica supported tungsten phosphide catalysts

The P 2*p* spectra (Fig. 3.4) for tungsten phosphide catalysts are similar to those obtained for Ni₂P catalysts. The contributions are due to the phosphide phase at 128.7 eV and phosphate groups at 135.0 eV. The WP (I) catalyst also reveals the presence of phosphite (133.6 eV) due to the phosphorous excess present on this sample. The matching XPS figures of catalysts from both methods indicate that there is a WP phase in the bulk of the WP (A) particles although the XRD pattern did not show strong peaks.

3.3.6. Reactivity in hydrodeoxygenation (HDO) of 2-methyltetrahydrofuran (2-MTHF)

3.3.6.a) Reactivity as a function of temperature

The catalytic activity of these phosphides were evaluated for the HDO of 2-MTHF on a basis of 30 μmol active sites as measured by CO chemisorption. The gas phase feed contained 3.2 % of 2-MTHF in a H₂ stream with a H₂ to feed ratio of 30:1. The catalytic activities of all phosphides at different temperatures are presented as turnover frequencies (TOF) in Fig. 3.5. All catalysts have higher conversion at higher temperature as expected. Values of TOF together with the corresponding conversions at 275 °C and 350 °C are reported in Table 3.4.

Table 3.4. Conversions and apparent activation energies of 2-MTHF HDO on transition metal phosphides

Sample	Total Conversion % at Temperature °C					Apparent activation energy E_a (kJ/mol)	TOF (s^{-1}) at 275°C	TOF (s^{-1}) at 350°C
	250	275	300	325	350			
Ni ₂ P (I)	4	12	43	63	76	114	0.020	0.12
Ni ₂ P (A)	6	20	63	91	97	119	0.032	0.15
CoP (I)	1	4	10	35	66	108	0.0058	0.11
CoP (A)	0.5	2	8	17	40	137	0.0039	0.06
WP (I)	6	16	41	56	65	88	0.025	0.096
WP (A)	4	11	29	48	64	101	0.016	0.1
MoP (I)	2	5	21	32	63	113	0.0084	0.1
MoP (A)	2	6	17	30	31	109	0.0091	0.05
FeP (I)	-	-	1	3	2	116	-	0.0035
FeP (A)	0.5	1.4	5	14	24	117	0.0023	0.038
Pd/Al ₂ O ₃	0.4	1	2	4	5	77	0.0016	0.0074

At high temperature (350 °C) the phosphide catalysts prepared by the phosphite method perform with little difference at TOF $\sim 0.1 s^{-1}$ with an order of Ni₂P/SiO₂ > CoP/SiO₂ = MoP/SiO₂ \sim WP/SiO₂. The only exception is iron phosphide (I) which exhibits an extremely low activity - only 12 molecules of substrate got converted per active site per hour. For the phosphate method, a more distinct order was observed: Ni₂P/SiO₂ > WP/SiO₂ > CoP/SiO₂ \sim MoP/SiO₂ > FeP/SiO₂. In both methods, Ni₂P is the most effective catalyst, as observed in many HDS, HDN, and HDO studies [15, 22, 26]. A comparison within each pair of catalysts shows that the TOF values of CoP and MoP using the phosphite method are higher than those of the phosphate method. Meanwhile, for Ni₂P, WP, and FeP, catalysts prepared by the phosphate method are better than those made by the phosphite method, though the extents of differences vary. The TOF of Ni₂P (A) is about 1.4 times that of Ni₂P (I), WP (A) is practically the same as WP (I), while FeP (A) is ten-fold more active than FeP (I).

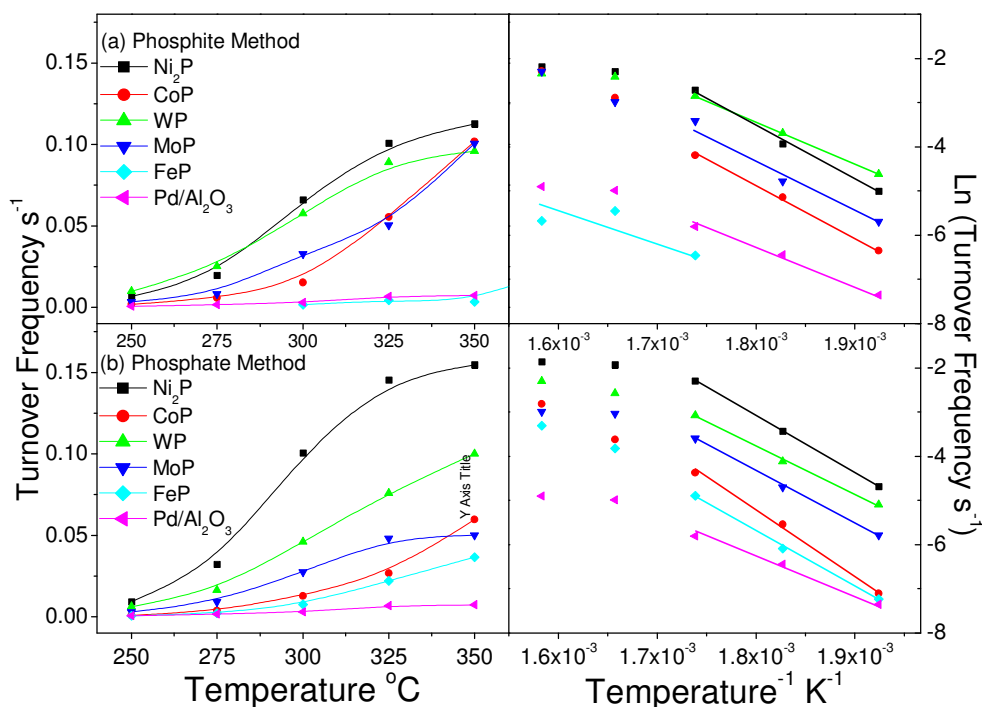


Fig. 3.5. Turnover frequency of 2-MTHF on transition metal phosphides

At lower temperature (275 °C), in both methods, supported FeP still shows the lowest activity as at higher temperature. Iron phosphides have been shown to be prone to coking and deactivation [22, 26]. Though most of previous studies focused on metal rich Fe₂P/SiO₂, similar weak activity and easy deactivation were also observed on FeP/SiO₂ in this HDO study of 2-MTHF. The order of activity of the catalysts prepared by the phosphite method is: WP > Ni₂P > MoP > CoP > FeP and that by the phosphate method is: Ni₂P > WP > MoP > CoP > FeP. Turnover frequencies within each rank are in the same order; for instance, the average TOF values are the following: 1st (WP (I) and Ni₂P (A)): 0.03 s⁻¹, 2nd (Ni₂P (I) and WP (A)): 0.02 s⁻¹, 3rd (MoP): 0.009 s⁻¹, and 4th (CoP): 0.005 s⁻¹. Overall, the differences in the TOF obtained from

using the phosphite or phosphate preparation methods are not extraordinarily large, indicating that the final materials are similar. However, as will be seen, the phosphite method can result in the deposition of excess phosphorus on the surface, which can affect the HDO reaction pathway.

A comparison of conversions for the catalysts prepared by the two preparation methods is given in Fig. 3.6. The graph allows visualization of the activity order among the catalysts. In general, phosphides from the phosphite method have higher conversions than those from the phosphate method, except for the supported Ni_2P and FeP . The catalysts' average total conversions have the following order: $\text{Ni}_2\text{P}/\text{SiO}_2$ (16%) > WP/SiO_2 (13.5%) > MoP/SiO_2 (5.5%) > CoP/SiO_2 (3%) > FeP/SiO_2 (0.7%). Supported Ni_2P , WP , and MoP catalysts show a steady trend of high HDO conversion (90-100%) in the temperature range 250 – 350 °C. Regardless of preparation method, $\text{Ni}_2\text{P}/\text{SiO}_2$ and WP/SiO_2 , representatives of iron group and group 6 phosphides, stand out in their performance. For this reason the samples were chosen for further study.

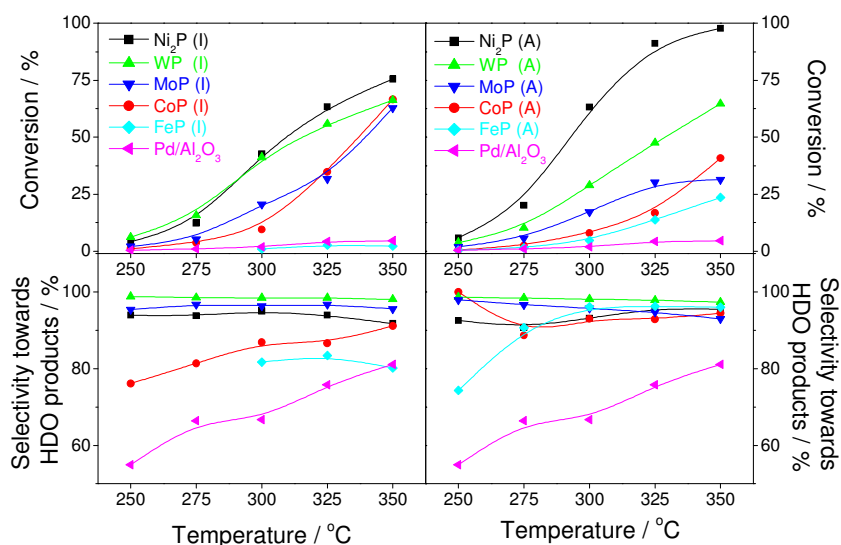


Fig. 3.6. Total conversion and selectivity towards HDO products of 2-MTHF reaction on transition metal phosphides

Table 3.4 shows the total conversions at various temperatures together with the apparent activation energy E_a and Fig. 3.5 exhibits the TOF results in Arrhenius plots. The apparent activation energy was calculated from the TOF values at lower temperatures (250-300 °C), using the Arrhenius equation. Iron phosphide from the phosphite precursor did not have any activity at 275 °C and showed deactivation at 350 °C, thus, its apparent activation energy was calculated in the range of 300 - 325 °C. Activation energies of the supported catalysts span the range of 88 kJ/mol - 137 kJ/mol. These values are lower than the C-O bond dissociation energy (360 kJ/mol), suggesting that direct CO bond scission did not occur. Oxygen removal may have occurred by a protonation of the oxygen first, followed by a hydrolysis.

Ni₂P catalysts from both methods show similar activation energy. The same was found for FeP. For CoP and WP, catalysts from the phosphite method have lower activation energy than those from the phosphite method, while the opposite was found for MoP/SiO₂ (Table 3.4). The differences in activation energy are not great, except possibly for the WP samples. The apparent activation energy calculated by the Arrhenius equation only provides an indication of the barrier for the overall chemical reaction, which might contain positive contributions from activated steps but negative contributions from equilibrated steps. Thus, when a multiple step sequence is involved, the order of activation energies is not directly related to a key reaction step unless the same mechanism is involved with all catalysts. As will be seen, this is not the case here.

The reactivity data for the commercial 5 wt% Pd/Al₂O₃ catalyst are reported in Fig. 3.5, Fig. 3.6, and Table 3.4. In general, the palladium catalyst was substantially out-performed by the phosphide catalysts with the only exception of FeP (I). As temperature increased from 250 to 350 °C, the total conversion of 2-MTHF on the Pd catalyst increased from 0.4 to 5%. These low

conversions may be due to coking and/or poisoning. A previous study [26] also reported a low performance of Pd/Al₂O₃ catalyst in the HDO of guaiacol. In the study the palladium catalyst showed a strong preference towards cleavage of the methyl group from guaiacol, producing catechol – a coking-inducing product. Product analysis for HDO of 2-MTHF (Fig. 3.9) consisted of a large proportion of a C4 mixture (30 - 45%), indicating a similar removal of a methyl group from 2-MTHF. Carbon residues might have formed a coke layer on the palladium catalyst, blocked the active sites, and thus resulted in the low conversions.

Product selectivity was calculated by the following equation:

$$\text{Selectivity} = \frac{\text{mol of product}}{\text{mol of 2-MTHF reacted}} 100\%$$

Table 3.5 reports total conversions, HDO conversions, and HDO product selectivity of all the catalysts in the region of moderate temperature and conversion. Special exception was made for FeP/SiO₂ because no product was detected for FeP/SiO₂ (I) at 275 °C, so values of HDO product selectivity for the iron phosphides at 300 °C are listed. Fig. 3.7-3.9 provide a visual presentation of specific products of the reaction on the phosphides. Based on the HDO products, the catalysts can be categorized in two groups. The first group consists of supported Ni₂P and CoP with C4 and C5 n-alkanes (such as butane and pentane) and 2-pentanone as predominant products (Fig. 3.7). The second group comprises supported group 6 metal phosphides (WP and MoP) and FeP with the main products being unsaturated C5 hydrocarbons (pentenes and pentadienes), pentane, and C4 hydrocarbons (Fig. 3.8, Fig. 3.9). Though total conversions of 2-MTHF vary over a wide range (1%-16%), all phosphides demonstrated a strong preference to HDO products (>74%). The order of average HDO conversions is as follows: MoP/SiO₂ > FeP/SiO₂ > WP/SiO₂ > Ni₂P/SiO₂ > CoP/SiO₂.

Table 3.5. Product selectivity for HDO of 2-MTHF on transition metal phosphides at 275 °C
***Conversions of FeP/SiO₂ were at 300°C**

Sample	Total conversion % (at 275°C)	Conversion to HDO products %	HDO products selectivity %			
			Pentane	Pentenes	Pentadienes	C4 Mixture
Ni ₂ P (I)	12	85	67	2	1	15
Ni ₂ P (A)	20	81	61	0	0	20
CoP (I)	4	74	43	2	0	29
CoP (A)	2	80	40	15	0	25
WP (I)	16	78	0	11	65	2
WP (A)	11	95	3	68	23	1
MoP (I)	5	95	14	70	7	4
MoP (A)	6	90	2	44	39	5
FeP (I)*	1	91	5	64	5	15
FeP (A)*	5	86	15	55	0	16
Pd/Al ₂ O ₃	1	72	17	12	0	43

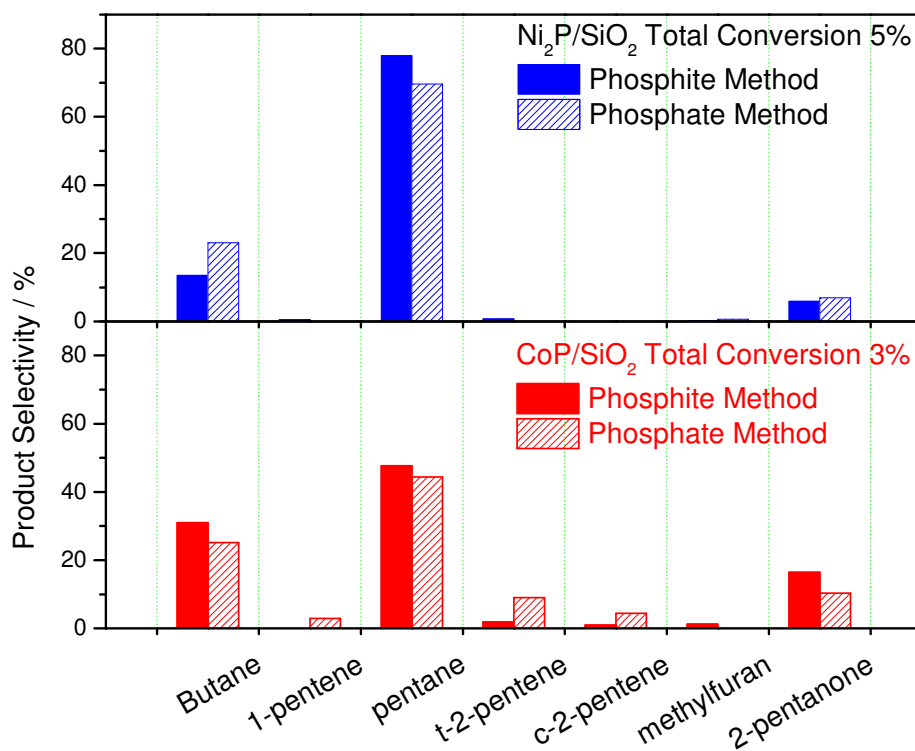


Fig. 3.7. Product selectivity of 2-MTHF reaction on Ni₂P/SiO₂ and CoP/SiO₂ at a total conversion of around 5%

The iron group metal (Ni, Co, and Fe) phosphides were expected to give similar HDO product distributions, yet only Ni₂P and CoP followed this trend (Fig. 3.7). The products of 2-MTHF HDO on Ni₂P/SiO₂ were mainly pentane (61-67%), butane (15-20%), 2-pentanone (5-8%), and very little alkenes (0-3%). CoP/SiO₂ produced less pentane (40-43%) and more 2-pentanone (10-16%) than Ni₂P/SiO₂. These products suggest that besides oxygen removal there were also dealkylation and dehydrogenation occurring and that 2-pentanol may have been an intermediate in the HDO mechanism, though not observed in the products stream. Ni₂P/SiO₂ performed better than CoP/SiO₂ with higher total conversions (>12%), higher HDO conversions (>81%), and higher selectivity to pentane (>61%). The Ni₂P/SiO₂ prepared by the phosphite method was better than the phosphate method in terms of higher HDO conversions and better yield toward pentane. In comparison, CoP/SiO₂ (A) was better than CoP/SiO₂ (I) because of the higher total HDO product yields.

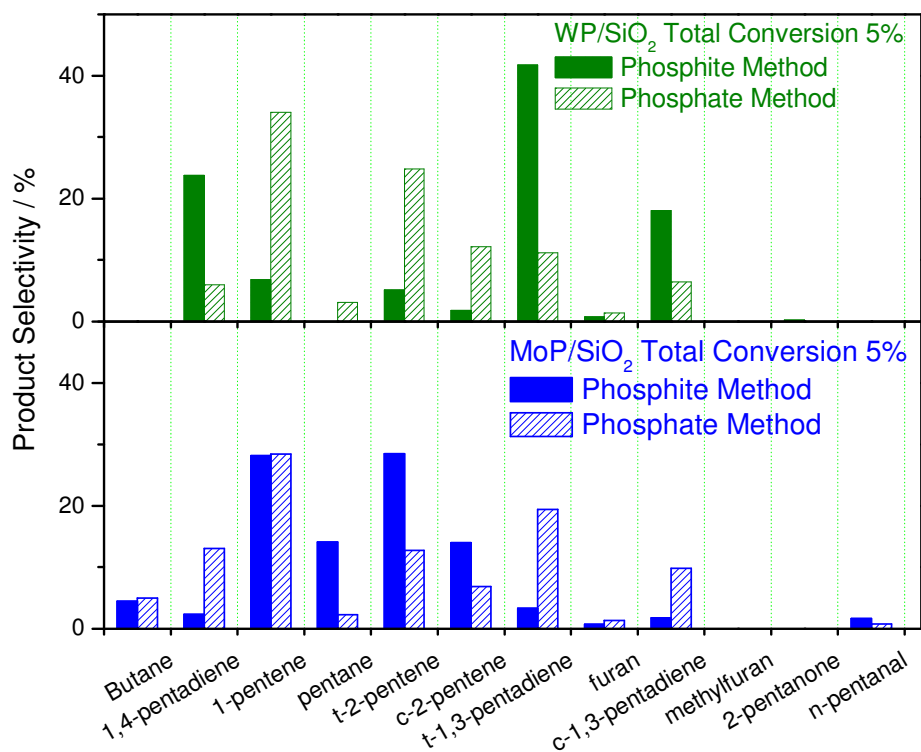


Fig. 3.8. Product selectivity of 2-MTHF reaction on WP/SiO₂ and MoP/SiO₂ at total conversion of 5%

Group 6 metal phosphides (WP/SiO₂ and MoP/SiO₂) showed a higher HDO conversion (78% to 95%) compared to iron group metal phosphides (Table 3.5). A clear preference towards unsaturated hydrocarbons was observed (Fig. 3.8) with very little 2-pentanone and C4-mixtures detected. This suggests that a different ring opening mechanism took place. The HDO of 2-MTHF with tungsten phosphides (I) and (A) shows different product distributions. For WP/SiO₂ (I) the formation of pentadienes was favoured, whereas for WP/SiO₂ (A) pentenes were preferred (Fig. 3.8). In general, WP/SiO₂ (A) gave a notably higher selectivity towards HDO (95% vs. 78%, Table 3.5). The surface metal-to-phosphorus ratio may have been responsible for this

sensitivity (Table 3.3). The P/W ratio was 3.4 for the phosphite method and 1.7 for the phosphate method. This will be discussed shortly.

Both MoP/SiO₂ (I) and (A) showed the highest HDO activity (although not total conversions) among all the phosphides examined here with MoP (I) better than MoP (A) (Table 3.5). The synthesis method also seems to affect the reaction pathways of the catalysts. MoP/SiO₂ (I) favoured production of pentenes and pentane while MoP/SiO₂ (A) gave additional large portions of pentadienes (Fig. 3.8). The phosphorus-to-metal ratio may again have been responsible for this sensitivity. The P:M ratio for preparation was 2:1 for the phosphite method and 1:1 for the phosphate method (Table 3.1).

The HDO of 2-MTHF on iron phosphide generated 5-15% of pentane, 15% of dealkylation products, 4-6% of 2-pentanone, and 55-64% of pentenes (Fig. 3.9). The large proportion of dealkylation products as well as the noticeable amount of 2-pentanone product resembles the results of other iron group metal phosphides (Ni₂P and CoP). Yet, more than half of the products were alkenes, indicating the occurrence of dehydration. FeP/SiO₂ (I) showed a higher selectivity towards HDO products; however, it had a much lower overall conversion than FeP/ SiO₂ (A).

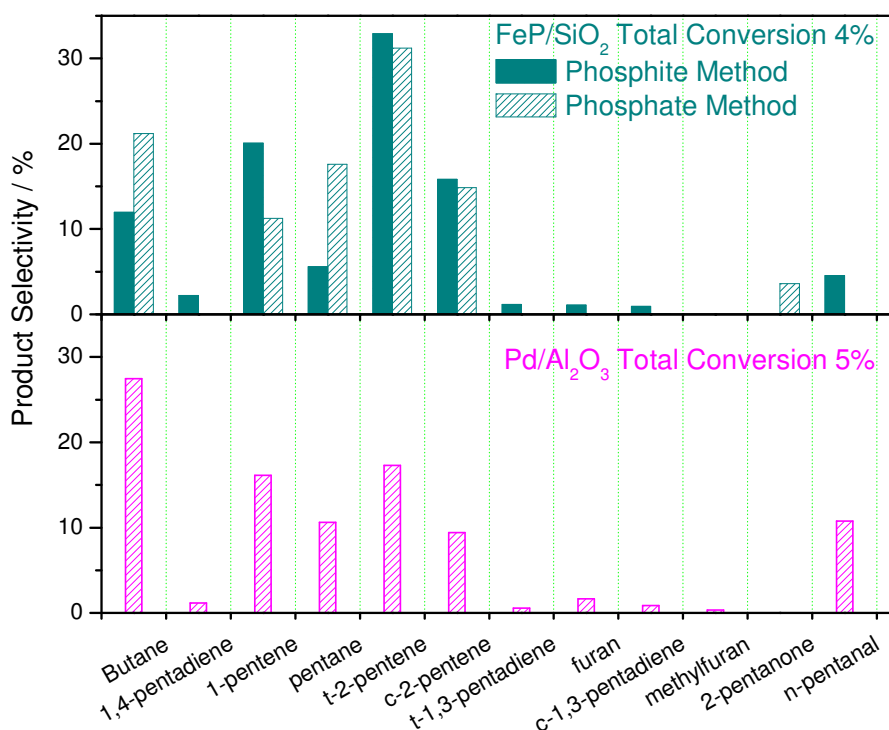


Fig. 3.9. Product selectivity of 2-MTHF reaction on FeP/SiO₂ and Pd/Al₂O₃ at total conversion of 5%

Pd/Al₂O₃ exhibited a high propensity for the removal of the methyl group from the 2-methyltetrahydrofuran reactant. The main products included an average of 12% pentane, 25% of pentenes, 38% of a C4 mixture, and 16% of 2-pentanone (Fig. 3.9). Similar results have been reported earlier on Pd/SiO₂ [46]. The large amount of C4-hydrocarbons and the absence of methane production coupled with a poor reactivity imply that coke deposition and/or self-poison by CO by-product occurred. The earlier study also showed substantial CO formation on supported metals of group 10 (Ni and Pt) – the same group as Pd – during HDO of 2-MTHF [47, 48]. In other studies of 2-MTHF hydrogenolysis on Pt/SiO₂ it was suggested that the produced

CO adsorbs strongly on the Pt surface and causes self-poisoning of the catalyst [47, 48]. This may also be the case here with Pd/Al₂O₃.

3.3.6.b) Reactivity as a function of contact time study

Contact time studies provide trends of product selectivity that help to identify reaction intermediate products and determine reaction pathways. Nickel and tungsten phosphides supported on silica have the highest HDO performance from the iron group and group 6 transition metals and therefore were chosen for study. At the moderate temperature of 300 °C and low contact time ranging from 0.3 s to 7 s, the catalysts exhibited a low catalytic activity (15% total conversion or less) in the kinetic-regime. Absence of internal diffusion limitations was checked using the Weisz-Prater criterion (C_{WP}) (see Supplementary Information) [49]. The highest value of C_{WP} was 0.3, satisfying the criterion ($C_{WP} < 1$), suggesting no internal diffusion limitations or concentration gradient within the catalyst. Fig. 3.10 shows selectivity of products in the HDO of 2-MTHF on Ni₂P/SiO₂. The contact time study on Ni₂P/SiO₂ (A) was chosen as representative in the iron group since catalysts from both synthesis methods demonstrated similar product selectivities during the reactivity experiments as a function of temperature (Fig. 3.7, Table 3.5). The product selectivities are presented in three groups: alkenes (1-pentene and 2-pentenes), oxygen containing compounds, and pentane. Selectivity for alkene products (trans, cis 2-pentene, and 1-pentene respectively) decreases with increasing contact time from 17%, 8%, and 6% to 5%, 2.5%, and 1.5% (Fig. 3.10), indicating that these are intermediate product species. Dehydrogenated products such as methylfuran also decrease with increasing contact time. On the other hand, the oxygenated products, 2-pentanone and n-pentanal, show the behavior characteristic of secondary products as they grow to a maximum (14% and 3.2% respectively)

and then decline. Pentane increases steadily from 28.5% to 49.5% as contact time progresses, demonstrating the characteristic of a final product (Fig. 3.10).

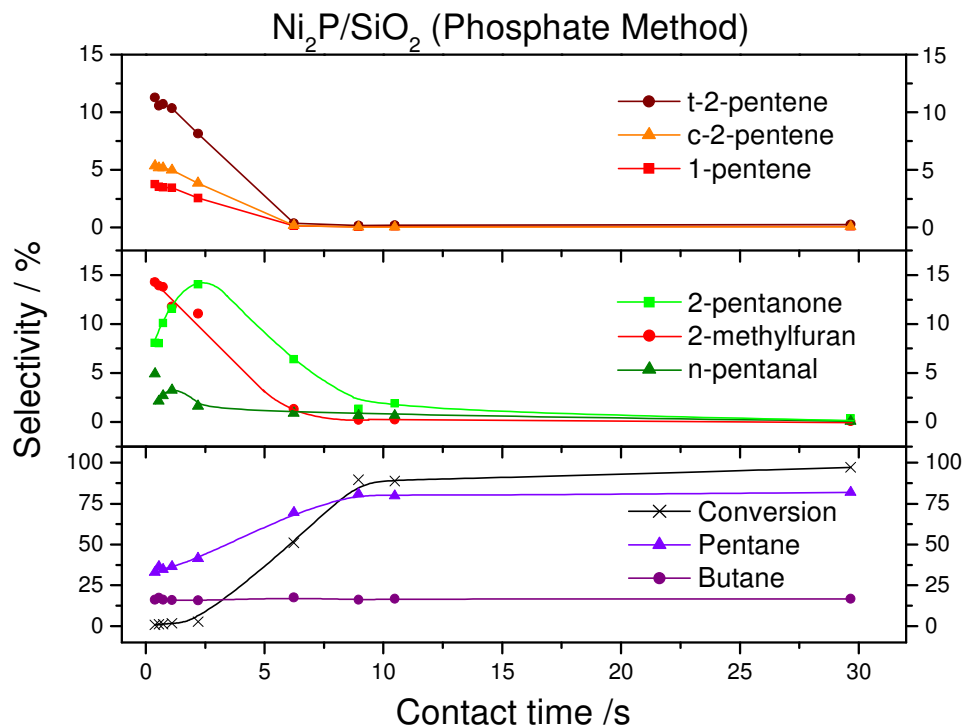
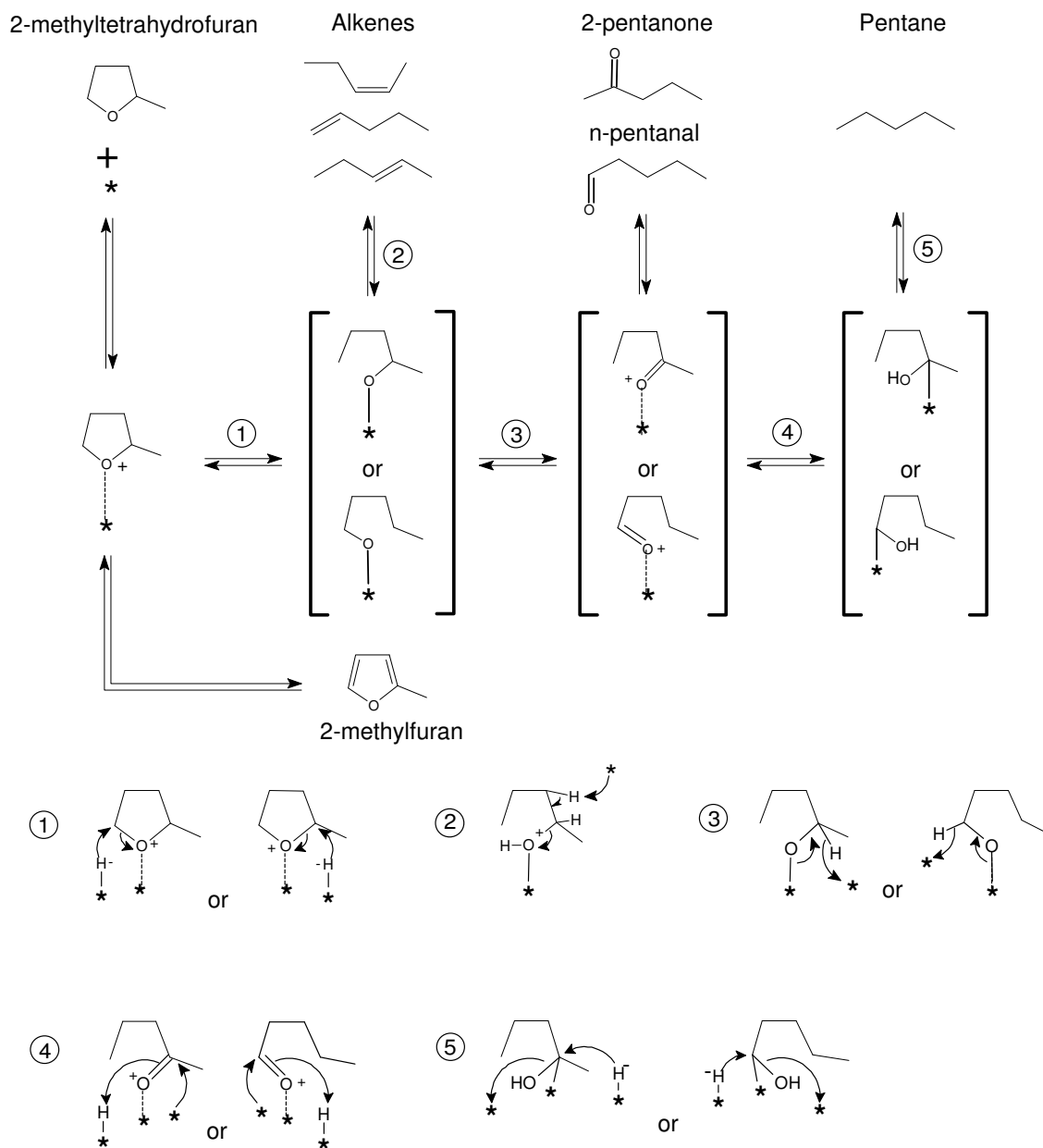


Fig. 3.10. Contact time study on Ni₂P/SiO₂

The results suggest that more than one reaction pathways occurs on the surface of Ni₂P/SiO₂. The less dominant reaction route involves dehydrogenation of 2-MTHF into a very small amount of methylidihydrofuran as primary product and methylfuran as secondary product. The main reaction route involves the production of alkenes, 2-pentanone and pentane. This route consists of a ring opening process and a C-O cleavage to give alkenes as primary product, 2-pentanone as secondary product, and pentane as final product. A consecutive reaction pathway such as 2-MTHF → alkenes → 2-pentanone → pentane is unlikely because of the need to oxidize alkenes to 2-pentanone in a highly reductive experimental environment. A more likely

possibility is that there are common intermediate species at the surface that react to form alkenes, 2-pentanone, and pentane in a sequential manner. This observation is similar to a previous study on the conversion of ethanol on Ni₂P/SiO₂ where ethanol was converted to acetaldehyde as primary product and ethylene as secondary product [50]. The contact time study results lead to the following “rake mechanism” scheme (Scheme 3.1). A rake mechanism is one which involves sequential steps of adsorbed species on a surface with each adsorbed species capable of desorbing. Thus, a diagram of the scheme shows prongs like in a rake for sweeping leaves.

The results can be rationalized in the following manner. The reactant 2-MTHF first adsorbs onto a vacant site on the catalyst surface. Nucleophilic attack by a surface hydride in step ① opens the ring to form a 1° or 2° alkoxide intermediate. Attack by a nearby electron-rich site on a hydrogen beta to the oxygen atom gives rise to an E2 elimination in step ② to produce the primary alkene products. The alkoxide intermediates may also go through an alpha hydride elimination in step ③ to form adsorbed carbonyl species with hydrogen transfer to vacant active sites. The carbonyl species can desorb as 2-pentanone or n-pentanal or can react further through a hydrogen transfer in step ④ to form adsorbed alcohol species. These can then undergo another hydrogen transfer in step ⑤ and release pentane.



Scheme 3.1. HDO reaction network of 2-MTHF on Ni₂P/SiO₂

In contrast to nickel phosphide, the HDO of 2-MTHF on tungsten phosphides supported on silica produced mostly unsaturated products. Interestingly, the selectivities followed different trends between the two catalyst preparation methods. Fig. 3.11 shows the selectivity to the three main groups of products: pentadienes, pentenes and pentane, and oxygenated compounds.

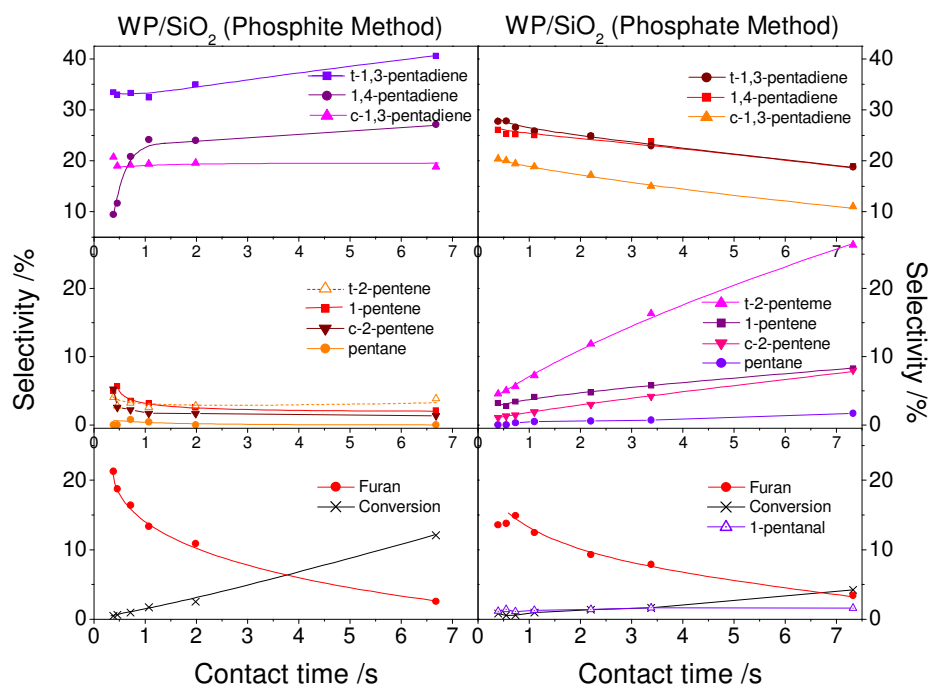
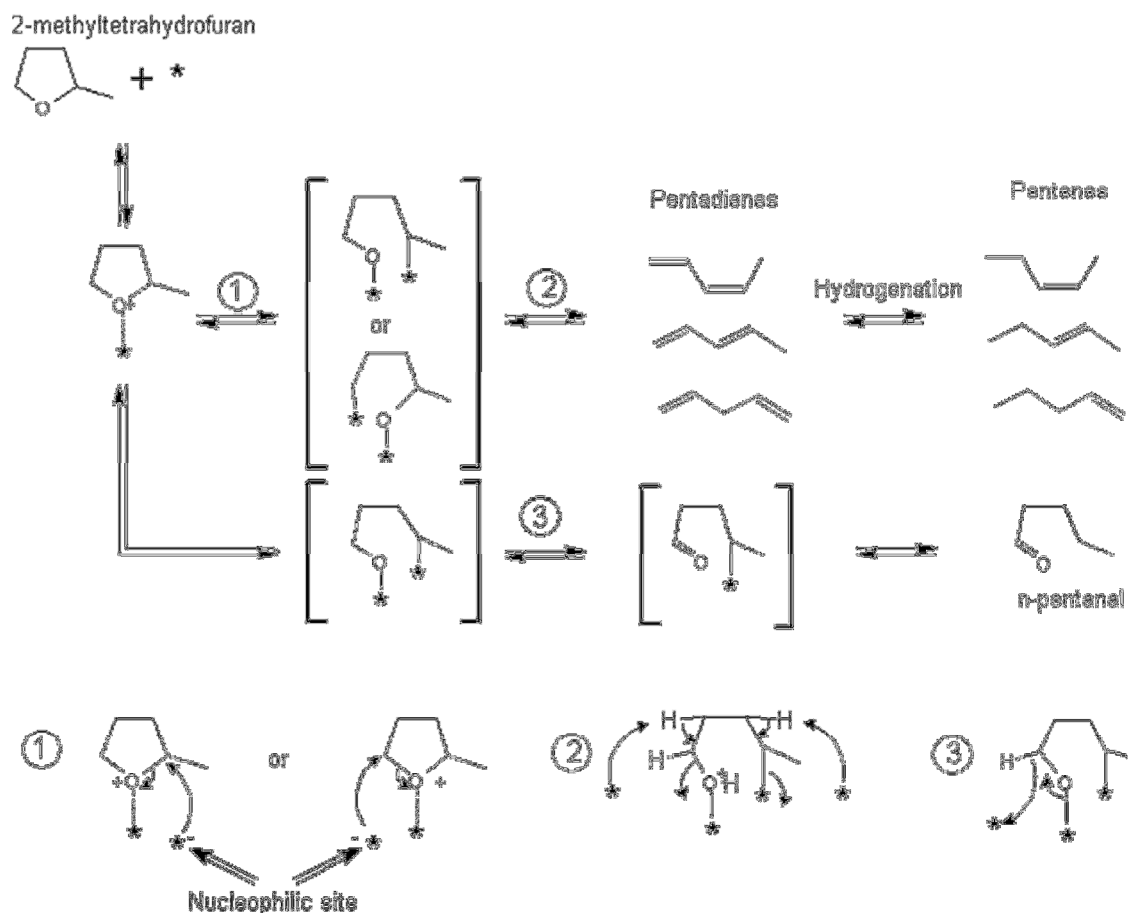


Fig. 3.11. Contact time study on WP/SiO₂ prepared by the phosphite and phosphate methods

Clear trends were observed on WP prepared by the phosphate method. The main products were pentadienes and pentenes. Selectivity to pentadienes decreased with increasing contact time, from 26%, 28%, and 20% to 19%, 19%, and 11% (1,4-pentadiene, t-1,3-pentadiene, and c-1,3-pentadiene respectively). In contrast, selectivity to pentenes increased with increasing contact time, suggesting that a hydrogenation process follows the production of pentadienes. Though pentane shares the same trend as with pentenes, its selectivity is extremely low (maximum 1.6%). Furan selectivity starts at 14% then peaks at 15% before quickly going down to 3.4%. Some pentanal is also detected though at low selectivity (< 2%) starting at 1.1% to reach 1.6% at the end.

The results demonstrate that pentadienes were formed first then pentenes and pentane, the latter produced by hydrogenation. This leads to a dominance of pentenes as final products at high conversion at steady-state. This interpretation agrees well with the steady-state results on supported tungsten phosphide (phosphate method) where at a 29% total conversion, HDO products were mainly pentenes (74%) rather than pentadienes (21%) (Fig. 3.8). These observations can be rationalized by another reaction scheme (Scheme 3.2). In order to produce pentadienes as primary products, it is likely that 2-MTHF was bound to two active sites. The 2-MTHF is first absorbed on a single site and then in step ① a surface nucleophilic species attacks a carbon alpha to the oxygen to form a doubly bound intermediate species. Next, nearby vacant sites induce beta hydride elimination in step ② and release pentadienes. The elimination follows E2 mechanism and the resulting pentadienes desorb immediately, having little chance to isomerize. Furthermore, at low residence time, the surface reaction follows kinetic regime which allows the production of the kinetic product – 1,4-pentadiene. The following step involves hydrogenation to form alkenes. The small amount of n-pentanal observed may have occurred by an alpha hydride abstraction from primary alkoxide species in step ③, followed by a hydrogen transfer to detach n-pentanal from the catalyst surface.

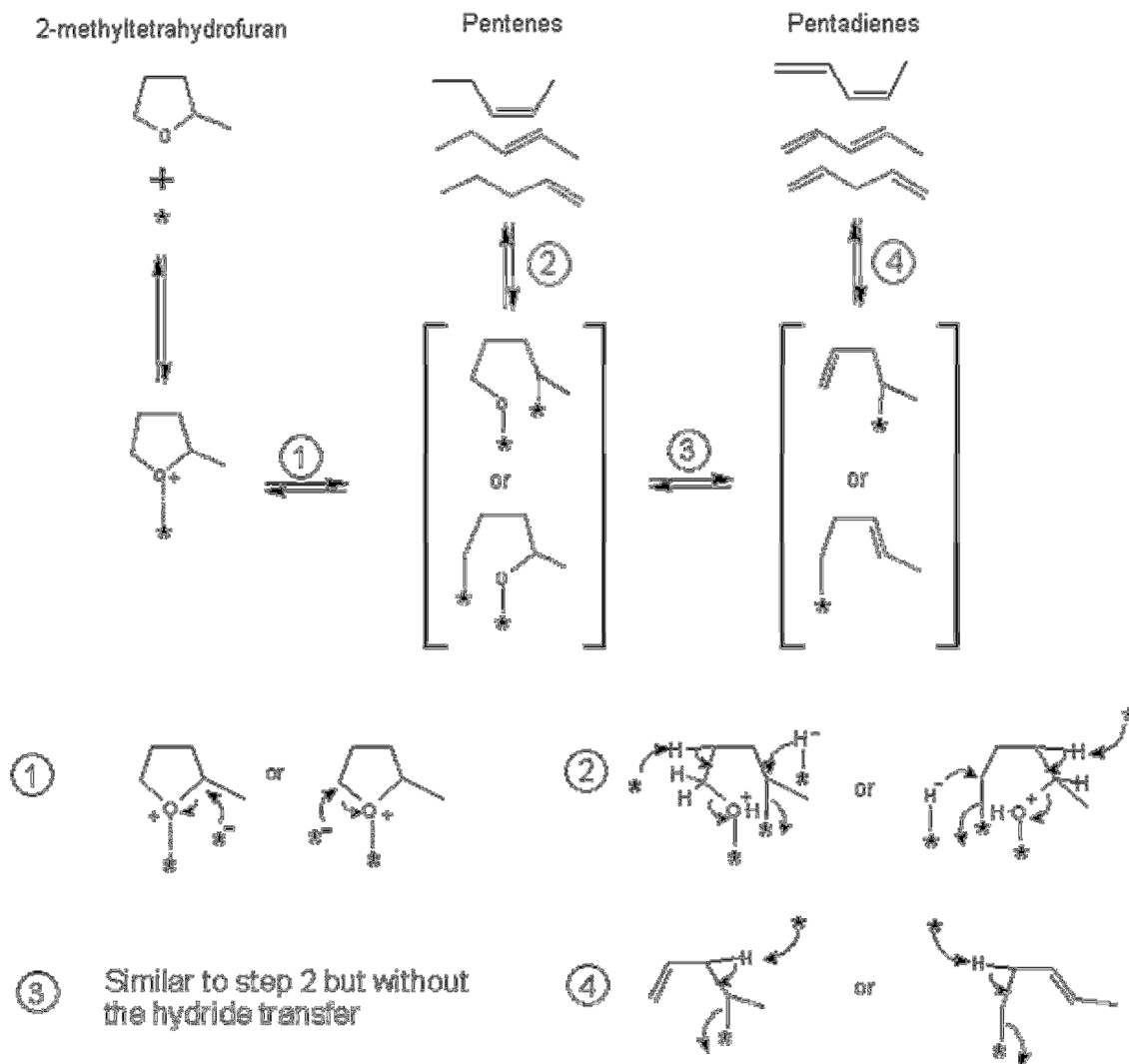


Scheme 3.2. HDO reaction network of 2-MTHF on WP/SiO₂ (phosphate method)

Interestingly, the contact time results from the HDO reaction on WP by the phosphite method show almost the opposite trend from that obtained by the phosphate method (Fig. 3.11). Pentadienes are the final products, except for c-1,3-pentadiene. The selectivity to 1,4-pentadiene and t-1,3-pentadiene respectively increases from 9.5% and 33.5% to 27% and 40.5%, whereas c-1,3-pentadiene selectivity starts at 21% to decrease only slightly to 19%. Meanwhile, 1-pentene and c-2-pentene have an initial selectivity of 5% and 5.2% that later decline to 2% and 1.3% respectively, indicating that they are primary products. The selectivity to t-2-pentene decreases

slightly from 4% to 2.6% during the initial period of contact time (0.4 s to 1 s) prior to a rise to 3.8%. Pentane was only produced at 0.7 s (0.75%) and 1 s (0.43%). Furan selectivity decreases steadily from 21% to 2.5% over the contact time range of 0.4 s to 7 s. These results are in good agreement with the steady-state findings at moderately high conversion (36%) in the reactivity test where the products are comprised of 81% pentadienes and 15% of pentenes (Fig. 3.8).

The results on tungsten phosphide made by the phosphite method can be rationalized by a scheme (Scheme 3.3) which has a similar starting point with the one for the phosphate method where an intermediate species formed by step ① is bound to two surface sites. However, a difference is that hydrogen removal occurs stepwise. A single beta-hydrogen abstraction from the intermediate coupled with a hydride transfer to release alkene products occurs as in step ②. Without a second hydride transfer to cause desorption from the catalyst surface, the doubly bound intermediate species transforms into an alkene intermediate species in step ③ which can react further via another beta hydrogen elimination to form pentadienes in step ④. The difference between the two pathways can be accounted for by the lack of readily available vacant sites on the surface of WP/SiO₂ by the phosphite method. In the phosphite preparation, the phosphorus-to-metal ratio was 2:1, twice as much phosphorous compared to the ratio of 1:1 used in the phosphate method. Furthermore, the phosphite method did not undergo calcination to remove the excess surface phosphorus. XPS data showed the surface P/M ratio was 3.4/1 for the phosphite method compared to 1.7/1 for the phosphate method. As a result, the phosphorous residues produce a catalyst surface with less vacant sites and this leads to a step by step consecutive dehydrogenation on WP made by the phosphite method. The findings demonstrate that surface composition in the form of phosphorus to metal ratio can play a crucial role in the reaction pathway adopted by the reactant.



Scheme 3.3. HDO reaction network of 2-MTHF on WP/SiO₂ (phosphite method)

3.4. Conclusions

Nickel, cobalt, tungsten, molybdenum, and iron phosphides were synthesized by reducing phosphite precursors and phosphate precursors. At 300 °C and 1 atm total conversions of 2-

methyltetrahydrofuran (2-MTHF) on supported phosphides followed the order of $\text{Ni}_2\text{P} > \text{WP} > \text{MoP} > \text{CoP} > \text{FeP} > \text{Pd/Al}_2\text{O}_3$. At 5% total conversion, the selectivity towards HDO products had the following trends: $\text{MoP} > \text{WP} > \text{Ni}_2\text{P} > \text{FeP} > \text{CoP}$ (phosphite method) and $\text{MoP} \sim \text{WP} > \text{FeP} > \text{Ni}_2\text{P} > \text{CoP}$ (phosphate method). In general, supported catalysts from the phosphite method had higher surface area and comparable selectivity towards HDO products at 5% total conversion. The main HDO products of supported iron metal phosphides group (Ni_2P and CoP) were pentane and butane, whereas those of group 6 metal phosphides and iron phosphide were mostly pentenes and pentadienes. The commercial catalyst $\text{Pd/Al}_2\text{O}_3$ and the weaker catalyst of the iron group – FeP/SiO_2 produced mostly pentenes and C4 mixtures. The results from contact time studies were used in the development of reaction networks for $\text{Ni}_2\text{P/SiO}_2$ and WP/SiO_2 for both preparation methods. $\text{Ni}_2\text{P/SiO}_2$ by both methods had similar selectivity profiles which could be explained by a rake mechanism that produced pentenes as primary products, 2-pentanone as a secondary product and pentane as a final product. On the other hand, selectivity profiles for WP/SiO_2 depended greatly on the preparation method. WP/SiO_2 by the phosphate method produced pentadienes prior to pentenes; therefore, the surface intermediate is suggested to have been bound to two active sites to allow simultaneous dehydrogenation for the initial pentadienes formation. WP/SiO_2 by the phosphite method produced pentenes prior to pentadienes indicating that sequential hydrogen removal took place on single sites. X-ray photoelectron spectroscopy of the WP from the phosphite method indicated more phosphorus on the surface than WP from the phosphate method, consistent with more single metallic sites present in the latter.

3.5. Supplementary Information

Weisz – Prater criterion for internal diffusion

The Weisz – Prater criterion C_{WP} uses measured values of the rate of reaction to determine if internal diffusion is limiting the reaction as follows:

$$C_{WP} = \frac{\text{Actual reaction rate}}{\text{A diffusion rate}} = \frac{-r'_{A(obs)}\rho_c R^2}{D_e C_{As}}$$

Internal mass transfer effects can be neglected when the value of C_{WP} is less than 1. The parameters used for the criterion are listed in Table 3.6. The observed rates $-r'_{A(obs)}$ were calculated at each contact time and listed along with the corresponding C_{WP} values in Table 3.7-3.9. Most values of C_{WP} are on the order of 10^{-2} and the highest value is around $0.3 < 1$, indicating that internal mass transfer effects can be neglected at the conditions employed for reactivity study in this paper.

Table 3.6. Parameters in the Weisz-Prater criterion

R	Catalyst particle radius / cm	0.08
ρ_c (Ni ₂ P)	Solid catalyst density for Ni ₂ P / g·cm ⁻³	0.3
ρ_c (WP)	Solid catalyst density for WP / g·cm ⁻³	0.4
C_{As} (300 °C)	Gas concentration at the catalyst surface / mol·cm ⁻³	6.8×10^{-7}
D_e	Effective diffusivity/ cm ² ·s ⁻¹	0.1

Table 3.7. The observed reaction rates and corresponding Weisz-Prater criterion for Ni₂P/SiO₂

Contact time / s	$-r'_{A(obs)} \times 10^6$ Observed reaction rate / mol g ⁻¹ s ⁻¹	C_{WP} Weisz-Prater criterion
0.39	2.09	0.059
0.56	2.28	0.064
0.75	1.66	0.047
1.13	1.84	0.052

2.26	1.45	0.041
6.38	7.98	0.225
9.18	9.76	0.276
10.75	8.27	0.233
30.40	3.20	0.090

Table 3.8. The observed reaction rates and corresponding Weisz-Prater criterion for WP/SiO₂ (I)

Contact time / s	$-r'_{A(obs)} \times 10^6$ Observed reaction rate / mol g ⁻¹ s ⁻¹	C _{WP} Weisz-Prater criterion
0.34	0.35	0.013
0.39	0.42	0.016
0.47	0.46	0.017
0.73	0.47	0.018
1.10	0.48	0.018
2.03	0.46	0.017
6.84	0.64	0.024

Table 3.9. The observed reaction rates and corresponding Weisz-Prater criterion for WP/SiO₂ (A)

Contact time / s	$-r'_{A(obs)} \times 10^6$ Observed reaction rate / mol g ⁻¹ s ⁻¹	C _{WP} Weisz-Prater criterion
0.40	0.89	0.033
0.56	0.46	0.017
0.75	0.35	0.013
1.13	0.36	0.014
2.26	0.27	0.010
3.46	0.21	0.008
7.51	0.24	0.009

References

1. A. A. Lappas, S. Bezergianni, I. A. Vasalos, *Catal. Today*, 145 (2009) 55.
2. G. W. Huber, S. Iborra, A. Corma, *Chem. Rev.*, 106 (2006) 4044.
3. J. J. Bozell, G. R. Petersen, *Green Chem.*, 12 (2010) 539.
4. J. Zakzeski, P. C. A. Bruijninx, A. L. Jongerius, B. M. Weckhuysen, *Chem. Rev.*, 110 (2010) 3552.
5. D. Mohan, C. U. Pittman Jr., P. H. Steele, *Energ. Fuel*, 20 (2006) 848.
6. L. Zhang, C. Xu, P. Champagne, *Energ. Convers. Manage.*, 51 (2010) 969.
7. A. Oasmaa, S. Czernik, *Appl. Catal. A: Gen.*, 13 (1999) 914.
8. Bridgwater, A. V., *Appl. Catal. A: Gen.*, 116 (1994) 5.
9. Demirbas, M. F., *Appl. Energ.*, 86 (2009) S151.
10. Furimsky, E., *Appl. Catal. A: Gen.*, 199 (2000) 147.
11. P. M. Mortensen, J. D. Grunwaldt, P. A. Jensen, K. G. Knudsen, A. D. Jensen, *Appl. Catal. A: Gen.*, 407 (2011) 1.
12. A. Gutierrez, R. K. Kaila, M. L. Honkela, R. Slioor, A. O. I. Krause, *Catal. Today*, 147 (2009) 239.
13. A. Y. Bunch, U. S. Ozkan, *J. Catal.*, 206 (2002) 177.
14. E. M. Ryymin, M. L. Honkela, R. R. Viljava, A. O. I. Krause, *Catal. Today*, 147 (2009) 239.
15. Oyama, S. T., *J. Catal.*, 216 (2003) 343.
16. S. T. Oyama, T. Gott, H. Zhao, Y. -K. Lee, *Catal. Today*, 143 (2009) 94.
17. S. T. Oyama, X. Wang, Y. -K. Lee, K. Bando, F. G. Requejo, *J. Catal.*, 210 (2002) 207.
18. P. Clark, X. Wang, S. T. Oyama, *J. Catal.*, 207 (2002) 256.
19. W. Li, B. Dhandapani, S. T. Oyama, *Chem. Lett.*, (1998) 207.
20. P. Clark, W. Li, S. T. Oyama, *J. Catal.*, 200 (2001) 140.
21. J. A. Cecilia, A. Infantes-Molina, E. Rodríguez-Castellón, A. Jiménez-López, *Appl. Catal. B: Environ.*, 92 (2009) 100.
22. X. Wang, P. Clark, S. T. Oyama, *J. Catal.*, 208 (2002) 321.
23. J. A. Cecilia, A. Infantes-Molina, E. Rodríguez-Castellón, A. Jiménez-López, *J. Phys. Chem. C*, 113 (2009) 17032.
24. J. A. Cecilia, A. Infantes-Molina, E. Rodríguez-Castellón, A. Jiménez-López, *J. Catal.*, 263 (2009) 4.
25. S. T. Oyama, X. Wang, Y. -K. Lee, W. -J. Chun, *J. Catal.*, 221 (2004) 263.
26. H. Y. Zhao, D. Li, P. Bui, S. T. Oyama, *Appl. Catal. A: Gen.*, 391 (2011) 305.
27. V. M. L. Whiffen, K. J. Smith, *Energ. Fuel*, 24 (2010) 4728.
28. X. Duan, Y. Teng, A. Wang, V. M. Kogan, X. Li, Y. Wang, *J. Catal.*, 261 (2009) 232.
29. T. I. Korányi, Z. Vít, D. G. Poduval, R. Ryoo, H. -S. Kim, E. J. M. Hensen, *J. Catal.*, 253 (2008) 119.
30. H. Loboue, C. Guillot-Deudon, A. Florin Popa, A. Lafond, B. Rebours, C. Pichon, T. Cseri, G. Berhault, C. Geantet, *Catal. Today*, 130 (2008) 63.
31. Q. Guan, W. Li, M. Zhang, K. Tao, *J. Catal.*, 263 (2009) 1.
32. G. Shi, J. Shen, *J. Mater. Chem.*, 19 (2009) 2295.

33. C. L. Yaws, P. K. Narasimhan, C. Gabbula. *Yaws' handbook of antoine coefficients for vapor pressure*. 2009 [cited 2012 10/04]; Available from: <http://www.knovel.com>.
34. C. Stinner, Z. Tang, M. Haouas, Th. Weber, R. Prins, J. Catal., 208 (2002) 456.
35. A. Wang, L. Ruan, Y. Teng, X. Li, M. Lu, J. Ren, Y. Wang, Y. Hu, J. Catal., 229 (2005) 314.
36. J. A. Rodriguez, J. Y. Kim, J. C. Hanson, S. J. Sawhill, M. E. Bussell, J. Phys. Chem. B, 107 (2003) 6276.
37. A. Motesinos-Castellanos, T. A. Zepeda, B. Pawelec, E. Lima, J. L. G. Fierro, A. Olivas, J. A. de los Reyes, Appl. Catal. a: Gen., 334 (2008) 330.
38. K. A. Layman, M. E. Bussell, J. Phys. Chem. B, 108 (2004) 10930.
39. Z. Feng, C. Liang, W. Wu, Z. Wu, R. A. van Santen, C. Li, J. Phys. Chem. B, 107 (2003) 13698.
40. A. W. Burns, K. A. Layman, D. H. Bale, M. E. Bussell, Appl. Catal. A: Gen., 343 (2008) 68.
41. S. J. Sawhill, D. C. Phillips, M. E. Bussell, J. Catal., 215 (2003) 208.
42. S. J. Sawhill, K. A. Layman, D. R. Van Wyk, M. H. Engelhard, C. Wang, M. E. Bussell, J. Catal., 231 (2005) 300.
43. Briggs, D., *Practical surface analysis by auger and x-ray photoelectron spectroscopy*, ed. M. P. Seah. 1983, New York: Wiley.
44. J. F. Moulder, W. F. Stickle, P. E. Sobol, K. D. Bomben, J. Chastain, *Handbook of x-ray photoelectron spectroscopy*. 1992, Eden Prairie, MN: Perkin Elmer.
45. G. E. McGuire, G. K. Schweitzer, T. A. Carlson, Inorg. Chem., 12 (1973) 2450.
46. F. Notheisz, M. Bartok, J. Catal., 71 (1981) 331.
47. U. Gennari, R. Krammer, H. L. Gruber, Appl. Catal., 11 (1984) 341.
48. U. Gennari, R. Krammer, H. L. Gruber, Appl. Catal., 44 (1988) 239.
49. P. B. Weisz, C. D. Prater, Adv. Catal. Relat. Subj., 6 (1954) 143.
50. D. Li, P. Bui, H. Y. Zhao, S. T. Oyama, T. Dou, Z. H. Shen, J. Catal., 290 (2012) 1.

Chapter 4

Kinetic and Spectroscopic Study of Deoxygenation of 2-Methyltetrahydrofuran over Supported Nickel Phosphide Catalyst

4.1. Introduction

The general conclusion from reaction network studies of oxygenated aromatic compounds is that the aromatic ring must be hydrogenated at least partially prior to ring opening (Chapter 1), indicating saturated cyclic ethers as a potential intermediate in hydrodeoxygenation. Previous chapters presented the successful preparation of silica supported transition metal phosphides among which $\text{Ni}_2\text{P}/\text{SiO}_2$ showed high reactivity towards hydrodeoxygenation of ethanol and 2-methyltetrahydrofuran. In this chapter, attention is placed on investigating the effect of the reactants (2-MTHF and H_2) partial pressure on the HDO reactions and monitoring the surface species involved in the reactions.

4.2. Materials and Experiments

4.2.1. Materials and synthesis

The supported nickel phosphide catalyst was synthesized via a phosphate precursor as reported earlier (Chapter 3). In short, nickel (II) nitrate ($\text{Ni}(\text{NO}_3)_2 \cdot 6\text{H}_2\text{O}$ (Alfa Aesar, 99.6%))

was added into an ammonium hydrogen phosphate ((NH₄)₂HPO₄ (Aldrich 99%)) solution with a 2:1 metal to phosphorous ratio. The resulting solution was impregnated onto a silica support (Cab-osil ® EH5 supplied by Cabot Corp) using the incipient wetness method. The mixture was dried at 120 °C for 4 h and calcined at 600 °C for 6 h to obtain the final phosphate precursor. Then, a temperature programmed reduction in a H₂ stream (1 dm³ min⁻¹ of H₂ per gram of precursor) was carried out to obtain the corresponding phosphide. The temperature was increased from 25 °C to 580 °C at a rate of 2 °C min⁻¹. Finally, the catalyst was cooled to 25 °C in a He stream and was passivated in a 0.5 % O₂/He stream for 2 h.

4.2.2. General characterization

General characterization techniques such as X-ray diffraction, carbon monoxide (CO) chemisorption and Brunauer Emmett Teller (BET) surface area measurements were carried out to confirm the presence of nickel phosphide and to quantify the active sites on the catalyst.

4.2.3. Low temperature reactivity test

The reactivity test was carried out in a cylindrical quartz reactor packed with 2.9 g of catalyst – equivalent to 338 μmol of active site on the basis of CO uptake. Prior to the test, the supported nickel phosphide was reactivated in H₂ as temperature increased at a rate of 5 °C min⁻¹ from 25 °C to 450 °C and held at this temperature for 2 h. The reactivity experiment was carried out at atmospheric pressure and temperatures ranging from 150 to 225 °C. The reactant was fed to the catalyst bed in a H₂ stream (100 cm³ (NTP) min⁻¹) flowing first through a saturator

containing a solution of 95 volume % of 2-MTHF and 5 volume % of heptane as an internal standard. The saturator was kept at 0 °C to ensure a stable feed concentration. The feed composition was obtained as follows by applying the Antoine equation to obtain the vapor pressures of 2-MTHF and heptane and then using Raoult's law for liquid mixtures. The Antoine equation has the form $\log P^{\text{sat}} = A - \frac{B}{T+C}$ and the coefficients A, B, and C are 7.13891, 1339.48, and 234.353 respectively for 2-MTHF and 7.04605, 1341.89, and 223.733 for heptane [1] and gave a saturated vapor pressure at 0 °C (saturator temperature) of P^{sat} 26.5 mmHg for 2-MTHF and 11.2 mmHg for heptanes. The total vapor pressure of the mixture was 26 mmHg. At atmospheric pressure, the gas-phase concentration of the reactant 2-MTHF in H₂ is 3.3 molar %. The space velocity and contact time were 667 h⁻¹ and 149 s respectively and were calculated by the following equations:

$$\text{GHSV} = \frac{\text{Feed volume flow rate}}{\text{Volume of the catalyst bed}}$$
 in which feed volume flow rate is 6000 [cm³ (NTP) h⁻¹] and volume of the catalyst bed is 9 cm³.

$$\text{Contact time} = \frac{\text{Quantity of active sites of catalyst loaded}}{\text{Reactant molar flow rate}}$$

The products were monitored by an online gas chromatograph (SRI 8610B) equipped with an HP-1 100m x 0.25mm capillary column and a flame ionization detector. The reactants and products were identified by comparing their retention times with those of commercial standards and confirmed by gas chromatography – mass spectrometry (GC-MS) (Hewlett – Packard, 5890-5927A).

4.2.4. Kinetic test

The kinetic test was carried out in a trickle bed reactor at 300 °C and a total pressure of 1 atm. The reactant solution (a liquid mixture of 2-MTHF and 5 vol % of heptane) was delivered into the reactor via a vaporizer kept at 300 °C. A mixed flow of H₂ and He (total flow rate of 127 cm³ (NTP) min⁻¹) brought the vaporized reactant to the reactor chamber. The catalyst bed in the middle of the reactor chamber was made with 100 mg of supported nickel phosphide well mixed in 1.5 g of quartz with the same pelletized size to a total volume of 2 mL. The kinetic study consisted of two subsets of experiments. In the first one the partial pressure of 2-MTHF was kept constant at 14.3 atm while the partial pressure of H₂ was varied in the following order (in atm): 85 → 83 → 66 → 29 → 14 → 21 → 47 → 74. In the second experiment the partial pressure of H₂ was kept constant at 67 atm while the partial pressure 2-MTHF was varied as follows (in atm): 4.4 → 18 → 31 → 34 → 25 → 15 → 11 → 7.7. As in the reactivity test the products were monitored via an online gas chromatograph (SRI 8610B) equipped with an HP-1 100m x 0.25mm capillary column and a flame ionization detector.

4.2.5. Temperature-programmed desorption

Temperature programmed desorption (TPD) of 2-MTHF in He (and H₂) was conducted in a tubular quartz reactor using 0.50 g of catalyst. The catalyst underwent the same reactivation as discussed above and was cooled in He flow (100 cm³ (NTP) min⁻¹). At 30 °C and after a 20 min period of stabilization in He, the reactor was evacuated to a pressure of less than 0.1 mmHg, and then was filled with saturated vapor of 2-MTHF to a pressure of 20 mmHg. Excess and lightly adsorbed 2-MTHF was removed by a second evacuation. Then, the catalyst was flushed in a He

flow (100 sccm) for 30 min at 1 atm. Temperature programmed desorption in He (or H₂) (50 cm³ (NTP) min⁻¹) started as temperature increased from 30 °C to 600 °C at a rate of 3 °C min⁻¹. The desorption was monitored by a quadruple mass spectrometer. The monitored masses and their relative intensity are summarized below.

Table 4.1: Masses monitored during temperature programmed desorption of 2-MTHF and their relative intensity

Chemical	m/z	Relative intensity
2-MTHF	71.0	100
	41.0	51.8
	42.0	47.9
2-Pentene	55.0	100
	42.0	41.8
	70.0	38.6
2-Pentanone	43.0	100.0
	86.0	20.2
	41.0	11.9
Pentanal	44.0	100
	29.0	52.3
	41.0	41.0
n-Pentane	43.0	100.0
	42.0	78.3
	41.0	50.5
1-Pentanol	42.0	100.0
	55.0	65.1
	70.0	51.0
2-Pentnaol	45.0	100.0
	55.0	18.7
	43.0	13.7

4.2.6. Fourier transform infrared (FTIR) spectroscopic experiments

The spectroscopic study was carried out using a Digilab Excalibur Series FTS 3000 spectrometer. The detachable reaction cell was positioned parallel to the beam line so that the laser beam passed through the catalyst wafer prior to reaching the liquid N₂ cooled mercury-

cadmium-telluride detector. The chamber had an outlet and inlet for gas flows and a thermocouple connected to a temperature controller to monitor and control the sample temperature. Potassium bromide windows were placed at the ends of the cell and perpendicular to the beam line. The catalyst sample was made of 32.5 mg of finely ground Ni₂P/SiO₂ pressed into a self-supporting wafer (13 mm in diameter). The catalyst was pretreated in H₂ (100 cm³ (NTP) min⁻¹) at 450 °C for 2 h prior to experiments. Background spectra were taken as the catalyst cooled down in either H₂ or He (100 cm³ (NTP) min⁻¹). All spectra are shown with subtraction of the background contribution. In the temperature programmed desorption experiments, the catalyst sample was dosed with 0.32% 2-MTHF/He (100 cm³ (NTP) min⁻¹) until saturation at 100°C and 1 atm. Then, sample was purged with carrier gas for 300 s to remove the excessive 2-MTHF. During temperature programmed desorption spectra were recorded at each 25 °C interval as temperature increased from 100 – 300 °C. In the steady-state experiments, 2-MTHF was fed at a constant concentration (0.32 mol %) in either H₂ or He and temperature was varied in the range of 105 - 300 °C at 50 °C interval, spectra were taken after the catalyst was stabilized in 2-MTHF stream for 1.5 h. The transient experiment has the same conditions with the steady state experiment; however, spectra were taken starting at the moment 2-MTHF was introduced.

4.3. Results and Discussion

4.3.1. Characterization

Fig. 4.1 shows the X-ray diffraction pattern for Ni₂P/SiO₂ exhibiting a broad peak at 20° assigned to amorphous silica support and three sharp peaks at 40.8°, 44.6°, and 47.3° that correspond well to the PDF pattern for Ni₂P. The broad peak at 54.2° consists of an overlap of the two peaks at 54.2° and 54.9° suggested by the PDF pattern. XRD result confirms the presence of Ni₂P crystals in the catalyst. Furthermore, the crystal size of Ni₂P particles can be deduced from the width at half-height of the three most prominent peaks at 40.8°, 44.6°, and 47.3° (Table 4.2, Supplementary Information).

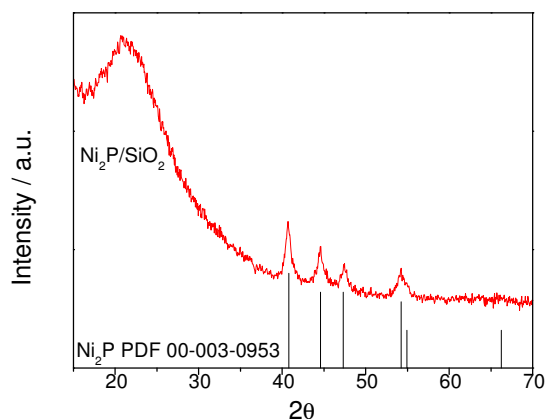


Fig. 4.1 X-ray diffraction pattern of Ni₂P/SiO₂

Table 4.2 lists the results of general characterization done on the catalyst. These results are in close agreement with the ones reported previously. Crystallite size was calculated using the Scherrer equation $D_c = \frac{K\lambda}{\beta \cos(\theta)}$ in which K is the shape factor with a value of 0.9, λ is the X-ray wavelength, β is the line broadening at half- maximum intensity in radians (accounting for instrumental broadening of 0.1°), and θ is the Bragg angle. The equation was applied to the three peaks at 40.8°, 44.6°, and 47.3° (see Supplementary Information) and the average value for

crystallite size is reported in Table 4.2. Measurements from CO chemisorption provided estimation of the dispersion of metal sites following the equation:

$$\text{Dispersion (\%)} = \frac{\text{CO uptake } \left(\frac{\mu\text{mol}}{\text{g}}\right)}{\text{Loading } \left(\frac{1.16 \mu\text{mol}}{\text{g}}\right)} 100\%$$

Table 4.2: Characterization results of Ni₂P/SiO₂; * BET surface area value of SiO₂

Catalyst	BET Surface Area m ² g ⁻¹	Crystallite Size nm	CO uptake μmol g ⁻¹	Dispersion %
Ni ₂ P/SiO ₂	177 (334*)	14.5	115	10

4.3.2. Low temperature reactivity test

The reactivity of 2-MTHF on Ni₂P/SiO₂ at low temperatures is presented as an Arrhenius plot of 2-MTHF conversion over Ni₂P/SiO₂ (Fig. 4.2). A large catalyst loading (2.9 g) and a long contact time (149s) between the reactant and the active sites were used to obtain conversion at low temperatures and help improve the accuracy of the observed reaction activation energy. The temperatures were varied in a downwards and upwards order as follows: 275-250-200-175-150-162-187-223-225 °C to ensure the data were not affected by deactivation. The result exhibits an excellent linear relationship between the logarithm of the turnover frequency and the inverse temperature. The apparent activation energy for 2-MTHF conversion on Ni₂P/SiO₂ from the slope of the plot was 134 kJ/mol. This value is slightly higher than the one reported previously because the reaction rate starts to deviate from Arrhenius temperature dependency as temperature

increases past 225 °C yet a previous study started from 250 °C [Chapter 3]. Furthermore, in the previous study there were less data points available to establish an accurate value. Kreuzer and Kramer reported an apparent activation energy value of 75kJ/mol for the conversion of tetrahydrofuran on silica supported Pt [2]. The higher value from 2-MTHF conversion indicates a more complex reaction network for this molecule.

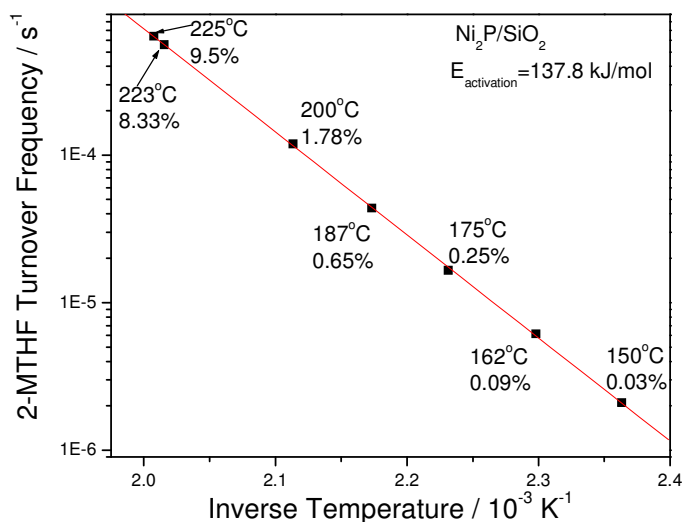


Fig. 4.2. Arrhenius plot of 2-MTHF conversion over Ni₂P/SiO₂

4.3.3. Kinetic study

Previous result on 2-MTHF reactions on Ni₂P/SiO₂ showed that pentenes and 2-methylfuran are primary products, 2-pentanone and n-pentanal are secondary products, and pentane and butane are final products [Chapter 3]. The dependence of 2-MTHF conversion on the partial pressures of H₂ and the reactant itself was investigated via a kinetic study (Table 4.3). In the first series 2-MTHF partial pressure was held constant while H₂ pressure was varied and in

the second series the opposite was carried out. In both experiments, total conversion and turnover frequency increase as the concentration of either H₂ or 2-MTHF increases. However, the conversion of 2-MTHF shows a larger dependence (~ 3 times) on the partial pressure of 2-MTHF than H₂. As 2-MTHF pressure decreases 77 % from 34.1 to 7.7 kPa, the rate decreases 81 % from 0.75 to 0.14 s⁻¹; meanwhile, as H₂ pressure decreases 83 % from 83.9 to 14.5 kPa, the rate of 2-MTHF converted decreases 28 % from 0.32 to 0.23 s⁻¹.

Table 4.3 Effects of H₂ and 2-MTHF partial pressures on the conversion of 2-MTHF over Ni₂P/SiO₂

Partial Pressure kPa		Total Conversion %	TOF mol mol ⁻¹ active site s ⁻¹	Product Selectivity %				
H ₂	2-MTHF			C4	Pentenes	Pentane	2- methylfuran	2- pentanone
83.9	14.5	56.9	0.32	22.4	0.9	51.4	5.4	18.9
75.1	14.5	55.2	0.31	22.2	1.0	42.2	7.3	25.6
67.0	14.5	54.3	0.30	20.8	0.9	42.5	6.7	27.5
47.8	14.6	50.3	0.28	18.7	1.2	35.6	9.9	33.6
29.0	14.5	49.0	0.27	15.4	1.6	24.0	16.9	41.0
20.9	14.5	43.8	0.24	16.8	2.8	21.8	23.1	34.8
14.5	14.6	41.8	0.23	16.2	6.6	13.3	36.6	26.7
67.0	34.1	55.4	0.75	20.3	1.5	32.0	13.9	30.6
67.0	30.9	54.7	0.65	19.6	1.5	32.6	13.2	31.0
67.0	24.8	55.3	0.53	20.4	1.2	33.3	11.9	31.7
67.0	17.9	55.5	0.38	18.7	1.3	44.3	10.0	24.8
67.0	14.5	54.3	0.30	20.8	0.9	42.5	6.7	27.5
67.0	10.7	50.8	0.21	22.2	1.0	44.1	7.9	24.2
67.0	7.7	48.5	0.14	20.6	1.1	37.9	10.2	29.5

The selectivity of products is presented in Table 4.3 and Fig. 4.3. In the experiment where H₂ partial pressure was varied, a trend similar to contact time study was observed. As H₂ concentration increases, the selectivity towards unsaturated products such as 2-methylfuran and

pentenes decreases, the selectivity towards the secondary product of 2-pentanone reaches a maximum, the selectivity towards saturated final product of pentane increases significantly, and the selectivity towards the cracking product of butane rises slightly. Note that the reaction is not mass transfer limited as the Weisz-Prater coefficient is less than ; thus, the concentrations in the immediate vicinity of the active sites are the same in the bulk. Considering the experimental conditions which involve an excessive amount of catalytic active sites (11.5 $\mu\text{mol CO uptake}$) available for the reaction of a constant reactant flow (6.4 $\mu\text{mol s}^{-1}$), the observed selectivity profiles hint that the surface reaction may be the rate limiting step in the reaction mechanism.

In the experiment where 2-MTHF partial pressure was varied, total conversion and selectivity of the products do not show a significant change as in the H_2 experiment (Fig. 4.3). The results show two steady regions below and above 20 kPa of 2-MTHF. As 2-MTHF flow increases past 7.9 $\mu\text{mol s}^{-1}$ (corresponding to 18.5 kPa), the selectivity towards the final product – pentane shifts to a lower steady value, the selectivity towards intermediate products – 2-pentanone, 2-methylfuran, and pentenes shifts to higher values while butane stays relatively the same. The cracking product maintains a steady selectivity in both experiments as well as in the contact time study (Fig. 4.3). If either the adsorption of 2-MTHF or the desorption of the products was rate-limiting then the surface reaction would be fast, resulting in a high and steady selectivity towards pentane and low selectivity towards other intermediate products. The case was not observed here. Therefore, the surface reaction is likely the rate limiting step for the HDO mechanism.

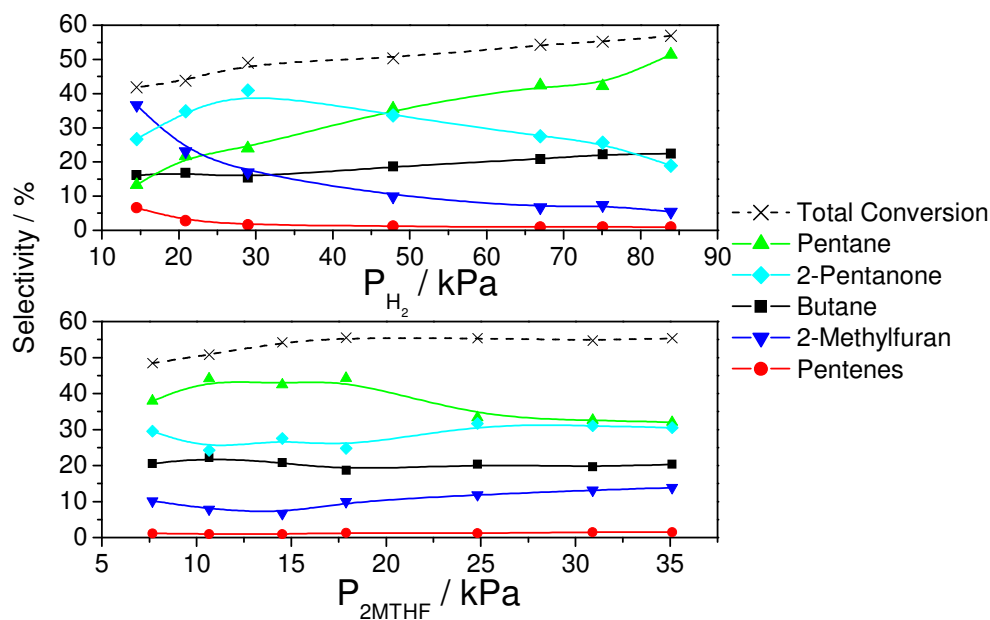


Fig. 4.3. Selectivity of products in partial pressure experiment

The apparent order of 2-MTHF conversion with respect to H_2 and 2-MTHF was obtained using the simple power rate law where TOF is the turnover frequency with the unit of mole of 2-MTHF converted per mole of active sites per second, k is the overall rate constant, P_{2MTHF} and P_{H_2} are the partial pressures of 2-MTHF and H_2 , and a and b are the orders of the reaction with respect to 2-MTHF and H_2 , respectively.

$$TOF = kP_{2MTHF}^a P_{H_2}^b$$

The power rate law could be presented in a linear form as:

$$\ln(TOF) = \ln(k) + a\ln(P_{2MTHF}) + b\ln(P_{H_2})$$

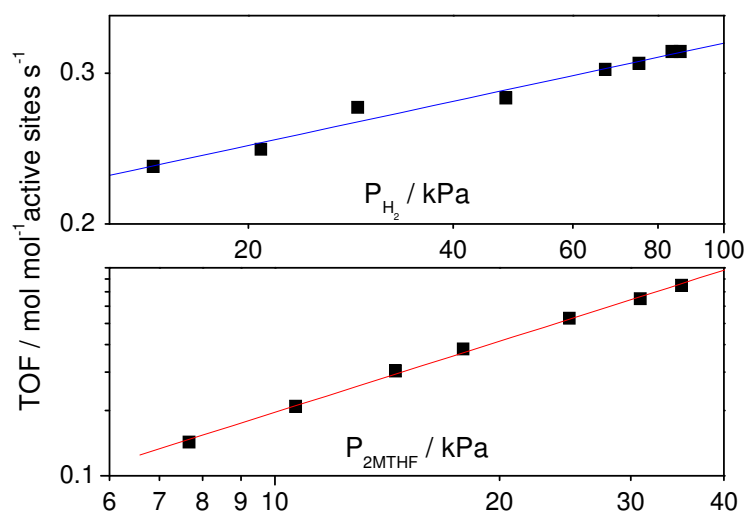


Fig. 4.4. Estimate of reaction order of H₂ and 2-MTHF

Overall reaction orders a and b are determined from the slopes in Fig. 4.4. The conversion of 2-MTHF on Ni₂P/SiO₂ has the order of 1.07 with respect to 2-MTHF and 0.17 with respect to H₂. The first order of 2-MTHF is as expected. The low reaction order of H₂ may be due to the dehydrogenation reaction to form 2-methylfuran. At low H₂ partial pressures (< 30 kPa), the conversion of 2-MTHF produces more 2-methylfuran, pentenes, and 2-pentanone than the saturated pentane. It is likely that the adsorbed species donate hydrogen to active sites and later on utilize the hydride species for their transformations, thus reducing the dependence on the gas phase hydrogen. This is consistent with the excellent hydride transfer capacity of nickel phosphides. On the other hand, extra hydrogen is necessary to form the final product – pentane.

4.3.4. Temperature programmed desorption

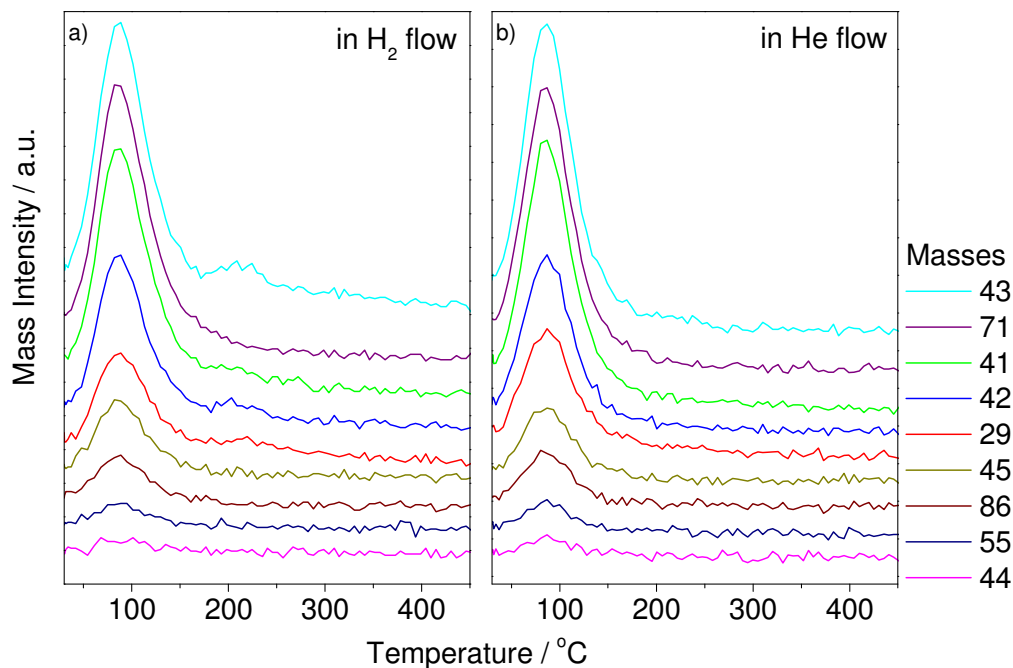


Fig. 4.5: Temperature programmed desorption of 2-MTHF on Ni₂P/SiO₂ in H₂ and He at atmospheric pressure, heating rate of 3 °C min⁻¹, injection temperature was at 30 °C

Spectra of masses 29, 41, 42, 43, 44, 45, 55, 71, and 86 in H₂ flow (a) and He flow (b) during temperature programmed desorption were shown (Fig. 4.5). Main peaks centered at 87 °C were detected in both He and H₂ flow. These peaks indicate desorption of the physisorbed 2-MTHF. At around 210 °C a small peak was detected for masses 43, 42, 41 and 29 in H₂ flow but not in He flow. These masses could originate from either pentane, 2-pentanone or n-pentanal. Additional TPD was carried out with a focus on masses 43, 42, 41, and 71. An elevated injection temperature of 150 °C was applied to eliminate the physisorption of 2-MTHF. The results are shown in Fig. 4.6. Here, mass 71 has no peak, indicating that this is not 2-MTHF. Masses 43, 42,

and 41 exhibit clear peaks at 210 °C and are consistent with the previous TPD experiment (Fig. 4.5). Relative intensity of each mass was calculated by taking the area of the desired mass divided by the area of mass 43 and multiplied by 100. The calculation gives 100, 60, and 60 as relative intensity of mass 43, 42, and 41 respectively. These values are closest to the value listed for n-pentane in Table 4.1. The deviation from the reference values may be due to the very small amount of pentane produced.

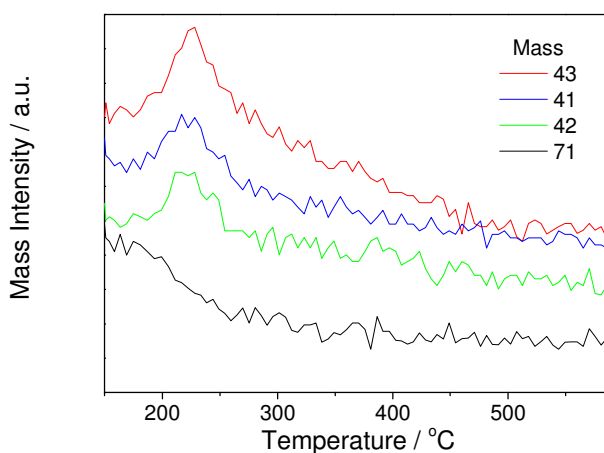


Fig. 4.6 Temperature programmed desorption of 2-MTHF on Ni₂P/SiO₂ in H₂ at atmospheric pressure, heating rate of 3 °C min⁻¹, injection temperature was at 150 °C

4.3.5. Fourier transform spectroscopy

In order to observe the catalyst surface during reaction, a series of infrared spectroscopy measurements were carried out at conditions of temperature programmed desorption, steady-state reaction, and transient reaction. All spectra shown here include background subtraction at the temperature of the measurement. Table 4.4 lists the main peaks and their assignments.

Temperature programmed desorption of 2-MTHF on the pure SiO₂ support is shown in Fig. 4.7. The high wavenumber region in the left panel shows a peak at 3746 cm⁻¹, a broad feature from 3500 to 3100 cm⁻¹, and a cluster of peaks at 2978, 2939, and 2880 cm⁻¹. The first two are contributions from hydroxyl group associated with the silica support [3-5] and hydrogen-bond interactions, and the last is from C-H stretching of the methyl and methylene groups of 2-MTHF [6]. There seems to be interactions between 2-MTHF and the SiOH group due to the negative feature surrounding the peak at 3746 cm⁻¹. The lower wavenumber region in the right panel shows peaks at 1464 cm⁻¹ with a shoulder at 1450 cm⁻¹, and a doublet at 1385 and 1360 cm⁻¹, attributed to C-H bending vibrations (δ_s CH₂, δ_{as} CH₃ and δ CH for secondary C) of 2-MTHF [7]. Slight features at 1070 and 1000 cm⁻¹ are from either C-O-C or C-C-C stretching of 2-MTHF. The results showed that 2-MTHF is adsorbed weakly on pure the SiO₂ support, probably via hydrogen bonding with the silanol group. As temperature increases 2-MTHF simply desorbs from the inert support without any chemical conversion; no features were observed for any products. For this reason, the same experiment in He was not carried out.

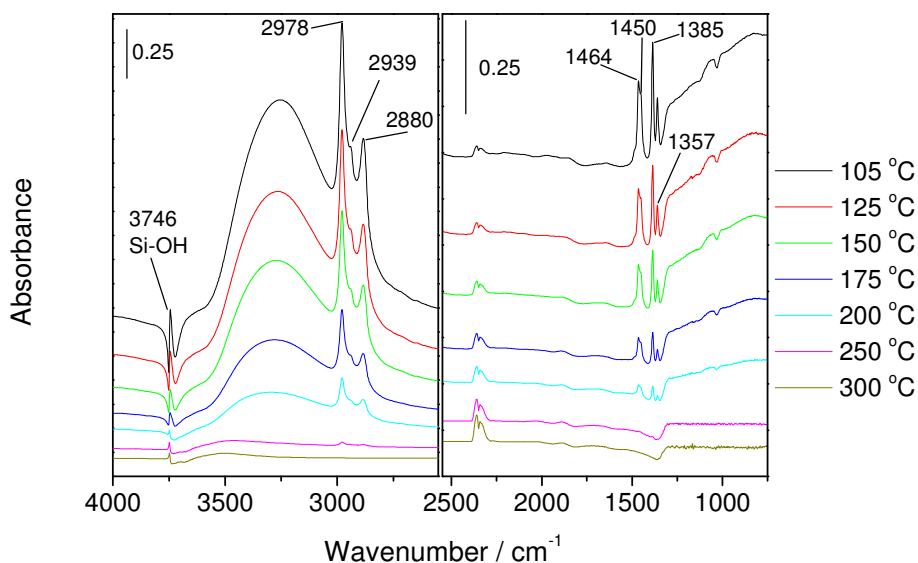


Fig. 4.7. Temperature programmed desorption of 2-MTHF from the support SiO₂ in H₂

Considerable changes occur in the FTIR spectra as nickel phosphide is incorporated to the support (Fig. 4.9). As 2-MTHF adsorbs on and desorbs from the catalyst, the following peaks were noticed:

1/ Two negative peaks at 3745 and 3667 cm⁻¹ are attributed to the consumption of the hydroxyl groups associated with the support and phosphorus. Their negative intensity decreases as temperature increases; eventually the peaks turn positive indicating a recovery of the corresponding hydroxyl species. The silanol groups on the SiO₂ are not acidic enough even for the protonation of 2-methylpiperidine – a basic compound [8], therefore it is likely that silanol group does not protonate 2-MTHF here. Instead, the P-OH group is likely to be involved here. A previous FTIR analysis of P₂O₅/SiO₂ showed the P-OH vibration at 3660 cm⁻¹. This band is close to that of Ni₂P/SiO₂ catalyst. It was proposed that the P-OH groups at 3668 cm⁻¹ are associated

with the Ni_2P particles (Fig. 4.8) and the oxygen in these hydroxyl groups probably came from incompletely reduced phosphate species [8].

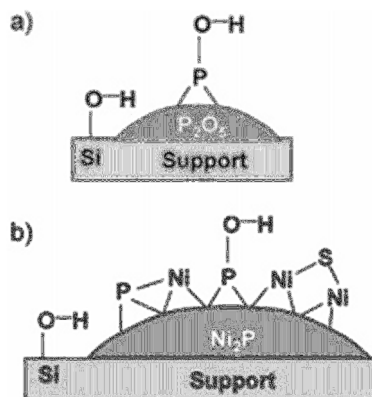


Fig. 4.8 Proposed structural models of (a) $\text{P}_2\text{O}_5/\text{SiO}_2$ and (b) $\text{Ni}_2\text{P}/\text{SiO}_2$ [8]

2/ An overlapped signal at 2978, 2939, and 2885 cm^{-1} is assigned to aliphatic C-H stretching that comes from the adsorbed reactant and products.

3/ A peak at 2450 cm^{-1} originates from P-H stretching of phosphite species [7]. Unlike the trend observed in the PO-H stretching (3667 cm^{-1}) which continues rising even as all species desorbed, the P-H peak (2450 cm^{-1}) diminishes along with the desorption of surface species, suggesting some hydrogen transfer activity between the adsorbed species and the phosphite species.

4/ A peak at 2066 cm^{-1} that starts at 200 $^\circ\text{C}$ and reaches a maximum at 250 $^\circ\text{C}$. This peak belongs to adsorbed CO species, a decarbonylation product. The peak position matches with the Ni^0 -CO complex [9, 10], indicating that the decarbonylation reaction takes place near or on Ni metal sites – a result observed in previous studies [11, 12].

5/ A broad region contains peaks at 1693 and 1634 cm^{-1} in which the former is assigned to a C=O stretch from adsorbed ketone species and the latter is assigned to a C=C stretch from adsorbed alkenes [7]. The accompanying alkene C-H stretching vibration, usually appears at 3015-3100 cm^{-1} does not appear here probably because of overlap with the alkane C-H stretch region which starts at 3030 cm^{-1} (Fig. 4.9). Another possible explanation is that the alkene species has a π -interaction on the active sites; this π -absorption may stabilize the species and lower the frequency of the alkene C-H stretch into the alkane C-H stretch region, resulting in being masked by the predominant alkane C-H vibrations. The intensity of both C=O and C=C stretches quickly decline with temperature.

6/ Two peaks at 1464 and 1385 cm^{-1} are contributed from the alkane C-H bend of 2-MTHF as these were also observed over pure SiO_2 . The peak at 1464 cm^{-1} has a small left shoulder at 1488 cm^{-1} and a right shoulder at 1450 cm^{-1} . The right shoulder is due to the CH_2 scissoring vibration of the non-aromatic ring of 2-MTHF. Cyclization is known to decrease the frequency of CH_2 bending vibrations while having little effect on C-H stretching vibrations for unstrained cyclic hydrocarbons [7]. For example, cyclohexane absorbs at 1452 cm^{-1} while n-hexane absorbs at 1468 cm^{-1} [7]. In the 1385-1360 cm^{-1} region, there is one peak at 1385 cm^{-1} , attributed to C-H bending of the methyl group of 2-MTHF. On pure silica (Fig. 4.7), the same region showed a doublet (1385 and 1357 cm^{-1}) which is a result of the interaction between the in phase and out-of-phase CH_3 bending of the two methyl and methylene groups attached to the secondary carbon atom of 2-MTHF. Therefore, if 2-MTHF was absorbed in a $\eta^1(\text{O})$ mode on an active site, there should present a doublet as seen on pure silica (Fig. 4.7). So, the loss of the peak at 1360 cm^{-1} on $\text{Ni}_2\text{P}/\text{SiO}_2$ suggests that 2-MTHF may have adsorbed onto the catalyst in a parallel η^5 conformation in which the methyl or methylene group attached to the secondary

carbon atom was immobilized. As this phenomenon was only observed on Ni₂P/SiO₂, the bonding must have occurred on the Ni₂P active phase or at the catalyst/support boundary.

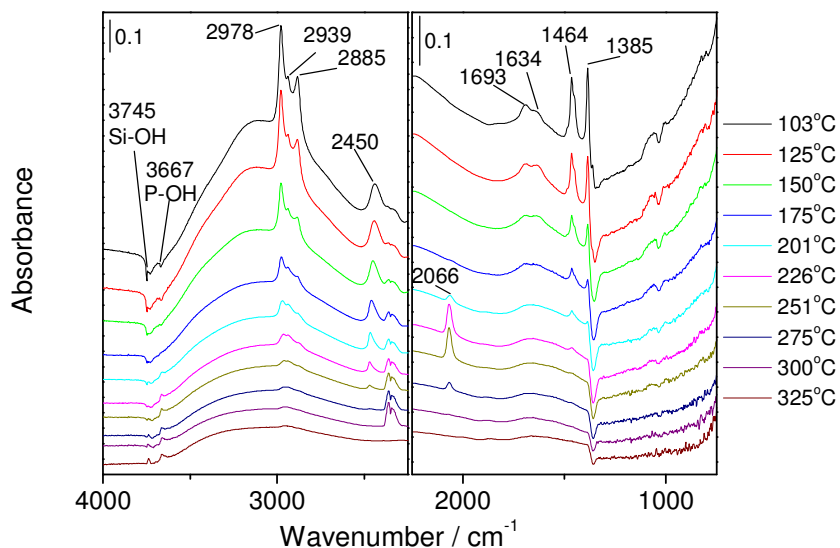


Fig. 4.9. Temperature programmed desorption of 2-MTHF from Ni₂P/SiO₂ in H₂

Overall, the result indicates some transformation of adsorbed 2-MTHF at a temperature as low as 103 °C. The presence of 2-pentanone species (#5) in the low temperature range compared to the CO species in the high temperature range indicates that ring-opening has a lower activation barrier energy than decarbonylation.

A significant change was observed as the temperature-programmed desorption was carried out in He (Fig. 4.10). In the high wavenumber region the FTIR spectra show a less significant recovery of the SiOH and POH groups at 3746 and 3667 cm⁻¹ and an elimination of the P-H species at 2450 cm⁻¹ (Fig. 4.10). In the low wavenumber region the features at 1693 and 1636 cm⁻¹ are present, yet follow a different trend. The $\nu_{C=C}$ band (1636 cm⁻¹) is more intense initially and the $\nu_{C=O}$ band (1693 cm⁻¹) is less prominent. As temperature increases the $\nu_{C=C}$ band

decreases and broadens to lower wavenumbers while the $\nu_{C=O}$ band rises to a maximum and then decreases. As temperature passes 275 °C two new bands appeared at 1656 and 1600 cm^{-1} , corresponding to conjugated C=C stretching [7]. These features maybe attributed to pentadienes or furan derivatives. A small but clear peak at 1488 cm^{-1} is seen from 105°C to 200°C. A previous study on thiophene assigned the band at 1491 cm^{-1} to a di- π -absorbed 1,3-butadiene species and the band at 1449 cm^{-1} to both π and σ -bonded butenes [13]. It might be the case here with pentadiene as a product. Other peaks associated with pentadiene in the 3000 cm^{-1} region were not observed, due to the small quantity and overlap with the alkane C-H region as explained above (#6).

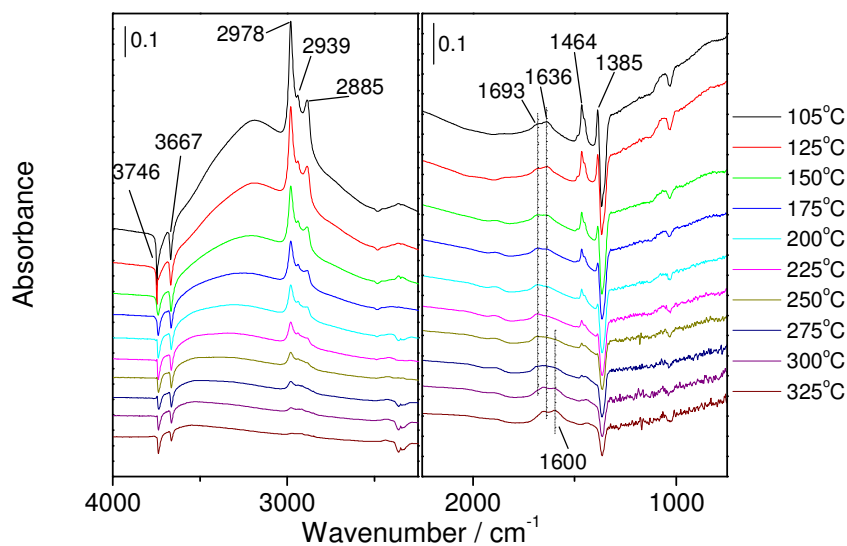


Fig. 4.10 Temperature programmed desorption of 2-MTHF from $\text{Ni}_2\text{P}/\text{SiO}_2$ in He

Overall, the initial trend of $\nu_{C=C}$ and $\nu_{C=O}$ species is in agreement with the contact time study in which pentenes decreases over time and 2-pentanone reaches a maximum before

declining. The presence of conjugated $\nu_{C=C}$ at the high temperature indicates the conversion of 2-MTHF in He proceeds via dehydrogenation route.

The reaction of 2-MTHF on Ni_2P/SiO_2 was also monitored in H_2 and He using FTIR (Fig. 4.11, Fig. 4.12). In the presence of constant 2-MTHF flow, additional vibration absorptions at 1100 and 1025 cm^{-1} was observed. These peaks correspond to the slight feature at 1067 and 1000 cm^{-1} observed in desorption experiments and are attributed to the C-O-C or C-C-C stretching of 2-MTHF [7]. The shift to higher frequency occurs because of the increased coverage of adsorbed species. The increase in temperature which lowers the intensity of other bands seems to not affect these bands, especially the band at 1100 cm^{-1} . The spectra of 2-MTHF conversion in H_2 are similar to those observed in the desorption experiment under H_2 (Fig. 4.11, Fig. 4.9). The main difference shows at the 1700-1600 cm^{-1} region where the $\nu_{C=O}$ stays at the same location while the $\nu_{C=C}$ starts at lower wavenumber – 1605 cm^{-1} . The broad C=C band at 1605 cm^{-1} indicates the formation of a conjugated structure which could be 2-methylfuran, pentadiene, or a mixture of 2-methyltetrahydrofuran and pentenes species. As temperature increases, both C=O and C=C stretching absorption decrease their intensity. This is as expected since reaction proceeds faster at higher temperature, hence the less chance to observe intermediate species on the surface. During the decrease, the C=O band stays at the same location, whereas the C=C band starts at 1605 cm^{-1} and moves toward higher frequency, indicating the diminishing of conjugated alkenes and rising of mono alkenes. The ketone species appeared to decline at a slower rate than the alkene species, consistent with the contact time study in which 2-pentanone is the secondary product and pentene is the primary product. Carbon monoxide was detected at 200 °C, the same temperature as in the previous desorption experiment (Fig. 4.9). The intensity

of absorbed CO goes through a maximum at 250 °C, again, the same as the previous result Fig. 4.9.

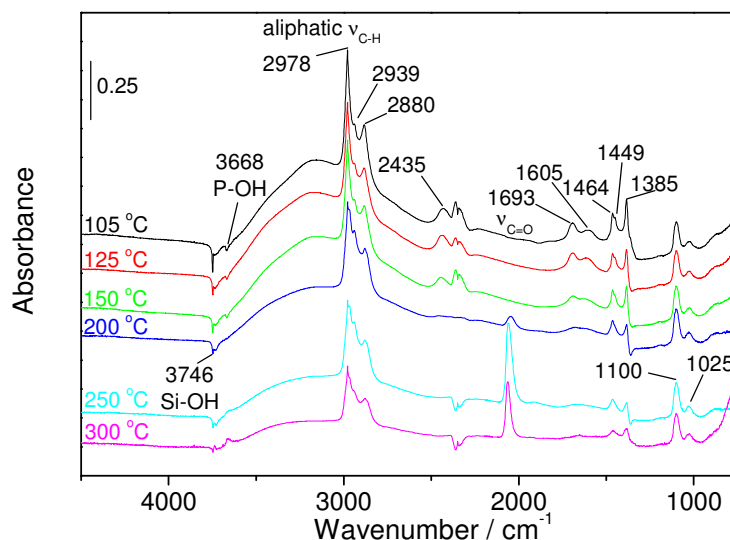


Fig. 4.11. FTIR spectra of 2-MTHF adsorbed on Ni₂P/SiO₂ in 0.32% 2-MTHF/H₂ flow as a function of temperature

In 0.32% of 2-MTHF in He, similar species to the H₂ experiment was detected, yet the trend of these species exhibits dramatic change (Fig. 4.12). First, a slower recovery of SiOH and POH groups at 3746 and 3667 cm⁻¹ was observed as these peaks remain negative as temperature increases. Second, there is no P-H at 2450 cm⁻¹. At low temperature, there are C=O and C=C bands at 1690 and 1636 cm⁻¹, respectively. The intensity of these peaks decreases as temperature increases. As temperature passes 150 °C a new set of peaks forms at 1656 cm⁻¹ and 1600 cm⁻¹. The new peaks are attributable to conjugated alkene species such as 2-methylfuran and pentadienes. The intensity of the peak at 1600 cm⁻¹ increases significantly as temperature

increases, suggesting that the conversion of 2-MTHF in He proceeds mainly via dehydrogenation.

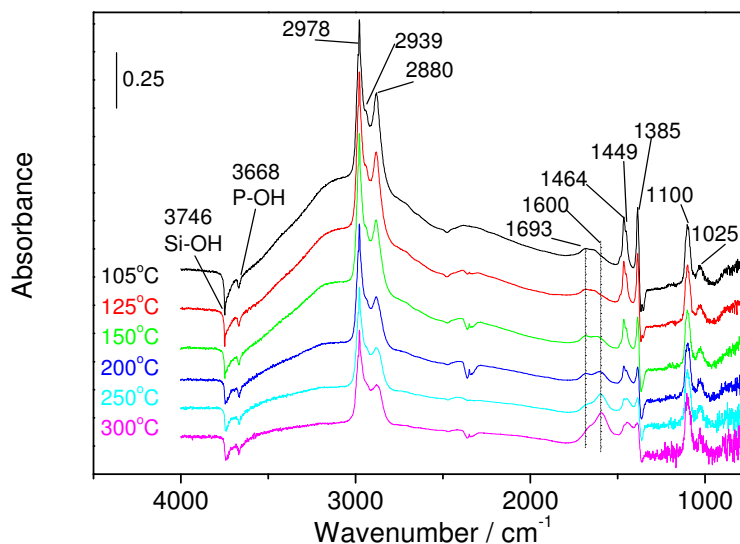


Fig. 4.12. FTIR spectra of 2-MTHF adsorbed on Ni₂P/SiO₂ in 2-MTHF/He flow as a function of temperature

A transient study in H₂ was conducted by monitoring the catalyst surface as 2-MTHF was introduced into the system. Fig. 4.13 shows spectra as time increases from 0 to the steady-state of 150 min. The results are in good agreement with the result of the contact time study. Alkenes were formed first with initial growth of the C=C vibration at 1630 cm⁻¹. Then, 2-pentanone followed with a C=O band at 1693 cm⁻¹ starting at 90s and growing past the C=C band after 300 s. At steady state, the surface intermediates came to equilibrium with each other and the intensity of the ketone species remained higher than the alkene species.

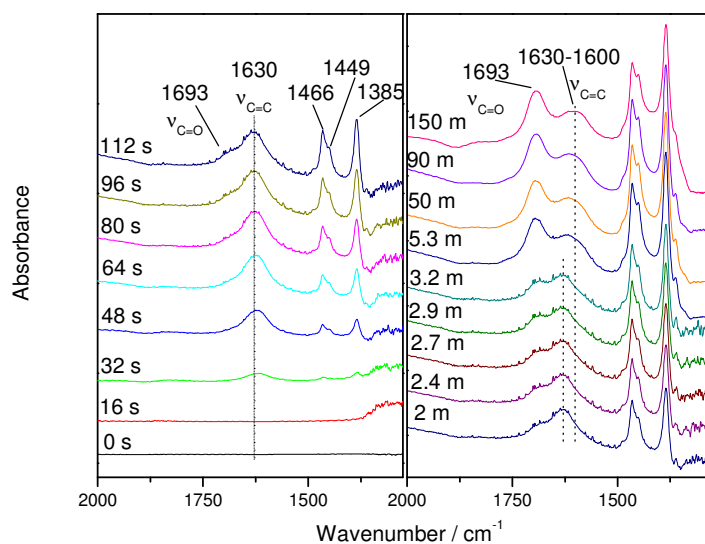


Fig. 4.13. Transient FTIR spectra following the introduction of 2-MTHF onto Ni₂P/SiO₂ in H₂

Table 4.4: Assignment of FTIR peaks

Wavenumber / cm ⁻¹	Assignment	Contributions	Reference
3746	SiO-H stretch	Si-OH	[3-5]
3668	PO-H stretch	P-OH	[3-5]
2978, 2939, 2885	Aliphatic C-H stretch	-CH ₃ , -CH ₂ , -CH, 2-MTHF, 2-pentanone, pentenes, 2-methylfuran	[7]
2450	P-H stretch	Phosphite residue	[14]
2066	C-O	CO	[5, 15]
1693	C=O stretch	2-Pentanone, n-pentanal	[7]
1634	C=C stretch, unconjugated	Pentenes	[7]
1653&1600	C=C stretch, conjugated	Pentadienes, 2-methylfuran	[7]
1490	C=C stretch	Pentenes, pentadienes, 2-methylfuran	[5]
1464&1450&1385	C-H bending	-CH ₃ , -CH ₂ , -CH 2-MTHF, pentenes, 2-pentanone, pentenes, 2-methylfuran	[7]
1385	Tertiary C-H (alkanes)	2-MTHF	[7]
1100&1025	C-O stretch	2-MTHF, 2-methylfuran	[7]

4.4. Conclusions

The hydrodeoxygenation of a heterocyclic O-compound (2-methyltetrahydrofuran) was investigated on Ni₂P/SiO₂ using a combination of temperature programmed desorption, kinetic study, and Fourier transform infrared spectroscopy. The apparent activation energy was calculated to be 134 kJ/mol. The conversion of 2-MTHF was found to be first order in 2-MTHF partial pressure and an order of 0.17 in H₂ partial pressure. The low dependence on external hydrogen indicates hydrogen transfer between the reactant and the catalyst active sites. FTIR result on the Ni₂P surface was in agreement with the contact time study in which an alkene species was formed first followed by a ketone species, indicating pentenes are primary products and 2-pentanone was a secondary product.

4.5. Supplementary Information

4.5.1. Crystallite size calculations

Crystallite size was calculated using the Scherrer equation $D_c = \frac{K\lambda}{\beta \cos(\theta)}$ in which:

K is the shape factor with a value of 0.9

λ is the X-ray wavelength with a value of 0.154178 nm

β is the line broadening at half the maximum intensity in radians (accounting for instrumental broadening of 0.1°)

θ is the Bragg angle

θ Bragg angle / degree	Crystal Face	β Width at half height / rad	Crystallite size / nm	Average crystallite size / nm
40.8	111	0.0103	14.4	14.5
44.6	201	0.0103	14.6	
47.3	210	0.0105	14.5	

4.5.2. Weisz – Prater criterion for internal diffusion

The Weisz – Prater criterion C_{WP} uses measured values of the rate of reaction to determine if internal diffusion is limiting the reaction as follows:

$$C_{WP} = \frac{\text{Actual reaction rate}}{\text{A diffusion rate}} = \frac{-r'_{A(obs)}\rho_c R^2}{D_e C_{As}}$$

Internal mass transfer effects can be neglected when the value of C_{WP} is less than 1. The parameters used for the criterion are listed in Table 4.5. The observed rates $-r'_{A(obs)}$ were calculated at each contact time and listed along with the corresponding C_{WP} values in Table 4.6.

Table 4.5. Parameters in the Weisz-Prater Criterion

R	Catalyst particle radius / cm	0.08
ρ_c (Ni ₂ P)	Solid catalyst density for Ni ₂ P / g·cm ⁻³	0.3
D_e	Effective diffusivity/ cm ² ·s ⁻¹	0.1

Table 4.6: C_{WP} values for reactivity test at low temperature

Temperature / °C	C_{As} Gas concentration at the catalyst surface / mol·cm ⁻³	$-r'_{A(obs)}$ Reaction rate / mol g ⁻¹ s ⁻¹	C_{WP} values
150	9.50E-07	2.42E-10	2.31E-16
162	9.24E-07	7.11E-10	6.57E-16
175	8.97E-07	1.92E-09	1.72E-15
187	8.74E-07	5.07E-09	4.43E-15
200	8.50E-07	1.38E-08	1.17E-14
223	8.11E-07	6.47E-08	5.25E-14
225	8.07E-07	7.38E-08	5.96E-14

References

1. C. L. Yaws, P. K. Narasimhan, C. Gabbula. *Yaws' handbook of antoine coefficients for vapor pressure*. 2009 [cited 2012 10/04]; Available from: <http://www.knovel.com>.
2. K. Kreuzer, R. Kramer, *J. Catal.*, 167 (1997) 391.
3. A. P. Legrand, H. Hommel, A. Tuel, *Adv. Col. Interface Sci.*, 33 (1990) 91.
4. S. T. Oyama, T. Gott, K. Asakura, S. Takakusagi, K. Miyazaki, Y. Koike, K. K. Bando, *J. Catal.*, 268 (2009) 209.
5. Y. -K. Lee, S. T. Oyama, *J. Catal.*, 239 (2006) 376.
6. M. Hawkins, L. Andrews, *J. Am. Chem. Soc.*, 105 (1983) 2523.
7. R. M. Silverstein, F. X. Webster, *Spectrometric identification of organic compounds*. 6th ed. 1998, New York: Wiley.
8. S. T. Oyama, Y. -K. Lee, *J. Phys. Chem. B*, 109 (2005) 2109.
9. Peri, J. B., *Discuss Faraday Soc.*, 41 (1966) 121.
10. Peri, J. B., *J. Catal.*, 86 (1984) 84.
11. R. H. Bowker, M. C. Smith, M. L. Pease, K. M. Slenkamp, L. Kovarik, M. E. Bussell, *ACS Catal.*, 1 (2011) 917.
12. S. Sitthisa, D. Resasco, *Catal. Lett.*, 141 (2011) 784.
13. Z. Wu, Z. Hao, P. Ying, Z. Wei, C. Li, Q. Xin, *J. Phys. Chem. B*, 104 (2000) 12275.
14. T. C. Stringfellow, J. D. Trudeau, T. C. Farrar, *J. Phys. Chem.*, 97 (1993) 3985.
15. K. I. Hadjiivanov, G. N. Vayssilov, *Adv. Catal.*, 47 (2002) 307.

Chapter 5

Conclusions

5.1. Conclusions

The decomposition of ethanol in helium was investigated on Ni₂P/SiO₂ in comparison to an acidic catalyst HZSM-5. Chemisorption measurements showed that Ni₂P/SiO₂ contained a mixture of metal sites (134 μmol g⁻¹) and acidic sites (381 μmol g⁻¹) while HZSM-5 had few metal sites and a substantial amount of acidic sites (565 μmol g⁻¹). The nickel phosphide catalyst exhibited a higher reactivity towards ethanol deoxygenation than the HZSM-5 catalyst.

To elucidate the decomposition mechanism of ethanol on Ni₂P/SiO₂, contact time experiments were carried out. The results indicated that acetaldehyde was a primary product and ethylene was a secondary product. A network of sequential reactions of surface intermediates was proposed to explain the phenomenon. First, the reactant adsorbed on the catalyst surface, then species reacted to form an adsorbed acetaldehyde species which could desorb or form adsorbed alkene species; finally, the alkene species desorbed as ethylene. This rake-type mechanism was supported by a simulation that produced good agreement with the experimental data. Fourier transform infrared measurements confirmed the formation of the adsorbed aldehyde and alkene intermediate species, thus, further validated the mechanism.

Reactions of 2-methyltetrahydrofuran on Ni₂P/SiO₂ were carried out on a series of transition metal phosphides. The phosphides were prepared via the phosphate (A) precursors (conventional method) and the phosphite (I) precursors (new method). The (A) catalysts went through harsher preparation conditions and had lower surface area than the (I) catalysts. Both type of catalysts showed comparable reactivity towards the HDO of 2-MTHF except for WP. The difference was attributed to the surface P/W ratio that X-ray photoelectron spectroscopy measurements showed to be twice as large for the (I) method than the (A) method.

At 300 °C and 1atm, reactivity towards 2-MTHF of the phosphides followed the order of: Ni₂P > WP > MoP > CoP > FeP > Pd/Al₂O₃. Iron group phosphides (Ni₂P and CoP) produced mostly pentane and butane, whereas group 6 metal phosphides (WP and MoP) and FeP produced mostly pentenes and pentadienes.

For Ni₂P/SiO₂, contact time study showed pentene as primary products, 2-pentanone as secondary product, and pentane as a final product. Fourier transform infrared spectroscopy showed formation of surface intermediate species in consistency with the contact time study results. The conversion of 2-MTHF on Ni₂P showed a first order in 2-MTHF concentration and an order of 0.17 in H₂ concentration. The low hydrogen dependence indicated active hydrogen transfer among the reactants, the products and the catalytic active sites.

5.2. Recommendations for future work

1/ Computational calculations

Based on the kinetic information from Chapter 4, one can propose various mechanisms of 2-MTHF reactions on Ni₂P and perform numerical simulations to obtain the best fit mechanism

that describes the observed physical phenomenon. Density function theory is also an excellent tool to predict adsorption modes of 2-MTHF that are most favored on Ni₂P sites.

2/ Extended X-ray absorption fine structure spectroscopy (EXAFS)

In order to obtain more information on the active phase of Ni₂P, extended X-ray absorption fine structure spectroscopy can be used to characterize the catalyst before, during, and after reaction. The technique reveals information on the bond distances (For examples Ni-Ni, Ni-P, or Ni-O) present on the surface. Comparing the bonds formed during and after the reaction to the ones before the reaction would give insight to the nature of active phosphide catalyst.

3/ Studies on WP catalysts

Steady state results showed that WP had little cracking products and favored the formation of unsaturated carbons. Less cracking results in less CO formation and thus less poisoning effect while unsaturated carbons may have great use in the synthetic polymer industry. Therefore, it would be interesting to study the reactions on WP catalysts.